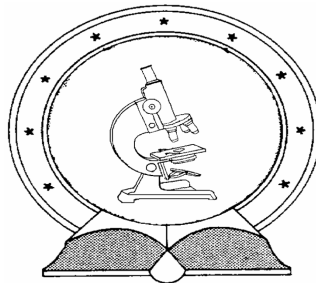


DE TTK



1949

Investigations of nuclear decay half-lives relevant to nuclear astrophysics

PhD Thesis
Egyetemi doktori (PhD) értekezés

János Farkas

Supervisor / Témavezető
Dr. Zsolt Fülöp

University of Debrecen
PhD School in Physics
Debreceni Egyetem
Természettudományi Doktori Tanács
Fizikai Tudományok Doktori Iskolája

Debrecen
2011

Prepared at
the University of Debrecen
PhD School in Physics
and
the Institute of Nuclear Research
of the Hungarian Academy of Sciences
(ATOMKI)

Készült

a Debreceni Egyetem Fizikai Tudományok Doktori Iskolájának magfizikai
programja keretében a Magyar Tudományos Akadémia Atommagkutató
Intézetében (ATOMKI)

Ezen értekezést a Debreceni Egyetem Természettudományi Doktori Tanács Fizikai Tudományok Doktori Iskolája magfizika programja keretében készítettem a Debreceni Egyetem természettudományi doktori (PhD) fokozatának elnyerése céljából.

Debrecen, 2011.

Farkas János

Tanúsítom, hogy Farkas János doktorjelölt a 2010/11-es tanévben a fent megnevezett doktori iskola magfizika programjának keretében irányításommal végezte munkáját. Az értekezésben foglalt eredményekhez a jelölt önálló alkotó tevékenységével meghatározóan hozzájárult. Az értekezés elfogadását javaslom.

Debrecen, 2011.

Dr. Fülöp Zsolt
témavezető

Investigations of nuclear decay half-lives relevant to nuclear astrophysics

Értekezés a doktori (PhD) fokozat megszerzése érdekében a fizika
tudományágban

Írta: Farkas János, okleveles fizikus és programtervező matematikus

Készült a Debreceni Egyetem Fizikai Tudományok Doktori Iskolája
magfizika programja keretében

Témavezető: Dr. Fülöp Zsolt

A doktori szigorlati bizottság:

elnök: Dr.

tagok: Dr.

Dr.

A doktori szigorlat időpontja: 2011.

Az értekezés bírálói:

Dr.

Dr.

Dr.

A bírálóbizottság:

elnök: Dr.

tagok: Dr.

Dr.

Dr.

Dr.

Az értekezés védésének időpontja: 2011.

Contents

1	Introduction	1
2	Radioactivity and lifetimes	5
2.1	The discovery of radioactivity	5
2.2	General decay characteristics	7
2.3	Common decay modes	10
2.3.1	Nucleon emission decay	10
2.3.2	β decay and electron capture	13
2.3.3	Nuclear de-excitation	15
2.4	Measuring lifetimes	18
2.4.1	Detection of the decay products	18
2.4.2	Other technique	20
2.5	Radioactive decay and astrophysics	20
2.6	Recent questions	22
3	Experimental investigations of the lifetime of embedded ^{74}As	25
3.1	Nuclear reaction measurements for astrophysics	26
3.2	Electron screening of nuclear reactions and decay	28
3.3	The Debye–Hückel screening model	30
3.3.1	The foundations of the Debye–Hückel model	30
3.3.2	Lifetime predictions based on the Debye–Hückel model	33
3.4	Experimental results in the literature	33
3.5	The outlines of our experiment	35
3.5.1	The decay of ^{74}As	36
3.5.2	Host materials	37
3.5.3	Model predictions	37
3.6	Experimental instrumentation	39

3.6.1	Target evaporation	39
3.6.2	Irradiation at the cyclotron of Atomki	40
3.6.3	γ detection and electronics	41
3.7	The course of the measurement and its results	44
3.7.1	Measurement runs	44
3.7.2	Data analysis	45
3.7.3	Results	45
3.8	Conclusions	48
4	The lifetime of embedded ^{74}As at low temperatures	51
4.1	The predicted temperature dependence	51
4.2	Experimental results in the literature	52
4.3	The outlines and instrumentation of the experiment	53
4.3.1	Cooling system	54
4.3.2	Target preparation and irradiation	54
4.3.3	γ detection	55
4.4	The course of the measurement and its results	58
4.4.1	Measurement runs	58
4.4.2	Data analysis	58
4.4.3	Results	59
4.5	Conclusions	61
5	Lifetime determination of $^{133\text{m}}\text{Ce}$ and $^{154\text{m}}\text{Tb}$ with γ spectrometry	65
5.1	The astrophysical γ -process	65
5.2	Cross section measurements for the γ process	67
5.2.1	The activation method	68
5.2.2	When the half-life is incorrect	69
5.3	The determination of the half-life of $^{133\text{m}}\text{Ce}$	70
5.3.1	Motivation	70
5.3.2	Target preparation	70
5.3.3	The activation chamber	71
5.3.4	Irradiation	73
5.3.5	γ detection	73
5.3.6	Data analysis	75
5.3.7	Results	78

5.4 The determination of the half-life of ^{154m}Tb	81
5.5 Conclusions	85
6 The Newcomb–Benford law as a test of decay models	89
6.1 A historical review of the Newcomb–Benford law	89
6.2 The Newcomb–Benford law and nuclear half-lives	90
6.2.1 The distribution of the first digits	90
6.2.2 Ones scaling test	92
6.3 Mathematical explanation	92
6.4 Is the law applicable to test nuclear decay models?	95
7 Summary	99
7.1 Summary	99
7.2 Összefoglalás	103
Publications	108
Acknowledgements	110
Bibliography	111

Chapter 1

Introduction

The discovery of radioactivity (Becquerel, 1896) marks the birth of nuclear physics. More than a century have passed since then, during which applications based on nuclear decay found their way to applied science and industry, and became part of our everyday life. The exponential nature of nuclear decay became common sense since the early researches of Rutherford, and nowadays the use of the exponential decay law and its associated constant, the half-life became widespread in the natural sciences to describe decaying systems. Despite the long history of decay lifetime research, it is still a vivid field of subatomic physics.

In my thesis I write about my research activities carried out as a member of the Nuclear Astrophysics Group of Atomki (Institute of Nuclear Research of the Hungarian Academy of Sciences, Debrecen, Hungary). My work can be divided into three main parts, each of which dealing with different aspects of nuclear decay. In this chapter I give a short introduction to these parts, discuss our motivations and present the structure of the thesis.

In Chapter 2 I give a short historical review of the subject of radioactivity. The basic concepts and notations are introduced there as well as a short description of the common decay modes and measurement technique. I show the connection between astrophysics and nuclear decay, and review the most recent experimental results of the literature aiming to change our view of the exponential decay law.

Chapter 3 and Chapter 4 contain the details of our experiments designed to search for a possible influence of the environment on the lifetime of decaying radionuclides. As nuclear reactions play a key role in the evolution

and death of stars, low energy nuclear reaction cross section measurements are an important part of nuclear astrophysics. At the end of the 1980s such measurements with ~ 10 keV center of mass energies led to results showing a spectacular effect of the electronic environment of the target nuclei on the cross section values due to the electron screening phenomenon. The findings were explained by the classical Debye–Hückel plasma model, which was theoretically extended to the case of embedded decaying nuclei. Experimentalists took effort to verify the theoretical predictions, however their results were ambiguous. Our group joined the debate by carrying out two high precision experiments: one to observe the possible change of the half-life of ^{74}As nuclei in conductor, semiconductor and insulator environments, and one to check whether the supposed effect increases with lowering the temperature as the model predicts.

In Chapter 5 I write about our experiments determining the half-lives of $^{133\text{m}}\text{Ce}$ and $^{154\text{m}}\text{Tb}$ isotopes. Our motivations were again astrophysical: in order to verify the statistical model calculations of low energy reaction cross sections we measured the cross sections of the $^{130}\text{Ba}(\alpha, n)^{133}\text{Ce}$ and the $^{151}\text{Eu}(\alpha, n)^{154}\text{Tb}$ reactions. These reactions also produce the $^{133\text{m}}\text{Ce}$ and $^{154\text{m}}\text{Tb}$ isomers. To perform these measurements we used the activation technique, in which one has to observe the decay of the reaction products in order to determine their quantity at the end of the irradiation. For this, the precise half-life values of the reaction products have to be known. In the case of the $^{133\text{m}}\text{Ce}$ and $^{154\text{m}}\text{Tb}$ isomers the literature contained ambiguous half-lives and the nuclear data compilations gave the values with great uncertainties. Thus before carrying out the cross section experiments we had to measure these half-lives precisely.

In Chapter 6 I discuss the relation between the Newcomb–Benford law (also known as Benford’s first digit law) and nuclear decay half-lives. The first formulation of the Newcomb–Benford law goes back to the 19th century. The law gives the general distribution of the first significant digits of various number sequences coming from a wide range of data sources. It was found to be correct for data coming from economy, nature, magazines and many other sources. It was also proved to be valid for the half-lives of radioactive isotopes. The mathematical relation between the distribution of the numbers and the satisfaction of the Newcomb–Benford law was

published by Smith in 2008. Using his method based on Fourier analysis I discuss whether the law can be useful in testing decay models, as it was recently suggested by some authors.

A summary closes the thesis in Chapter 7. Here I give answers to the main questions of the above mentioned topics based on the results of our work. After the summary the publications list, acknowledgements and the bibliography can be found.

Chapter 2

Radioactivity and lifetimes

Bámulattal szemléljük a testek önsugárzását ...
(We amazedly watch the spontaneous radiation of matter ...)

L. Ilosvay

In this introductory chapter I lay down the notation and basic results of nuclear decay used frequently throughout the text. I begin with presenting a brief history of the discovery of radioactivity which marks the birth of nuclear physics (Section 2.1). Then in Section 2.2 I paint a general picture of the common treatment of nuclear decay. After that I review the most important decay modes in Section 2.3. In Section 2.4 I discuss the common experimental techniques used in lifetime measurements. I go on by pointing out the relation between nuclear decay and astrophysics (Section 2.5). The chapter ends by a short introduction to the most actual questions concerning the lifetimes of radioactive isotopes in Section 2.6.

2.1 The discovery of radioactivity

The beginning of nuclear physics is usually connected to Antoine Henri Becquerel's discovery of radioactivity [1]. In his early research between 1895 and 1897 Becquerel showed that various materials emit ionizing radiation which blackens photographic plates. He could demonstrate that this radiation can be attributed to the presence of uranium, which was an early indication for the existence of a sub-atomic structure, the nature of which could not be explored by chemical means [10].

In 1897, Marie Skłodowska-Curie and her husband, Pierre Curie started their research in the field of radioactivity. They performed the first activity measurements by measuring the changes in the resistance of air exposed to radiation [11]. Becquerel, Marie and Pierre Curie were awarded the Nobel prize in physics in 1903 for the discovery of radioactivity.

The different types of radiation were identified by Ernest Rutherford, Becquerel and Paul Ulrich Villard in 1899 and 1900. It was shown that radioactive elements can emit less (α) and highly penetrating (β) particles [12]. From their interactions with electrostatic and magnetic fields, it could be inferred that α rays consist of particles having positive electric charge, while β particles have negative charge. For the discovery of the α and β radiation and a new element (radon), Rutherford was awarded the Nobel prize in chemistry in 1908. By spectroscopic means he was also able to identify α particles as ionized helium [13], an element which had only been found in terrestrial environment a few years earlier. β rays were found identical to cathode rays, i. e. electrons [14]. A third component (γ) was also found and was identified as highly penetrating electromagnetic waves [15, 16]. Much later other decay modes were discovered: β^+ , electron capture (ε), spontaneous fission and particle (proton, neutron, ^{14}C , ...) emission. The first two are similar to β decay, which was renamed to β^- decay (see Section 2.3.2), while the mechanism behind the last two decay types is akin to that of α decay (see Section 2.3.1) [9]. The changes in the proton number (or atomic number, Z), neutron number (N) and mass number ($A = Z + N$) followed by α , β^- , β^+ , ε , proton and neutron emission decays can be seen in Fig. 2.1.

Radioactive decay played a major role in the observation of the atomic nucleus. In 1909, Hans Geiger and Ernest Marsden used α rays emitted by radium to survey the structure of the atoms. They recorded the angular distribution of the α particles scattered from a thin gold foil [17]. The surprising result (i. e. a significant number of particles scattered in a backwards angle) was interpreted by Rutherford two years later. He found that there has to be a scattering center in the atom the radius of which is about five orders of magnitude smaller than the atomic radius: he discovered the atomic nucleus [18].

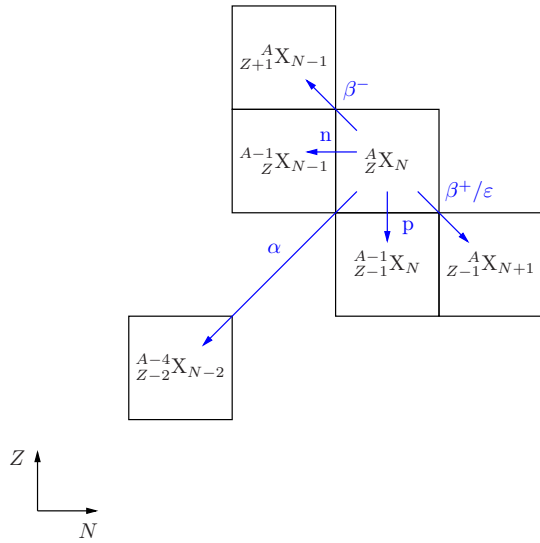


Figure 2.1: Typical nuclear decay modes and their effect on the proton, neutron and mass number of the parent nucleus.

2.2 General decay characteristics

When the activity of radioactive materials became measurable, experiments were conducted to examine the change of the activity in time. Here we discuss the simplest case, when the radioactive sample contains only one species of active component, while all the other components are stable (non-radioactive) [9, 2].

Let $N(t)$ denote the number of radioactive nuclei at a given time t . We define the activity as the rate of change of decaying nuclei of the simplest sample (see above): $-\frac{dN}{dt}$. One can measure the number of decaying nuclei in the time interval $[t_1, t_2]$

$$-\Delta N = \int_{t_1}^{t_2} \left(-\frac{dN}{dt} \right) dt = N(t_1) - N(t_2). \quad (2.1)$$

From such measurements it turns out that the decay of radioactive isotopes can be described by an exponential law, the *decay law*

$$N(t) = N_0 e^{-\lambda t} \quad (2.2)$$

where N_0 denotes the number of nuclei at time $t = 0$, and λ is the *decay constant*. From this, one can get the equation for the activity

$$\frac{dN(t)}{dt} = -\lambda N(t). \quad (2.3)$$

This equation expresses that the number of the decaying nuclei is proportional to the actual number of the nuclei. The law suggests that the decay of the individual nuclei are independent events with a given probability λdt , the value of λ being fixed during the measurement. Thus, nuclear decay is a Poisson random process [3]. The decay law is satisfied regardless of the decay method, so the theories of the different decay modes should provide decay probabilities that are independent from time, as well as the environmental changes that happen in a long running measurement (ex. changes in temperature, humidity or lighting). The decay law for three arsenic isotopes with different half-lives is illustrated in Fig. 2.2.

Let us note that the general definition of activity comes from the activity of the simplest radioactive sample: $A(t) \doteq \lambda N(t)$. For the general case $\frac{dN(t)}{dt}$ contains changes of the number of nuclei for reasons other than decay.

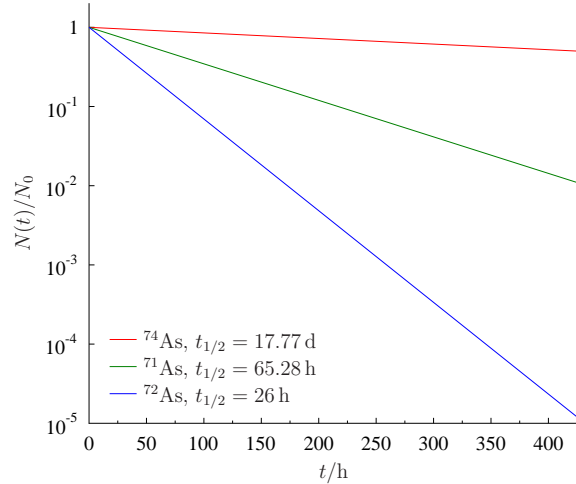


Figure 2.2: Theoretical decay curves of ^{74}As , ^{71}As and ^{72}As in semi-logarithmic scale. The half-lives are taken from Ref. [19].

One can define more expressive quantities to describe the decay probability of active nuclei. The *lifetime* (τ) of a nucleus is the time it takes for

an N_0 initial amount of nuclei to decrease to $\frac{N_0}{e}$: $N(\tau) = \frac{N_0}{e}$. Thus

$$\tau = \frac{1}{\lambda}. \quad (2.4)$$

Lifetime is also called *mean lifetime*, since it also gives the average time of a nucleus before its decay

$$\langle t \rangle = \frac{1}{N_0} \int_0^\infty t \lambda N_0 e^{-\frac{t}{\tau}} dt = \tau. \quad (2.5)$$

Half-life ($t_{1/2}$) denotes the time after which the number of the initial decaying nuclei reduces to one half: $N(t_{1/2}) = \frac{N_0}{2}$. This is the most commonly used quantity to describe decay rates in experimental literature, due to its practical definition.

$$t_{1/2} = \frac{\ln 2}{\lambda} = \tau \ln 2 \quad (2.6)$$

Due to the relatively low energies playing role in nuclear physics, nuclear theories based on non-relativistic quantum mechanics usually have adequate descriptive power. In such theories the dynamics of a nuclear system is described by the Schrödinger equation

$$i\hbar \frac{\partial \Psi}{\partial t} = \hat{H}\Psi = -\frac{\hbar^2}{2m} \Delta \Psi + V\Psi. \quad (2.7)$$

If the potential is time-independent ($V = V(\vec{r})$), it is advantageous to look for solutions that are separable in time,

$$\Psi(\vec{r}, t) = \psi(\vec{r})e^{-iEt/\hbar} \quad (2.8)$$

where the equation for ψ is the time-independent Schrödinger equation $\hat{H}\psi = E\psi$, which is the eigenvalue equation for the energy of the system.

For ψ to represent a physically realizable bound state with energy E , ψ shall be normalizable (in the sense that it shall be square integrable, $\psi \in L^2$) and E shall be real. For scattering states, where the incoming and outgoing particles are wave packages with uncertain energies, the eigenstates are non-normalizable, thus realizable states can only be a linear combination of the energy eigenstates. We are interested in decaying states (also called resonant

or Gamow states), where the particle to be emitted is initially bound, but becomes free after the decay. In this case, $\psi \notin L^2$ and $E \in \mathbb{C} \setminus \mathbb{R}$, where

$$E = E_0 - i\frac{\Gamma}{2} \quad (E_0, \Gamma \in \mathbb{R} > 0) \quad (2.9)$$

(we used the notation $\mathbb{R} > 0 \equiv \{x | x \in \mathbb{R}, x > 0\}$). In this case, the real part of E represents the energy of the emitted particle, while the imaginary part is connected with the probability of emission, i. e. the lifetime, since

$$\Psi = \psi e^{-iEt/\hbar} = \psi e^{-iE_0t/\hbar} e^{-\Gamma t/2\hbar} \quad (2.10)$$

thus

$$|\Psi|^2 = \Psi^* \Psi = \psi^* \psi e^{-\Gamma t/\hbar}. \quad (2.11)$$

By comparing this equation with the decay law (eq. (2.2)), one can see that

$$\Gamma = \hbar \lambda = \frac{\hbar}{\tau} = \frac{\hbar}{t_{1/2}} \ln 2. \quad (2.12)$$

Γ is called the *decay width* or energy width, and is also used to characterize lifetimes of decaying nuclei.

2.3 Common decay modes

In this section I present the most common decay modes: decay by nucleon emission, β decay, electron capture and γ de-excitation.

2.3.1 Nucleon emission decay

Nucleon emission decay occurs when the parent nucleus emits one or more nucleons. The most common nucleon emission decay in nature is α decay and spontaneous fission. Other nucleon emission decay modes, such as proton, neutron or cluster (ex. ^{14}C , ^{24}Ne or ^{28}Mg) emission decay occur more rarely, hence the name of the latter ‘exotic decay modes’. We handle these decay modes together because they share a common physical basis, namely *barrier penetration* [9]. Here we concentrate on the α decay.

During α decay, an α particle (i. e. a ^4He nucleus) is emitted from the parent nucleus



Apart from a few exceptions this process becomes spontaneous only at higher mass regions ($A \simeq 150$), where the Q value for α emission becomes significantly positive [9]

$$Q_\alpha = (m_X - m_Y - m_\alpha)c^2 = T_Y + T_\alpha, \quad (2.14)$$

where m denotes the mass of a particle, while T is its kinetic energy (in the system of the parent nucleus). Since it is usually possible for the parent nucleus to decay to different states (ground state and excited states) of the daughter nucleus, there are different Q values for each of the attainable daughter energy levels. Moreover, it follows from the conservation of momentum that the share of the kinetic energy between the α and the recoiling nucleus is fixed, i.e. $T_\alpha = Q_\alpha \frac{A-4}{A}$, where A is the mass number of the parent nucleus [9]. This makes the observed α spectrum (and cluster decay spectra) discrete [3]. This is not true for spontaneous fission though, since fissile nuclei can decay by emitting various different nuclei [3].

Since α decay is by far the most common nucleon emission decay mode, it was the first explained by barrier penetration (Gamow, Condon and Gurney, 1928). The dynamics of the decay is governed by two forces. On the one hand, if the particle formed inside the nucleus is charged, it interacts with the protons of the nucleus via *Coulomb repulsion*

$$V(r) = \frac{1}{4\pi\varepsilon_0} \frac{zZ}{r}, \quad (2.15)$$

where z and Z are the charge number of the particle and the rest of the nucleus respectively, and r is the distance from the center of the nucleus.

On the other hand, nucleons being hadrons, they interact by the residual strong force called *nuclear force*. This interaction is usually approximated by a mean-field approach, resulting in a deep, radial potential well, the diameter of which describing the size of the nucleus (\sim fm). In the simplest case, the potential well is taken as a finite radial square well, while a more realistic description can be given by using e.g. the Woods–Saxon potential [4]

$$V(r) = -\frac{V_0}{1 + e^{\frac{r-R}{a}}}, \quad (2.16)$$

parametrized by V_0 (depth, ≈ 50 MeV), R (nuclear radius, \sim fm) and a (diffuseness, ≈ 0.5 fm). Since both of these forces are spherically symmetric

and time independent, one has to use the radial Schrödinger equation to formulate the problem [2]

$$-\frac{\hbar^2}{2m} \frac{d^2 u(r)}{dr^2} + \left[V(r) + \frac{\hbar^2}{2m} \frac{l(l+1)}{r^2} \right] u(r) = Eu(r), \quad (2.17)$$

where $u(r) = rR(r)$ and $\psi(\vec{r}) = R(r)Y_l^m(\theta, \phi)$, $Y_l^m(\theta, \phi)$ being the spherical harmonics. Here, $V(r)$ is the net force coming from the Coulomb and nuclear force potentials (see Fig. 2.3), and $V_L = \frac{\hbar^2}{2m} \frac{l(l+1)}{r^2}$ is the centrifugal term which modifies the $V_{eff} = V(r) + V_L$ effective potential for different values of l (the azimuthal quantum number) [2].

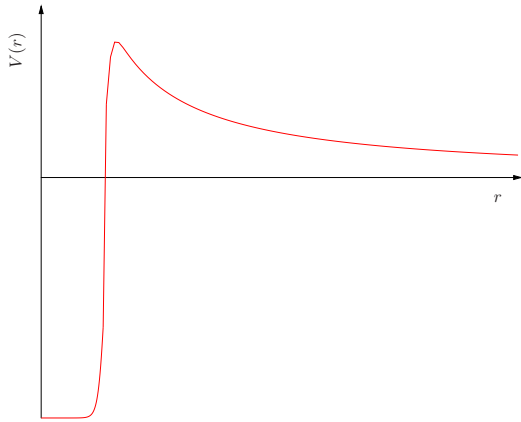


Figure 2.3: The net potential acting on a charged particle inside and around the nucleus.

Quantum mechanics makes it possible for a particle to penetrate potential barriers exploiting the phenomenon of tunneling. There are many methods used to calculate the tunneling probability, and only the roughest approximations lead to analytically solvable equations. One of these equations belong to the approximation when the net potential is given by a simple one dimensional square barrier [9, 2, 5]. To solve for more realistic potentials, like the 3-dimensional radial square well plus Coulomb barrier or Woods–Saxon well plus Coulomb barrier, one has to use special approximations along with numerical methods. These approximations contain methods like the WKB (Wentzel–Kramers–Brillouin) or perturbation

[9, 2]. It can be shown from such calculations that the contribution of barrier penetration to the decay rate is approximately $e^{-2\gamma}$, where $\gamma = \gamma(Z, T_\alpha)$, Z being the atomic number of the parent nucleus and T_α is the kinetic energy of the emitted α [2].

To get the decay rate of the nucleus, the probability of penetration has to be multiplied by the probability of the formation of the cluster and its frequency of impacts on the barrier inside the nucleus [9]. It can be shown that in the most basic cases for α decay the penetration probability has the most significant effect on the decay rate of the nucleus [2]. Thus the theory supports the experimental observations summarized by the Geiger–Nuttall law, showing that the logarithm of the experimental half-lives of α unstable nuclei is proportional to $T_\alpha^{-1/2}$ [2, 9]

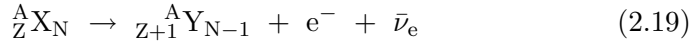
$$\log t_{1/2} = a + \frac{b}{\sqrt{T_\alpha}}, \quad (2.18)$$

making α half-lives extremely sensitive to T_α .

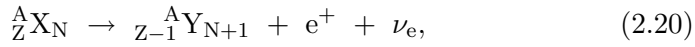
The described theory can not provide accurate lifetime values in general, thus the theoretical investigations of cluster decay is still an active field. Current research is conducted by utilizing more recent theory, like the shell model or the Bardeen–Cooper–Schrieffer (BCS) approaches [20].

2.3.2 β decay and electron capture

β decay is the transformation of a given type of nucleon inside the nucleus to another type of nucleon due to the weak interaction. Thus, it comes in two forms



and



where e^- and e^+ are the electron and the positron respectively, and ν_e denotes the electron neutrino, while $\bar{\nu}_e$ is the electron antineutrino. Eq. (2.19) is the transformation formula of the β^- decay, and eq. (2.20) shows the β^+ decay.

Unlike the α spectrum of α decay, the electron spectrum of β decay is continuous. The existence of the neutrino has been inferred from this fact (Pauli, 1930) [9], assuming that the kinetic energy is shared between the

emitted lepton (electron, electron neutrino), antilepton (positron, electron antineutrino) and the recoiling nucleus. A spectacular experimental evidence for the existence of the neutrino was found in Atomki in 1957 [21] with the cloud chamber shown in Fig. 2.4.

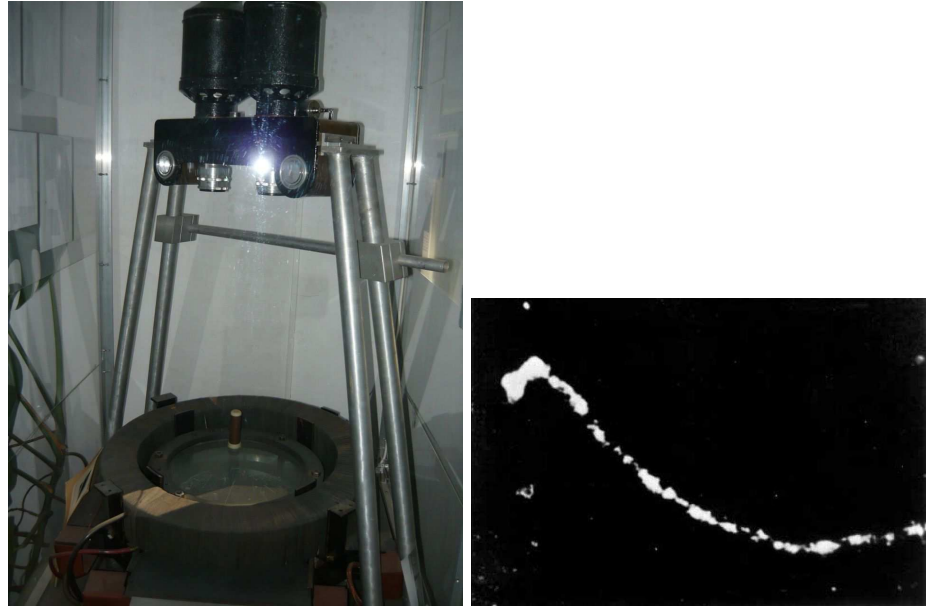


Figure 2.4: (left) The Wilson cloud chamber used to demonstrate the existence of the neutrino (1957). The device was developed by Csikai and Szalay soon after Szalay founded the Nuclear Research Institute (Atomki) in Debrecen. Now it is on display as part of the historical collection of Atomki. (right) This photograph taken with the device provided evidence for the existence of the neutrino.

The Q value equation reflects the three-body nature of β^- decay [9]

$$Q_{\beta^-} = (M_X - M_Y - M_{e^-} - M_{\bar{\nu}_e})c^2 = T_Y + T_{e^-} + T_{\bar{\nu}_e}. \quad (2.21)$$

On the one hand, the mass of the neutrino is close to 0, necessitating the use of relativistic kinematics for its modeling. On the other hand, the kinetic energy of the recoiling nucleus is low, so they can be handled by non-relativistic methods. In some cases it is satisfying to use the approximations $M_\nu = 0$ and/or $T_Y = 0$ [9]. The Q value formula for the β^+ decay is analogous to eq. (2.21).

β decay can be modeled by quantum dynamics, i. e. by a time-dependent potential [2]

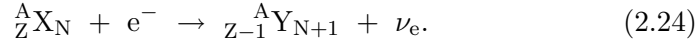
$$\hat{H}(t) = \hat{H}_0 + \hat{H}'(t), \quad (2.22)$$

where only the \hat{H}' interaction Hamiltonian contains time dependence. If the time-dependent part of the potential is small compared to the time-independent part, the problem can be approximated by time-dependent perturbation theory, yielding (in first order) *Fermi's golden rule* of state transition between the i initial and f final state [5, 9]

$$\lambda_{fi} = \frac{2\pi}{\hbar} \left| \left\langle \psi_f^0 \left| \hat{H}' \right| \psi_i^0 \right\rangle \right|^2 \sigma(E_f), \quad (2.23)$$

where λ_{fi} is the transition probability per unit time (i.e. the decay constant), the matrix element $H'_{fi} = \left\langle \psi_f^0 \left| \hat{H}' \right| \psi_i^0 \right\rangle$ contains the initial and final stationary states of the unperturbed problem (ψ_i^0 and ψ_f^0), and $\sigma(E_f)$ denotes the density of states around the final energy E_f .

β^- [β^+] decay is energetically possible if $M_P > M_D$ [$M_P > M_D + 2m_0$], where M_P and M_D is the mass of the parent and daughter nucleus, respectively, while m_0 is the electron mass [9]. If the energy difference between the parent and daughter nuclei is less than $2m_0c^2$ (where m_0 is the electron rest mass), then the capture of a shell electron by the nucleus may take place instead of the β^+ decay [9]



The Q value of the electron capture decay is

$$Q_\varepsilon = (M_X - M_Y - B)c^2, \quad (2.25)$$

where B is the binding energy of the devoured electron, which is usually an S electron coming from a highly bound state (K or L). A secondary process takes place after the electron capture (like X-ray or Auger electron emission), triggered by the vacancy created in the atomic shell.

I do not discuss the more exotic types of β decay (like the double β decay and the bound state β decay) here, as they are not necessary to understand this work.

2.3.3 Nuclear de-excitation

Nuclear de-excitation is based on the same principles as atomic de-excitation. A nucleus in an excited state can be created by nuclear reactions or by nuclear decay. De-excitation occurs by the emission of energetic electromagnetic radiation (a γ photon), by ejecting a bound electron from one of

the electron shells around the nucleus (internal conversion) or by creating an e^-e^+ pair (internal pair production). Since most decays and reactions lead to excited nuclei, the observation of the γ rays emitted during γ de-excitations can be used to monitor these nuclear phenomena.

γ decay leads to a daughter nucleus with the same nucleon composition as its parent nucleus, but the daughter will populate either a lower-lying excited state or the ground state. The de-excitation is accompanied by the emission of a γ photon, along with the recoil of the parent nucleus

$$M_0^*c^2 - M_0c^2 = E_\gamma + T_0, \quad (2.26)$$

where $M_0^*c^2$ and M_0c^2 is the energy of the parent and daughter nuclei respectively, E_γ is the energy of the emitted photon and T_0 is the kinetic energy of the recoiling nucleus [9].

The major difference between atomic and nuclear de-excitation is the energy of the emitted photon: the nuclear interaction makes the nucleons in the nucleus more tightly bound than the electrons in the atom bound by the weaker Coulomb interaction, leading to a much higher transition energy in the order of MeV instead of eV–keV. Thus, in the case of shell de-excitations, the recoil of the emitting atom is negligible, while in nuclear de-excitations the recoil energy is in the order of an eV, shifting the emitted photon out of resonance (Mössbauer effect) [1, 9].

Atomic and nuclear de-excitations by spontaneous photon emission is a case of particle–electromagnetic field interaction, which cannot be fully understood by using only nonrelativistic quantum mechanics. Within the framework of quantum electrodynamics (QED), spontaneous emission is a special case of stimulated emission, induced by the particle’s interaction with the quantum fluctuations of the electromagnetic field [2, 5, 9]. Here we give a summary of the semi-classical model, when the electromagnetic field is treated classically. In this case, spontaneous emission can be handled by time-dependent perturbation theory, leading to Fermi’s golden rule as mentioned in the previous section [2, 9]

$$\lambda_{fi} = \frac{2\pi}{\hbar} \left| \left\langle \psi_f^0 \left| \hat{H}'_{\text{em}} \right| \psi_i^0 \right\rangle \right|^2 \sigma(E_\gamma), \quad (2.27)$$

where $\sigma(E_\gamma)$ is the density of final states to which a photon is emitted with energy $E_\gamma = \hbar\omega = E_i - E_f$. As a first approximation, one can use the

minimum electromagnetic coupling potential [9]

$$H'_{\text{em}} = \frac{e}{m} \vec{p} \vec{A}, \quad (2.28)$$

where \vec{p} is the particle momentum and \vec{A} is the classical vector potential of the electromagnetic field. The utilization of QED can be avoided by assuming that the vector potential takes the form of a planar wave in the radiation zone [5]

$$\vec{A} = A_0 \vec{\epsilon} \cos(\vec{k} \cdot \vec{r} - \omega t), \quad (2.29)$$

where $\vec{\epsilon}$ is the unit vector characterizing the polarization of the radiation. By eqs. (2.28) and (2.29), one has to evaluate the matrix element [5]

$$[H'_{\text{em}}]_{fi} = \frac{eA_0}{2m} \left[\vec{e} \vec{p} e^{-i\vec{k}\vec{r}} \right]_{fi}. \quad (2.30)$$

Depending on the energy (and thus \vec{k}) of the emitted photon, higher orders of the Taylor series (the multipole series expansion)

$$e^{-i\vec{k}\vec{r}} = 1 - i\vec{k}\vec{r} + \frac{1}{2!}(-i\vec{k}\vec{r})^2 + \dots \quad (2.31)$$

can be neglected, leading to the dipole approximation (when leaving only the first order), the electric quadrupole and magnetic dipole approximations (leaving the second order) and other multipole approximations (leaving higher orders) of the emitted electromagnetic radiation [5]. The result for dipole radiation is [9]

$$\lambda_{fi} = \frac{4}{3} \alpha \left(\frac{E_\gamma}{\hbar c} \right)^3 c \left| \left\langle \psi_f^0 \left| \hat{\vec{r}} \right| \psi_i^0 \right\rangle \right|^2, \quad (2.32)$$

where α is the fine-structure constant expressing the strength of the electromagnetic coupling of the radiation field to the matter field

$$\alpha = \frac{1}{4\pi\epsilon_0} \frac{e^2}{\hbar c} \approx \frac{1}{137}. \quad (2.33)$$

The total angular momentum selection rule for dipole transitions are $\vec{J}_f = \vec{J}_i + \vec{1}$, so multipole transitions have to be taken into account when encountering transitions with higher change in angular momentum. The probabilities belonging to these transitions are much lower than the typical transition probabilities of dipole transitions, making the characteristic time

of such transitions longer. Transitions for which the order of the first allowed polarity in the multipole expansion is high are called isomeric transitions, and the corresponding nuclear states *isomeric states* [9]. Just as in the case of atomic de-excitation by X-ray emission, the resulting γ spectrum is discrete and allows the experimental probing of nuclear energy levels.

Internal conversion is the de-excitation process competing with γ decay. During the process, the excitation energy of the nucleus is transferred to a shell electron (most probably to a K electron, as their wave functions overlap the nucleus the most) making it free with the kinetic energy

$$T_{e^-} = (E_i - E_f) - B, \quad (2.34)$$

where B is the binding energy of the ejected electron [9].

Electrons coming from internal conversion have discrete spectra, but the energies of the nuclear bound state differences are varied by the electron shell energies. If the excited nucleus is the daughter of a parent nucleus undergoing β decay, the discrete spectrum appears superimposed on the continuous β spectrum discussed in Section 2.3.2 [9].

Finally, *internal pair production*, i.e. the creation of an electron – positron pair may occur if the transition energy of the nucleus is higher than $2m_0c^2$. Besides of producing electrons, this process increases the yield of the 511 keV peak due to positron annihilation.

2.4 Measuring lifetimes

Lifetimes are measured by monitoring either the number of decaying nuclei $N(t)$ or the activity $A(t)$. The latter is more common as it can be done by detecting the decay products emitted by the source.

2.4.1 Detection of the decay products

The complexity of detecting the activity of a decaying sample depends mostly on the decay mode. During the various decay modes heavy charged particles (ions), light charged particles (electrons and positrons), neutrons, electromagnetic radiation (γ rays, X-rays) or neutrinos can be emitted. Except for the neutrino, these can be detected to measure the source activity. This subsection is based on [3].

Heavy charged particles. Ions are easy to detect and to shield against because of their intense interaction with matter. Thus they have low penetrability and the source is prone to self-absorption. Ions are emitted during nucleon emission decay. In the case of cluster decay (like the most common α decay) the ion spectrum is discrete and characteristic of the Q value of the decay and the mass ratio of the parent and emitted nuclei. Fissile nuclei decay into various pairs of medium mass ions. The fission products get easily absorbed in material due to their high initial charge state.

Light charged particles. Electrons have moderate penetrability. On the one hand the electron spectrum of β decay is continuous. On the other hand the spectrum of conversion electrons (coming from the de-excitation of excited nuclear states by internal conversion) is discrete. Sometimes a discrete low energy electron spectrum can also be taken. This occurs when the atomic shell becomes excited (e.g. by electron capture or internal conversion) and is de-excited by the Auger process.

Neutrons. Neutrons are emitted during spontaneous fission or the de-excitation of highly excited nuclear states. They have long range due to their lack of charge, and they can only be detected indirectly by collisions or neutron induced nuclear reactions.

Electromagnetic radiation. The high energy γ photons emitted during nuclear de-excitation have high penetrability, making efficient detection harder compared to the detection of charged particles. γ emission accompanies decays when the daughter is created in an excited state like in most β decays. The characteristic time of an allowed γ transition is \sim ps, which makes γ detection suitable to follow decays with much longer lifetimes. As γ emission is connected to nuclear de-excitation, its spectra are discrete. Besides of decay, a characteristic 511 keV γ radiation accompanies electron–positron annihilation taking place after the positron emitted during a β^+ decay slows down. Lower energy electromagnetic radiation comes from bremsstrahlung, Compton scattering (both with continuous spectrum) and shell de-excitation (discrete spectrum). These constitute the background of the γ spectra. In the experiments detailed in this work we used this method to follow the decay of radioisotopes.

2.4.2 Other technique

The above mentioned methods are ideal if a sufficiently active sample can be made by activation and the half-life is in the handleable range of a few seconds to a few decades. If this is not the case, more sophisticated methods have to be applied. I briefly discuss here three of such methods: storage rings are suitable to examine highly charged states, very short half-lives can be measured with RIBs, while with AMS one can measure very long half-lives.

RIBs. Radioactive Ion Beam (RIB) setups are used to create exotic nuclei with either high or low neutron-to-proton ratio. These are created by fragmenting accelerated heavy nuclei. The fragments are separated and identified by their time of flight and energy loss in a degrader foil. The half-life can be measured with various methods. One such method is to stop the nuclei in a double-sided silicon strip detector and then measure the time between the implantation and the decay [22].

Storage rings. After producing the nuclei (for example by fusion reaction, fission or fragmentation in a RIB facility) the products can be sent into a storage ring (SR) after separation. Once in there, the half-life of the decaying radionuclides circling in the ring can be measured by e.g. Schottky mass spectrometry or in-ring particle detectors. With this method it is possible to measure the lifetime of highly charged radionuclides as the charge state of the ions can be preserved for hours [23].

AMS. Utilizing Accelerator Mass Spectrometry (AMS) to measure half-lives became available with the increasing precision of AMS measuring technique. As AMS is capable of detecting very low abundances of a given isotope (to a precision of $1 : 10^{12} - 1 : 10^{18}$), if a large enough sample is used the decay of radionuclides with long half-lives becomes measurable [24].

2.5 Radioactive decay and astrophysics

The observation of the starlit night sky (astronomy) and the pursuit of understanding the clockworks of the sky and its constituents (astrophysics) are most probably as old as our species. Astrophysics today give more and more accurate answers to the classical questions regarding sky objects, like what is the Sun? What the stars are? How do they work? Curious enough,

these questions born with the conscience of mankind, we had to wait for the answers until the 20th century, the birth of modern physics.

As soon as scientists began their research on the atomic nucleus, they have found nuclear physics (and thus nuclear decay) closely intertwined with the nature of stars. As in 1928 George Gamow discovered quantum tunneling as the phenomenon making α decay possible (see Section 2.3.1), it could be used to describe nuclear reactions as well (Atkinson and Houtermans, 1929) [6]. The idea that exothermic nuclear reactions provide the energy of stars (besides the energy coming from the gravitational contraction of an interstellar cloud) was the first that was in agreement with the supposed age of Earth based on geological and biological (evolutional) evidence [6]. Nuclear science also gave the answer to the creation of the chemical elements: through *thermonuclear reactions* and radioactive decay of unstable isotopes, the elements are synthesized inside stars and during cataclysmic stellar events (*nucleosynthesis*).

We call a star *first generation star* if it only contains elements created by primordial (or Big Bang) nucleosynthesis. Primordial elements are mostly isotopes of hydrogen and helium, which are called non-metals in astrophysics, while all other elements with $Z > 2$ are called *metals*. All other elements are created by stellar or supernova nucleosynthesis. *Light elements* (which usually mean lighter-than-iron) are created in stars that are in equilibrium state, in processes such as the p-p chain, triple α reaction, CNO cycle, carbon, oxygen and silicon burning. *Heavy element* nucleosynthesis is grouped into astrophysical processes like the s-process, r-process, rp-process, γ -process and ν -process [1, 7, 8]. The decay of unstable isotopes plays an important role in both light and heavy element nucleosynthesis. The details of these processes can be found in nuclear astrophysics texts, such as Refs. [7, 8]. We provide more details on nuclear reactions in Chapter 3, and on the astrophysical γ -process in Chapter 5, as they have provided motivations for our work.

The investigations of radioactive decay also provides useful practical applications for experimental nuclear astrophysics, as we will see in Chapter 5.

2.6 Recent questions

For a century of activity measurements the exponential decay law has been confirmed for many times. In fact, the exponential nature of radioactive decay with a fixed half-life has become common sense, and for many decades measurements were concentrating on the precise determination of the half-lives. This seems to be changing nowadays. In this section I shortly summarize the recent observations foreboding the non-exponential nature of nuclear decay.

Non-exponential decay. Although the exponential decay law in experimental physics is common sense, quantum mechanics reproduces it as a first order approximation. For realistic calculations, quantum mechanics predicts non-exponential decay (see eg. [25] and references therein). The deviation from exponentiality is usually so minor, that it could not have been found experimentally for decades. Recently, the missing evidence is thought to have been found in atomic [26, 27] and nuclear physics [28] experiments. According to the theoretical studies the non-exponentiality arises both at very short times and on the long run: e.g. after a long time elapsed a power decay law appears preceded by oscillations [25]. In the following results the exponential decay is assumed, but the decay constants are found to depend on the environment.

GSI oscillation. Litvinov *et al* in Ref. [29] investigated the electron capture decay half-life of hydrogen-like $^{140}\text{Pr}^{58+}$ and $^{142}\text{Pm}^{60+}$ ions while they circled round in the Experimental Storage Ring (ESR) of GSI, Darmstadt. They have found the lifetime of the ions to oscillate around the exponential decay curve with a period of about 7 s, changing the half-life by up to 23 %. They have interpreted their result by assuming that the emitted neutrino has at least two different mass eigenstates [29]. At the time of writing the ‘GSI anomaly’ has not been confirmed by independent experiments and the theoretical interpretation using neutrino mixing has clearly been refused (see for example Refs. [30, 31, 32]).

Annual wobble. Jenkins *et al* re-analysed the data sequence produced during the earlier half-life measurements of ^{32}Si (decaying by β^-) and ^{226}Ra (decaying mainly by α decay) [33]. They noticed a significant oscillatory change in the measured half-lives with a period of one year, changing the half-lives at most 0.3 %. After excluding all possible environmental effects

(like the effects of temperature or humidity), they began to look for correlations with physical quantities with an annual period. They found significant correlation between the half-life and $1/r^2$, where r is the Earth–Sun distance. This may imply that half-lives are modulated by some radiation emitted by the Sun. According to Ref. [33], this radiation can either be attributed to solar neutrinos or to a scalar field which affects the electromagnetic fine structure constant. To check this hypothesis, the authors examined the change of the β^\pm/ε lifetime of ^{54}Mn during a solar flare, and they observed the slight increase of the half-life [34]. These works induced the re-analysis of half-life measurement data sequences taken for years. In some data analysed partially by the same group, their claims have been confirmed [35, 36], but independent groups could not confirm their results [37, 38]. A simpler explanation for at least some of the results is also known: Semkow *et al* could explain the effects by the annual change of the laboratory temperature [39].

Piezonuclear effects. F. Cardone, R. Mignani and A. Petrucci published the results of their cavitation experiment in 2009 [40]. They have created cavitations by ultrasounds in a solution of ^{228}Th ($t_{1/2} = 1.9\text{ y}$) in water for 90 minutes, and measured the activity of the solution before and after the treatment of the water. They found that most of the thorium ‘disappeared’. According to the explanation of the authors, the extreme environment emerging during the implosion of the cavitations may lead to either the changing of the half-life of ^{228}Th by an order of 4, or to a new type of nuclear reaction they named ‘piezonuclear reaction’ (nuclear reaction triggered by pressure waves). They also proposed that the effect can be caused by the distortion of spacetime during the collapse of a cavitation bubble [41]. The published results induced an intense debate on the pages of Physics Letters A [42, 43, 44, 45]. Both the experimental methods and the data analysis have been criticised [46], and until the time of writing the independent control experiments showed no effect [47].

Effects of the electronic environment. To provide data for nuclear reaction models and astrophysical simulations, experimental nuclear astrophysicists measure nuclear reaction cross sections at low energies. From the beginning of such experiments the sensitivity of the measurements increased, and in the end of the 1980s experimenters could perform measurements at

so low energies that the screening of the Coulomb potential of the nucleus by atomic/metallic electrons could no longer be neglected [7, 50]. At very low energies ($\sim 10\text{ keV}$) the effects of electron screening was found to be significant, and the question arose naturally: is it possible that the electronic environment can noticeably modify the lifetimes of decaying nuclei [48]? If the answer is yes, the results of the half-life measurements shall be modified taking into account the environment of the decaying nuclei depending on whether they are in gaseous form or embedded into insulators/semiconductors/metals. Moreover, this could result in the change of half-lives in plasma, which makes the direct application of the measured half-lives to cosmochronometers and astrophysical models less established [49]. As an application, it was proposed that the embedding of nuclear waste into metals can result in the decrease of the time needed for the neutralization of such waste [49]. We engage this subject in more detail in the following chapters, as a part of my thesis deals with the experimental check of this hypothesis.

As it can be seen from this brief summary of the new results, the investigation of nuclear decay half-lives is an active field of nuclear physics, and it still holds surprises even after a century of research.

Chapter 3

Experimental investigations of the lifetime of embedded ^{74}As

In the present and the following chapter I discuss our experiments examining the possible connection between electron screening and β/ε decay. A brief review of the field is covered in Sections 3.1 to 3.4. In Sections 3.1 and 3.2 I begin with an introduction to low energy nuclear reaction measurements and their relation with electron screening. I also give our motivations here by showing the link between electron screening and radioactive decay. Then in Section 3.3 I describe the historical Debye–Hückel screening model, which was to give predictions on the supposed half-life change of embedded radioactive nuclei. In Section 3.4 I give an overview of the experimental literature preceding our work, while in Section 3.5 I set the aims for our experiment. Section 3.6 contains the detailed description of the experimental instrumentation used in our work. The course of the measurement and the obtained results are presented in Section 3.7. Finally I summarize our experiment in Section 3.8. This chapter is closely related to Chapter 4, at the end of which I compare our results to the literature and draw the conclusions.

3.1 Nuclear reaction measurements for astrophysics

As it was mentioned in the previous chapter, nuclear reactions are responsible for the energy production and element synthesis in stars. The actual transmutation of the elements in stars and supernovae depends on many factors coming from various areas of physics like astrophysics, statistical physics and nuclear physics. From the nuclear physics point of view, the reaction rates (and thus the reaction cross sections) of the different reactions taking place in astrophysical environments play a critical role in developing an accurate model of stellar processes. This makes the measurement of reaction cross sections at low energies an important subject of experimental nuclear astrophysics.

The stars in most of their life consist of hot plasma, which can be treated classically. It can also be assumed that the star is in thermal equilibrium [6]. Thus, the kinetic energy distribution of the charged particles involved in thermonuclear reactions is described by the Maxwell–Boltzmann distribution. A typical main sequence star has a core temperature of $\sim 10^7 \text{ K}$, while core collapse supernova temperatures can go up as high as $\approx 10^{10} \text{ K}$ [6, 51]. By using the equipartition theorem, this roughly corresponds to the kinetic energy interval of $T \sim 1 \text{ keV} – 1 \text{ MeV}$.

Such low energy charged particle induced reactions can be described similarly as α decay. The incoming particle with (center of mass kinetic) energy E and charge $Z_1 e$ approaches the target nucleus with charge $Z_2 e$. The potential field around the nucleus can be described as a sum of the short range nuclear and the infinite range electrostatic (Coulomb) potentials (see Fig. 2.3). In order for the projectile not to bounce off the repulsive Coulomb field, it has to go beyond the classical turning point to be affected by the attracting nuclear force. This can be done by tunneling, as it was described in Section 2.3.1 [2, 5]. The following treatment of unscreened and screened nuclear reactions is based on Refs. [8, 50].

The probability of tunneling through the Coulomb barrier can be written as

$$P = \frac{|\psi_r(r_n)|^2}{|\psi_r(r_{ctp})|^2}, \quad (3.1)$$

where ψ_r is the radial state function and r_n and r_{ctp} are the nuclear radius

and the classical turning point, respectively. In the case of low energies, where $r_{\text{ctp}} \gg r_n$, only the s-wave contribution is needed to be taken into account, and the tunneling probability can be approximated by

$$P = e^{-2\pi\eta}, \quad (3.2)$$

which is called the Gamow factor and η is the Sommerfeld parameter

$$\eta \sim \frac{Z_1 Z_2 e^2 \sqrt{\mu}}{\sqrt{E}}, \quad (3.3)$$

where μ is the reduced mass of the two-body system.

The astrophysically relevant energy range, called the Gamow window is the energy interval where nuclear reactions occur in stars. At a given temperature for a given pair of projectile and target, this range is defined by the Gamow peak, which is the folding of the tunneling probability and the Maxwell – Boltzmann kinetic energy distribution. The Gamow window is at higher energies than the mean kinetic energy of the particles calculated from the equipartition theorem, since for nuclear reactions the higher energies have heavier weights due to the penetration probability. The Gamow peak is very small at low temperatures, making nuclear reactions considerably probable only in hot environments.

The reaction cross section $\sigma(E)$ is proportional to the tunneling probability and the de Broglie wavelength ($\lambda \sim 1/E$), the factor of proportionality being $S(E)$, the astrophysical S -factor. Thus one can define $S(E)$ as

$$\sigma(E) = S(E) \frac{1}{E} e^{-2\pi\eta}. \quad (3.4)$$

Astrophysical applications need the cross section values at low energies, making measurements at the relevant energies hard to perform, if not impossible. Thus the reactions are typically measured above the Gamow window and the results are extrapolated to lower energies. When no resonance occurs, $S(E)$ changes much less with the energy than the cross section itself, making the low energy extrapolation of the S -factor more convenient than the extrapolation of the cross section.

3.2 Electron screening of nuclear reactions and decay

Usually the screening of the Coulomb potential by the atomic electrons can be neglected in nuclear reaction cross section measurements. Due to the developing techniques and the efforts of experimental nuclear astrophysicists, whose aim is to perform measurements as close to the Gamow window as possible, cross sections can now be measured at such low energies ($\sim 10 \text{ keV}$) where the effects of electron screening can no longer be ignored. This section is based on [7, 50, 52, 53, 54].

The major difference between the screened and unscreened Coulomb potential is in their range: while the Coulomb potential has infinite range, screening makes it to have a cut-off at the ‘atomic radius’ r_a . This can decrease the classical turning point greatly when the kinetic energy T of the incident charged particle is lower than the *screening potential* U_e

$$T \leq U_e := \frac{Z_1 Z_2 e^2}{r_a}, \quad (3.5)$$

enhancing the tunneling probability significantly. The screening decreases the height of the Coulomb barrier to a value E_{ebh} , the *effective barrier height*. With this, the *cross section enhancement factor* can be defined as

$$f(E) = \frac{\sigma(E_{\text{ebh}})}{\sigma(E)} = \frac{P(E_{\text{ebh}})}{P(E)}, \quad (3.6)$$

where $P(E)$ is the penetration factor. Assuming that the electrostatic potential of the electron cloud does not change inside the atom ($\Phi_e(r) = Z_1 e / r_a$ ($r \leq r_a$)), the net potential becomes

$$\Phi(r) = \frac{Z_1 e}{r} - \Phi_e(r) \quad (r \leq r_a), \quad (3.7)$$

which makes the effective barrier height

$$E_{\text{ebh}} = \frac{Z_1 Z_2 e^2}{r_n} - U_e = Z_1 Z_2 e^2 \left(\frac{1}{r_n} - \frac{1}{r_a} \right). \quad (3.8)$$

Using the low energy approximation (Eq. 3.2) the enhancement factor becomes

$$f(E) = \frac{E}{E_{\text{ebh}}} \frac{\exp(-2\pi\eta(E_{\text{ebh}}))}{\exp(-2\pi\eta(E))} \simeq \exp\left(\frac{\pi\eta U_e}{E}\right). \quad (3.9)$$

In Fig. 3.1 the measured S -factor of the ${}^3\text{He}(\text{d},\text{p}){}^4\text{He}$ reaction is shown at very low energies [55]. As it can be seen, the effect of electron screening is very prominent, thus if it is not taken into account, the low energy extrapolations of the S -factor can lead to erroneous results. The importance of the question raised the attention of researchers in the field, and both theoretical (e.g. [56]) and systematic experimental (e.g. [57]) studies were published about electron screening in fusion reactions.

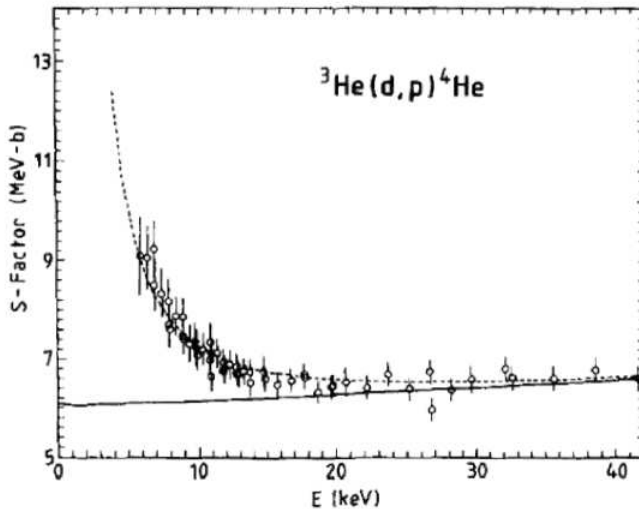


Figure 3.1: The effect of electron screening on the measured S -factor of the ${}^3\text{He}(\text{d},\text{p}){}^4\text{He}$ reaction using gaseous target [55]. The straight line is the expected S -factor without electron screening.

In 2001 Czerski *et al* performed experiments to measure the significance of electron screening [58] by investigating the ${}^2\text{H}(\text{d},\text{p}){}^3\text{H}$ and ${}^2\text{H}(\text{d},\text{n}){}^3\text{He}$ $\text{d}+\text{d}$ reactions at 5 keV – 60 keV on deuterated metallic targets. They experienced an enhanced electron screening effect, U_e being an order of magnitude higher than found in gaseous deuterium targets. A systematic study was performed by Raiola *et al* in 2003 [59]. In their work, 58 different deuterated targets were used, among which there were insulators, semiconductors and metals. They observed the enhanced electron screening in most metals, while only ‘normal’ (gaseous) screening was found when using deuterated insulator, semiconductor or lanthanide targets.

It was in this latter work where the classical Debye–Hückel plasma model appeared as the possible explanation of the enhanced electron screen-

ing in metallic environments. The original idea is that the quasi-free electrons of metals can be treated approximately as the loosely bound plasma electrons [59]. This idea is usually attributed to a co-author of Ref. [59], Professor Claus E. Rolfs, according to whom ‘metals are poor man’s plasma’ [49].

Around the time of these observations, papers reporting the slight change of the electron capture decay rate of ^7Be in different environments were published [60, 61, 62]. Some of the results may have considerable astrophysical consequences, as ^7Be is an important source of solar neutrinos [63]. As a generalization of this phenomenon, the possible dependence of other decay types on the electronic environment was proposed and the suggested model for the handling of the problem was again the Debye–Hückel plasma model [64, 48].

The question of screening is also important from the numerical side: it shall not only be used when an experimental cross section or decay rate value is transferred to the database of a star simulation, but the simulation itself has to handle reactions and decay taking place in hot plasma where electrostatic screening is a factor. Thus the understanding of screening theory heavily influences our predictions of how stars and supernovae work, due to the twofold use of screening. Screening may turn out to be an even more interesting issue as nowadays the researchers’ confidence in traditional star models are decreasing [65].

Though the exact calculations based on the Debye–Hückel model are only vaguely described [48], it has become the basis of comparison for experimental results in the years after the idea appeared. Because of this, and in spite of the theoretical objections of its use in nuclear decay (e.g. [66]) we devote the next section to the detailed overview of this classical screening model.

3.3 The Debye–Hückel screening model

3.3.1 The foundations of the Debye–Hückel model

The screening model of Debye and Hückel (1923) [67] is a classical model of electrostatic screening published as a part of the theory of liquid electrolytes. Today it is part of the foundations of plasma physics as its concepts are used

to define statistically treatable plasmas and thus to designate the boundaries of plasma physics. The following treatment of Debye shielding is based on Refs. [68, 69, 70].

The Debye model can be applied if the following assumptions hold:

- the system is a canonical ensemble [72, 73]: it interacts with its environment thermally and it is at thermodynamic equilibrium, thus it can be characterized by a temperature T . The probability of occupation is given by the Boltzmann distribution

$$n_E = n_E^{(0)} \exp\left(-\frac{E}{k_B T}\right), \quad (3.10)$$

where E is the energy of a single particle, k_B is Boltzmann's constant and n_E is the number of particles occupying a state with energy E . If there are more species of particles in the plasma, the different species need not to be in equilibrium with each other, thus a T_i temperature should be assigned to the gas of each species,

- T is high enough to make the system behave like a classical gas (i.e. the Maxwell–Boltzmann distribution is valid),
- magnetic interactions can be neglected, thus

$$E = T + V = \frac{1}{2}mv^2 + q\phi(\vec{r}), \quad (3.11)$$

where q is the charge of the particle and $\phi(\vec{r})$ is the electrostatic (scalar) potential,

- the changes in the system are slow compared to the mean collision time of the constituent particles, thus
 - it remains in equilibrium all the time ($\forall t : \exists T(t)$),
 - the spatial variations of the temperature is negligible: $T(\vec{r}) \equiv T$,
 - first order approximations are applicable (see later),
- the plasma is electrically neutral if viewed from a distance, which sets the boundary conditions to

$$\phi(\vec{r}) \xrightarrow{r \rightarrow \infty} 0, \quad n(\vec{r}) \xrightarrow{r \rightarrow \infty} n_0. \quad (3.12)$$

By substituting eq. (3.11) into eq. (3.10) and integrating in particle velocity v , our assumptions lead to the spatial particle density

$$n(\vec{r}) = n_0 \exp\left(-\frac{q\phi(\vec{r})}{k_B T}\right). \quad (3.13)$$

Let us examine a plasma consisting of electrons with charge $-e$ and positive ions with charge Ze , into which we immerse a charged plate with charge Q . The problem becomes one-dimensional and gives the equations

$$n_e(x) = n_0 \exp\left(\frac{e\phi(x)}{k_B T_e}\right) \quad (3.14)$$

$$n_i(x) = \frac{n_0}{Z} \exp\left(-\frac{eZ\phi(x)}{k_B T_i}\right) \quad (3.15)$$

where T_e and T_i are the electron and ion gas temperatures, respectively. This can be substituted into the Poisson equation $\Delta\phi = -\rho/\varepsilon_0$ using the charge densities $\rho_e = -en_e$ and $\rho_i = Zen_i$. Expanding the exponentials to first order, one gets the approximation

$$\Delta\phi \approx \frac{en_0}{\varepsilon_0 k_B} \left(\frac{e\phi}{T_e} + \frac{eZ\phi}{T_i} \right). \quad (3.16)$$

Let us introduce the Debye (wave)length λ_D and the Debye wave number k_0 as

$$\lambda_D = \frac{1}{k_0} := \sqrt{\frac{\varepsilon_0 k_B T_e}{n_0 e^2 \left(1 + Z \frac{T_e}{T_i}\right)}}. \quad (3.17)$$

For the similar three-dimensional problem, where Q is a point charge at the origin, one gets the spherically symmetric screened Poisson equation

$$[\Delta - k_0^2] \phi(r) = -\frac{1}{\varepsilon_0} Q \delta(r), \quad (3.18)$$

the solution of which is the screened Coulomb potential, which is formally the same as the Yukawa potential

$$\phi(r) = \frac{1}{4\pi\varepsilon_0} \frac{Q}{r} e^{-r/\lambda_D}. \quad (3.19)$$

Sometimes only the electron gas is considered so the ion term in the denominator of Eq. (3.17) is dropped. The plasma parameter Λ gives the number of particles in the sphere with radius λ_D

$$\Lambda = \frac{4}{3}\pi \lambda_D^3 n. \quad (3.20)$$

λ_D and Λ helps to decide if the plasma can be treated statistically: the plasma should be large enough for its charges to be shielded ($\lambda_D \ll L$, where L is the linear size of the plasma) and there has to be statistical number of particles inside the Debye sphere (i.e. the plasma is weakly coupled, $\Lambda \gg 1$). Knowing this and the original assumptions one can say that the application of the Debye–Hückel model to decaying embedded nuclei is quite far from the problem to which the model was originally constructed. It is worth to note though, that in some cases the statistical description of plasmas can be adequately precise even if the assumptions are not fully satisfied (e.g. when the plasma is strongly coupled, $\Lambda \ll 1$, see [70]).

3.3.2 Lifetime predictions based on the Debye–Hückel model

A Debye–Hückel model based calculation was applied recently to predict the change of the half-lives of radionuclides embedded into metallic environments. Here I review the calculation method presented in Refs. [48, 80].

The electron screening energy U_e in metals is given by

$$U_e = 2.09 \cdot 10^{-11} Z \sqrt{\frac{\rho_{ce}}{T}}, \quad (3.21)$$

where $\rho_{ce} = n_{ce}\rho_a$ is the number density of the conduction electrons (n_{ce} being the number of conduction electrons per atom and ρ_a is the atomic density) and Z is the atomic number of the decaying nucleus ($[U_e] = \text{eV}$, $[\rho_{ce}] = 1/\text{m}^3$, $[T] = \text{K}$). Knowing the Q value of the decay to a given state, the decay rate enhancement factor f for β decay can be calculated as

$$f \approx \left(\frac{Q \pm U_e}{Q} \right)^5. \quad (3.22)$$

The plus sign is applied for β^+ and the minus for β^- decay. For a specific prediction see Section 3.5. As one can see from eq. (3.21), U_e depends on temperature. I discuss this in detail in Chapter 4.

3.4 Experimental results in the literature

In this section we briefly review the experimental results in the literature. Though the questions of half-life alteration goes back to the 1930s [71], here we concentrate only on recent experimental results. In Table 3.1 we

summarize some of the papers that served as motivation for our work. Only these papers were published before we began our work in the field in early 2008. For a review of the literature dealing with the possible temperature dependence of nuclear half-lives see Section 4.2, and for the latest literature (as of 2010) and for a comparison of our results with that of others, see Section 4.5.

Table 3.1: Recent experimental results dealing with the possible change of the lifetimes of radioactive nuclei embedded into various environments. Legend: met: metal, sem: semiconductor, ins: insulator, C_{60} : fullerene cage (ex: exohedral, en: endohedral), 0: no observable change in $t_{1/2}$, 0?: hard to decide if there is a change in $t_{1/2}$, lit: literature value.

Date	Ref.	Source	Host material	$t_{1/2}$
1997	[74]	$^7\text{Be} \varepsilon$	met(Ta), ins	met < ins
1999	[60]	$^7\text{Be} \varepsilon$	met(Au), ins(Al_2O_3)	met > ins
2001	[75]	$^7\text{Be} \varepsilon$	met(Ta,Au), ins(C), BN	met > ins
		$^{40}\text{K} \beta^\pm \varepsilon$	met(Ta,Au), ins(C), BN	0
2002	[76]	$^7\text{Be} \varepsilon$	met(Be,Au)	0
2004	[61]	$^7\text{Be} \varepsilon$	met(Be), $\text{C}_{60}^{\text{en}}$	met > $\text{C}_{60}^{\text{en}}$
2004	[77]	$^7\text{Be} \varepsilon$	met(Au,Pd)	Au > Pd
2006	[78]	$^7\text{Be} \varepsilon$	met(Au), $\text{C}_{60}^{\text{ex,en}}$	met = $\text{C}_{60}^{\text{ex}} > \text{C}_{60}^{\text{en}}$
2007	[79]	$^7\text{Be} \varepsilon$	met(Cu,Al), ins(Al_2O_3 ,PVC)	0?
2007	[80]	$^{198}\text{Au} \beta^-$	met(Au)	met > lit
2007	[82]	$^{221}\text{Fr} \alpha$	met(Au,W), sem(Si), ins(CH_2)	0?

As it can be seen in Table 3.1, most of the recent experiments were conducted using ^7Be as radioactive source. This has multiple reasons. First of all, ^7Be decays by electron capture, which is expected to be the most sensitive to the electronic environment of the decaying nucleus, along with α decay. Moreover, ^7Be has the relatively simple electronic structure $1s^22s^2$, which on the one hand may result in a greater shift of the lifetime [60] and on the other hand it makes theoretical calculations easier. Another important reason is that the decay rate of ^7Be has to be known in order to calculate the neutrino flux coming from the Sun ($^7\text{Be} + e^- \rightarrow ^7\text{Li} + \nu$), thus it plays an important role in nuclear and particle astrophysics [8]. Furthermore, this isotope is fairly easy to create with the $^7\text{Li} + p$ reaction, and its half-life is well-known from several experiments ($t_{1/2} = 53.22\text{ d} \pm 0.06\text{ d}$) [81].

The listed experiments tried to find a dependence of the half-lives on different parameters with which the host materials can be characterized. Such parameters are the conductivity (metal/semiconductor/insulator) [60, 75, 79, 82], the electron affinity [76, 77] and the structure of the surroundings (like lattice structure or chemical forms) [61, 78]. A question mark designates that the results agree with the no effect hypothesis, but are slightly ambiguous.

Let us note that there were no measurement performed for β decaying nuclei until 2007. Though it is true that the influence of the electronic environment on the decay rate is most easily conceivable in the case of electron capture and α decay, but the influence on β^+ and β^- decays were also proposed based on the interaction of the electronic environment and the emitted particle (e^- or e^+) [83].

From the table it can be inferred that the measurements that piled up for a decade until 2007 did not come to a conclusion. This, with the appearance of the screening of nuclear reactions (see Section 3.2) and the proposed Debye screening model lead to an increased interest in the alteration of half-lives in the following years.

3.5 The outlines of our experiment

Some authors of the papers cited in the previous section examined the decay curve of the isotopes, i.e. they measured the sample activity versus time. Such measurements are prone to have an increased systematic uncertainty coming from various sources like the not precisely known dead time of the counting system or the changing of the measuring environment (like the laboratory temperature), and in close connection with the latter, the changing of the instrument parameters (like shifting of the detector efficiency). Such systematic errors may either hinder the finding of small changes in the decay rate or may lead to false positive observations. In order to make the measurements more precise, some authors performed relative measurements, where the activity of the sample was followed in comparison with a standard, well-known source.

The aim of the work described in this chapter is to provide a measurement of the possible change of the lifetime of embedded radionuclides so that the applicability of the Debye–Hückel model on lifetime predictions

can be tested. To achieve our goal we carry out a special relative measurement which enables us to keep the systematic uncertainties of the results as low as possible.

3.5.1 The decay of ^{74}As

In order to perform a relative measurement which is especially suitable to detect minute half-life changes, one has to examine two different decay modes for which a shift of lifetimes in different directions are predicted. To do this, one can use a single isotope with two different decay modes or two different isotopes stucked together, each of which decaying by different processes. We have chosen the radionuclide ^{74}As as there are several properties of this isotope making it an ideal source for our purposes.

^{74}As undergoes either a β^- or a β^+/ε decay. Due to the predictions of Ref. [83], if β decays are affected by electron screening then β^- decay is expected to be suppressed, while β^+ decay should be enhanced by the conduction electrons of metals. If β decay rates do not change, ε decay rate shifts should still be possible to observe if exist.

The β^- decay leads to ^{74}Se with a branching ratio of $I_{\beta^-} = 34\% \pm 2\%$, while the β^+/ε decay produces ^{74}Ge with $I_{\beta^+/\varepsilon} = 66\% \pm 2\%$. Both decays are followed by strong γ radiation due to the de-excitation of the decay daughters. The β^- decay is followed by an $E_\gamma = 634.8\text{ keV}$ radiation (with a relative intensity of $15.5\% \pm 1.2\%$) and the β^+/ε decay by an $E_\gamma = 595.8\text{ keV}$ radiation ($59.4\% \pm 3.5\%$ relative intensity). On the one hand, these γ lines are far enough from each other to be easily distinguished by modern detectors (see Section 3.6), while they are close enough to assume that they are similarly affected by drifts in the detector efficiency. On the other hand, taking into account the ^{74}As half-life of $t_{1/2} = 17.77\text{ d}$, the comparable branching ratios and intensive γ lines make it available to distinctly monitor the γ rays followed by different modes of decay¹. The simplified decay scheme of ^{74}As can be seen in Fig. 3.2.

All these characteristics make the relative intensity measurement of the 596 keV and 635 keV γ peaks of ^{74}As feasible. By measuring the intensity ratio instead of the half-life values we eliminate the sources of systematic errors mentioned in the beginning of this section.

¹All decay data are taken from [84].

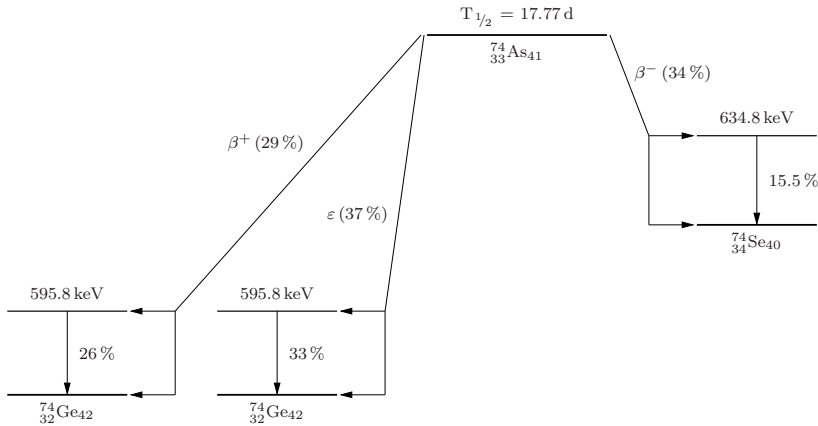


Figure 3.2: The simplified decay scheme of ^{74}As , showing only the transitions relevant to our work. The branching ratios and relative γ intensities are indicated next to the transition arrows. The energy levels are shown to scale.

3.5.2 Host materials

To test the half-life dependence on the host material the ^{74}As nuclei have to be implanted into different substrates. For this purpose germanium, aluminum, tantalum and mylar had been chosen. With this set of host materials we can test the effect of the conductivity, electron affinity and structure on the value of the lifetime. Some basic properties of the host materials can be found in Table 3.2. Mylar is a biaxially oriented polyethylene terephthalate polyester film, thus many of the data in the table does not apply to it. The sample preparation and the implantation technique is described in Section 3.6.

3.5.3 Model predictions

To set the experiment's precision requirements we have to know the magnitude of the change of the half-life predicted on the basis of the Debye–Hückel model. For this purpose we use the equations presented in Section 3.3.

The β^- decay of ^{74}As ($Z = 33$) to the first excited state ($E = 634.8\text{ keV}$) of ^{74}Se has a Q value of $Q = 718\text{ keV}$, while the β^+ decay goes to the first

Table 3.2: Some physical and chemical data of the host materials. a is the lattice constant, ρ is the resistivity, E_{ea} is the electron affinity and χ is the electronegativity in Pauling scale. The data are taken from Ref. [85].

Material	Cond. type	Lattice type	a/pm	$\rho/\Omega \text{ m}$	$E_{\text{ea}}/\frac{\text{kJ}}{\text{mol}}$	χ
Al	metal	FCC	405	$2.6 \cdot 10^{-8}$	42.5	1.61
Ta	metal	BCC	330	$1.3 \cdot 10^{-7}$	31	1.5
Ge	semicond.	FCC	566	$5 \cdot 10^{-4}$	119	2.01
mylar	insul.			$\sim 10^{16}$		

excited state ($E = 595.8 \text{ keV}$) of ^{74}Ge and has a Q value of $Q = 1967 \text{ keV}$. Knowing this, n_{ce} and $\rho_a = \rho_m A / A_r$ for the different hosts (where ρ_m is the mass density, A_r is the atomic weight and A is Avogadro's constant), the enhancement factor for the β^- and β^+ decay branches can be calculated. The values can be seen in Table 3.3. We note that in Ref. [112] a simple scaling of the results of Ref. [59] lead to $U_e \approx 9 \text{ keV}$ for tantalum, which slightly underestimates the predicted change in the intensity ratio.

By taking into account the branching ratios and the γ intensities, one arrives at the predicted shift of the γ intensity ratios I , compared to the intensity ratio in insulators ($I_{\text{enh}}/I_{\text{norm}}$, see Table 3.3). As it can be seen from the table, the predicted half-life changes are high enough to be easily detected. In spite of this the conclusions of the publications of Table 3.1 are far from being consistent with each other. As the observed half-life changes were as high as $\approx 1\%$ (and a magnitude higher at low temperatures, see the next chapter), it was unclear if the Debye screening model shall be adapted to nuclear decay or it shall be replaced completely. Thus a high precision experiment was needed to help in this decision.

Table 3.3: The predicted effect of electron screening on the decay of ^{74}As in the host materials. The prediction for mylar is $f_\beta = 100\%$ as it is an insulator. ρ_m is the mass density and A_r is the atomic weight. I_{enh} is the γ intensity ratio with enhanced β^\pm decays (expected in metals), and I_{norm} is the ratio without enhancement (expected in insulators). The data are taken from Ref. [85].

Material	n_{ce}	$\rho_m/\frac{\text{g}}{\text{cm}^3}$	$A_r/\frac{\text{g}}{\text{mol}}$	U_e/keV	$f_{\beta^-}/\%$	$f_{\beta^+}/\%$	$\frac{I_{\text{enh}}}{I_{\text{norm}}} /\%$
Al	3	2.7	26.982	16.9	88.75	104.38	114.8
Ta	5	16.65	180.948	21.0	86.23	105.44	118.7
Ge	4	5.323	72.64	16.7	88.88	104.33	114.7

3.6 Experimental instrumentation

In this section I discuss the technical instrumentation used in our measurements from the preparation to the detection stage. The ^{74}As isotope was produced by the $^{74}\text{Ge}(\text{p},\text{n})^{74}\text{As}$ reaction. The germanium targets were prepared and put into an activation chamber. The chamber was attached to a beamline of the Atomki cyclotron, which served as a source of the bombarding protons. The active sample was taken to the measuring chamber, where its decay was monitored with a γ detector.

3.6.1 Target evaporation

The targets were prepared by evaporating natural germanium onto thin aluminum foils. The natural abundance of ^{74}Ge is $\approx 36\%$. The germanium was placed into a tantalum boat while the Al backing was put into a sample holder 9 cm away from the boat. The evaporation was carried out by sending up to 86 A alternating current through the boat. The progress of the evaporation was monitored visually. The evaporator can be seen in Fig. 3.3. Two targets were prepared ($m_{\text{Ge}} = \{16, 27\} \text{ mg}$ before the evaporation) on $3\text{ }\mu\text{m}$ thick Goodfellow aluminum foils. The thickness of the Ge layer was determined by weighing: the weight of the foils before and after the evaporation was measured. The thickness of the targets was $30\text{ }\mu\text{g}/\text{cm}^2$ and $50\text{ }\mu\text{g}/\text{cm}^2$. The targets had circular shape with a diameter of 12 mm.



Figure 3.3: The Leybold Univex 350 evaporator used to prepare the natural germanium targets.

3.6.2 Irradiation at the cyclotron of Atomki

The targets have been placed into an activation chamber which serve as a place for the irradiation of a target. The detailed description of our chamber can be found in Section 5.3.



Figure 3.4: (left) The cyclotron of Atomki. (right) The activation chamber attached to the end of a short beamline of the Atomki cyclotron.

The protons for the $^{74}\text{Ge}(\text{p},\text{n})^{74}\text{As}$ reaction was provided by the MGC-20 cyclotron accelerator of Atomki (see Fig. 3.4). We attached our chamber to the end of beamline 2A, as it is seen in Fig. 3.4. The cyclotron provided the proton beam with an energy of 10.2 MeV. The beam current was approximately $1 \mu\text{A}$. The irradiations took 1.5 h – 3.3 h.

The schematic view of the attached activation chamber during the irradiation can be seen in Fig. 3.5. The Al-Ge foil was fixed in a sample holder and placed into the activation chamber, the Al side facing the incoming beam. As the beam hit the target, ^{74}As nuclei were created in the germanium. Most of these nuclei stayed embedded in the germanium, serving as a source for our measurement. According to the reaction kinematics, the arsenic recoil energy varied in the range of (0 – 450) keV with a maximum recoil angle of about 55° . The high energy reaction products could leave the germanium and headed toward the end of the chamber where either a tantalum or an aluminum plate with 0.5 mm thickness was placed. SRIM [86] simulations showed that more than 99.8 % of such nuclei have kinetic energy higher than 10 keV and therefore they got implanted deep inside the crystal lattice of the metal plate. The implanted surface was 15 mm in diameter, while the sample size of the germanium embedded arsenic was about 8 mm, estimated from the lateral beam size. The host material plate served also

as the beam stop and was directly water cooled.

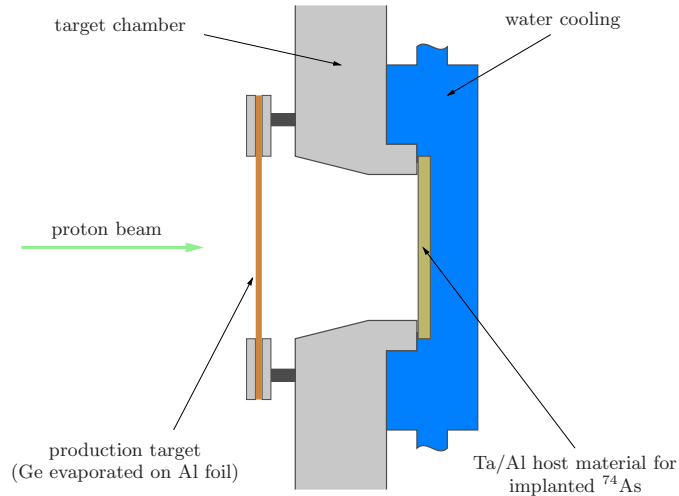


Figure 3.5: Schematic view of the irradiation setup.

The chamber had to be modified in the case of mylar implantation because an insulator cannot be used as a beam stop. To solve this problem the chamber was extended behind the target and the inner surface of the cylindrical extension was covered with an $8\text{ }\mu\text{m}$ thick mylar foil. With the applied geometry the foil was able to catch the ^{74}As leaving the germanium in the angle interval of about $10^\circ - 40^\circ$, which corresponds to an implantation energy range of about (220–440) keV. After the implantation the mylar foil was folded and fixed in a holder to have an approximately same geometry as the metal samples.

3.6.3 γ detection and electronics

After the irradiation the targets were transported to the counting room and placed in front of a γ detector. For this purpose a Canberra n-type high purity germanium (HPGe model GR4025) detector was used with a model 7600SL cryostat and a built-in pre-amplifier (model 2002CSL). This detector has 40 % relative efficiency and needs -4 kV bias voltage, which was supplied by an Atomki bias supply.

The pre-amplified output pulses have to be processed by a series of electronic instruments placed in a NIM crate (in our case it was a NIM BIN NU8205 crate). The signals were amplified by an Ortec 671 spectroscopic amplifier using $2\mu\text{s}$ shaping time. We set the amplification so that the most energetic observable γ ray had an energy of about 1.85 MeV. The amplified analogous signals were converted to digital ones in an Oxford/Tennelec/Nucleus PCA-II MCA PC (ISA) card using 8192 channels. The lower energy threshold of the ADC was set to $\approx 45\text{ keV}$ (i.e. 200 channels). For the energy calibration we used a ^{60}Co source.

The detector was surrounded by a 5–10 cm thick lead shielding in order to reduce laboratory background. The total background with the shielding was found to be 18000 CPH (counts per hour) in the (0–2) MeV energy range. A typical background spectrum can be seen in Fig. 3.6.

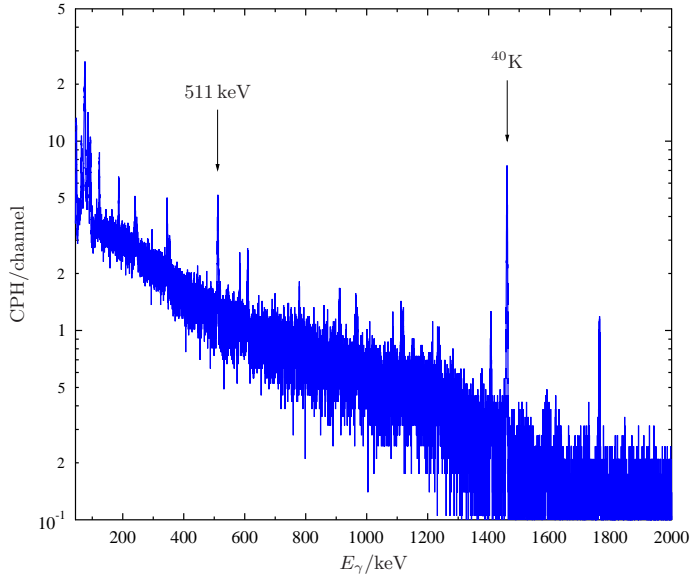


Figure 3.6: Background spectrum in lead shield. At lower energies Pb and Bi X-rays and ^{234}Th γ rays, while at higher energies γ rays from e.g. ^{212}Pb , ^{214}Pb , ^{228}Ac , ^{208}Tl , ^{212}Bi and ^{214}Bi can be seen. Counts: $1.8 \cdot 10^4$ CPH in (0–2) MeV.

A typical spectrum for ^{74}As is shown in Fig. 3.7. As it can be seen, the two peaks along with the 511 keV annihilation peak dominates the spectrum. We observed no disturbing γ activity in any of our samples in spite of the

presence of neutrons from the (p,n) reaction and the fact that the metal samples were directly bombarded by the beam passing through the target. To reduce the true coincidence events coming mainly from the summing of the annihilation peak with our peaks, we set up the relatively large source-to-detector distance of 10 cm.

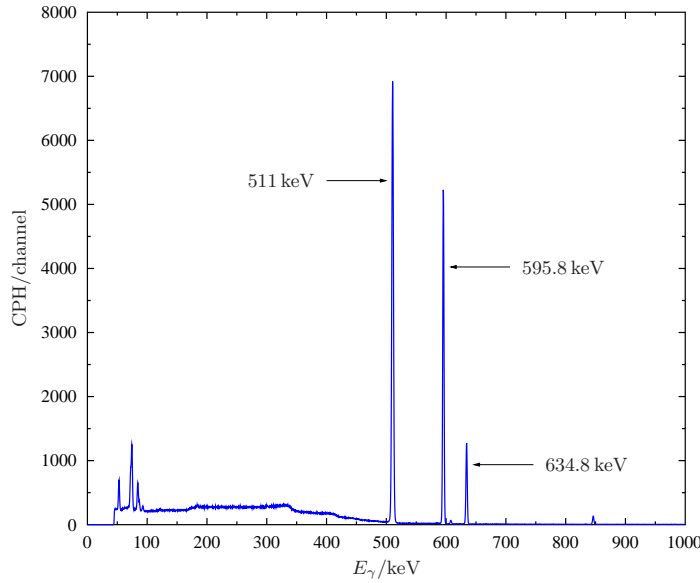


Figure 3.7: Sample spectrum of ^{74}As in Ge, taken for 27.9 h, soon after the irradiation. The two intensive peaks of the ^{74}As along with the annihilation peak at 511 keV can easily be seen. $6.67 \cdot 10^5$ CPH in 45 keV – 1.85 MeV.

To compare the intensity ratio to the literature value we had to know the detection efficiency ratio of the 596 keV and 635 keV peaks. To get this ratio we calibrated the detector for absolute efficiency by recording the spectra of various standard radioactive sources placed at exactly the same geometry as our ^{74}As samples. We fitted the obtained efficiency values and used the fitted line to get the efficiency ratio, which was found to be

$$\frac{\eta(596 \text{ keV})}{\eta(635 \text{ keV})} = 1.051 \pm 0.005. \quad (3.23)$$

The efficiency curve of the detector can be seen in Fig. 3.8.

From the known detector efficiency the source activities could be calculated. The activity of the aluminum, tantalum and mylar samples was

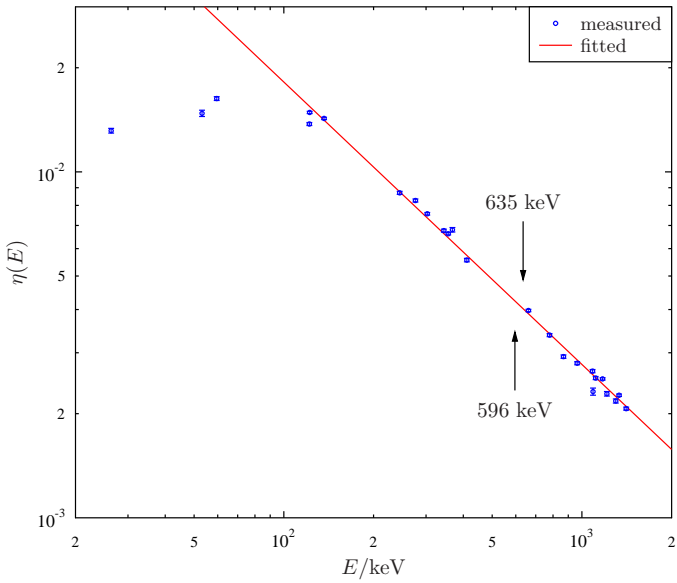


Figure 3.8: The absolute efficiency $\eta(E)$ of the detector. The sample distance is 10 cm. We used ^{60}Co , ^{57}Co , ^{241}Am , ^{137}Cs , ^{133}Ba and ^{152}Eu as calibrating sources.

found to be a few hundred becquerels, while the germanium sample was more active, having an activity of about 2 kBq. Owing to the low activity of the sources the dead time of the data acquisition system was always negligible.

3.7 The course of the measurement and its results

3.7.1 Measurement runs

Three irradiation runs were performed using only the thicker germanium target. One run belonged to each host material. After each irradiation run, the host material carrying the arsenic isotope was transported to the counting room and the spectra were taken. Meanwhile, the embedding of another sample was made at the cyclotron. After the spectra of the aluminum, tantalum and mylar samples were recorded, the relatively high activity germanium target was measured. Finally, a few additional spectra were taken with all the samples to have data with long cooling times for control, if needed. A summary of the irradiation and detection data can be

seen in Table 3.4.

Table 3.4: Data on the measurement runs. t_{irrad} and t_{meas} denote the irradiation and measurement times, respectively. t_{meas} is the sum of the duration of all measurement runs.

Run no.	Host	$t_{\text{irrad}}/\text{h}$	t_{meas}/h
1	Ta	1.83	364
2	Al	1.5	96
3	mylar	3.3	72.3
1–3	Ge	6.63	44.6

3.7.2 Data analysis

Due to the experimental conditions the expected systematic error is very low. To test the intensity ratio with various sources in different measuring geometries, extensive GEANT4 [87] simulations were carried out. In the simulations, different source distributions from the point-like to the 2 cm diameter case were considered as well as up to 1 cm off-axis displacement of the sources. All simulations resulted in the same efficiency ratios within the precision of about 0.5 %. The effect of the position shift of the source was also studied experimentally by repositioning the sources in the counting setup several times. The intensity ratio of a given sample was found to be constant within the statistical uncertainty. The simulations also provided an $(1.3 \pm 0.3) \%$ summing out correction for the 596 keV line.

The spectra were evaluated with the Atomki spectrum analyser software PGM [89]. Gaussian plus background were fitted to the 596 keV and 635 keV ^{74}As peaks. The high intensity of the peaks resulted in good quality fits. From the area of the fitted peaks the intensity ratios were calculated for each of the spectra. Additionally, the (17.77 ± 0.02) d half-life of ^{74}As made it possible to measure the half-life directly and compare it to the literature value. This was done in the case of the tantalum and germanium samples. The decay curve of the arsenic in tantalum can be seen in Fig. 3.9.

3.7.3 Results

Our aim was to retrieve the intensity ratio I of the 596 keV and 635 keV peaks and to examine if this ratio changed with the embedding material.

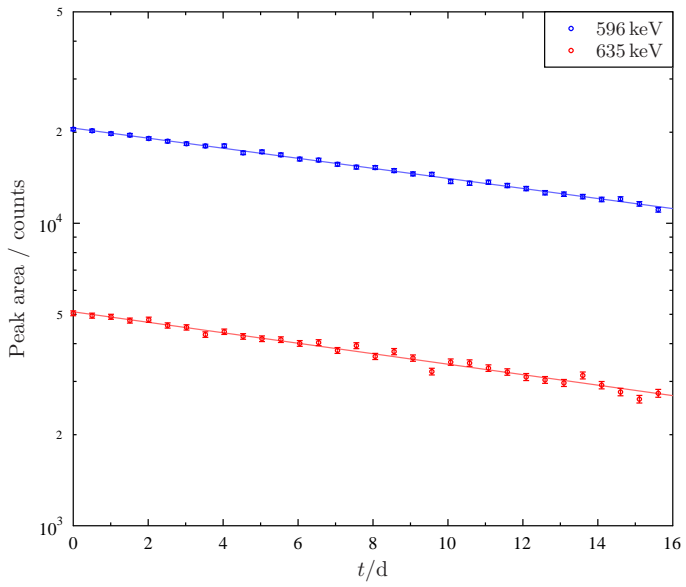


Figure 3.9: Semi-logarithmic plot of the intensity of the 596 keV and 635 keV peaks of ^{74}As in Ta versus time. The lines show the fitted decay curves.

In order to get an informative view of our results we normalized I to the error weighted mean of the measured points and denoted the normalized intensity ratio I_n . This way it was easier to tell statistical fluctuations and real effects apart, if any.

A summary of our results on the intensity ratios can be seen in Table 3.5. The values of the ratios are the error weighted means of the ratios obtained from each spectra, while the uncertainties are the quadratic sum of the statistical uncertainties and the 0.5 % systematic uncertainty coming from geometrical effects. The uncertainties do not contain detector efficiency and summing correction errors as they are the same for all four experiments. The results are shown in Fig. 3.10.

As it was mentioned, the half-life of ^{74}As was also measured in the case of Ta and Ge samples. The decay of the arsenic in the Ta sample was followed for 16 days and saved every 12 hours. The decay in the Ge sample was recorded for 13 days and saved every 6 hours. In order to control any change or long-term variation in the detector efficiency, a ^{60}Co source was fixed to the Al and Ta samples and the half-life was also deduced by normalizing

Table 3.5: Results of the experiment: the intensity ratios of the ^{74}As peaks. ‘Mean’ shows the error weighted mean and its error, while ‘literature’ shows the literature value of the intensity ratio derived from several direct measurements. The data are in the order of increasing resistivity of the host materials. As it can be seen in Tab. 3.3, I_n is expected to vary by at least 10 %, according to the predictions.

Sample	I	$I_n/\%$
Al	3.936 ± 0.038	99.72 ± 0.97
Ta	3.879 ± 0.037	98.28 ± 0.94
Ge	3.955 ± 0.021	100.21 ± 0.54
mylar	3.975 ± 0.027	100.71 ± 0.69
mean	3.947 ± 0.014	100 ± 0.36
literature	3.852 ± 0.082	97.59 ± 2.08

the counting rate from ^{74}As with the 1173 keV and 1332 keV lines of ^{60}Co [90]. (Though ^{60}Co is not the perfect source for this purpose as it increases the Compton-background of our peaks, we only had this standard source at the time of the experiment.) The half-lives were determined from the linear fit on the semi-logarithmic plot of the activity versus time. Table 3.6 shows the measured half-lives of the two sources. In the table I have indicated the half-lives obtained from the peak areas normalized to the ^{60}Co peaks, as well as the half-life gained from the non-normalized peaks. The results are shown in Fig. 3.11. The higher precision of the non-normalized germanium point comes from its better statistics due to higher sample activity. It is worth to note that the diffusion of arsenic in the host materials is negligible at room temperature, thus it cannot affect the measured half-lives [91].

Table 3.6: The obtained half-lives of the embedded ^{74}As samples. The values are the error weighted means of the half-lives obtained from the 596 keV and 635 keV peaks. The literature value is $t_{1/2} = (17.77 \pm 0.02)$ d [84]. The normalized values were used for verification. See the text for details.

method	$t_{1/2}/\text{d}$ in Ta	$t_{1/2}/\text{d}$ in Ge
w/o normalization	17.87 ± 0.22	17.82 ± 0.04
norm. to 1173 keV	17.90 ± 0.24	17.94 ± 0.14
norm. to 1332 keV	17.87 ± 0.24	17.65 ± 0.16

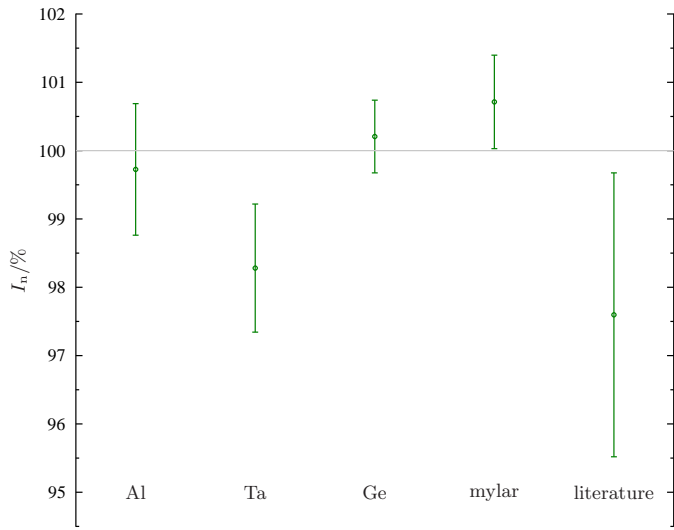


Figure 3.10: Results of our measurements: the normalized intensity ratio I_n of the ^{74}As peaks in different host materials. The points are in the order of increasing resistivity of the host materials.

3.8 Conclusions

From the intensity ratio results summarized in Fig. 3.10 one may see a slight indication that the branching ratio is smaller in metallic environment than in an insulator, but all the deviation of our points from the mean can be explained by statistical fluctuation, as all the points are well within 2σ deviation from the mean. This means that our results are compatible with the assumption that the half-life of ^{74}As does not depend on its material environment.

The measured half-life values of ^{74}As are in agreement with the literature half-life value (see Table 3.6). This also supports the independence of the half-life on the host material.

From our results consequences can be drawn concerning the possible changes of the β^- , β^+ and ε decay rates of ^{74}As in different host materials. According to the prediction (see Section 3.4 and Section 3.5), one expects a higher 596 keV / 635 keV intensity ratio in metals than in insulators if one

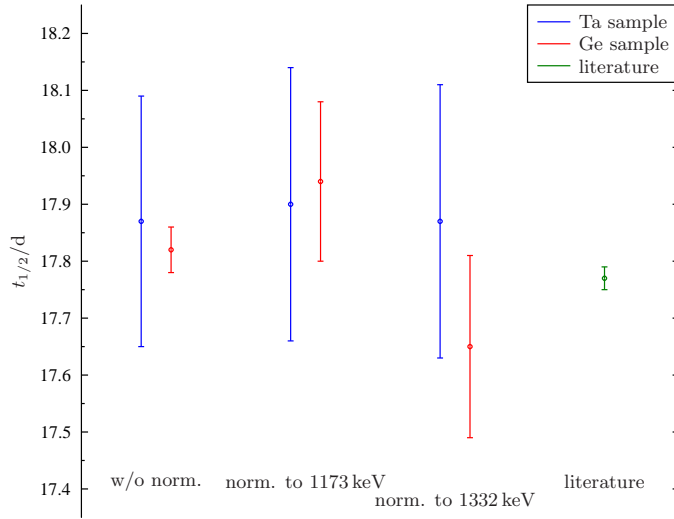


Figure 3.11: The ^{74}As half-life values obtained from the Ta and Ge samples using different methods.

assumes that electron capture decay rate remains unchanged. The results of our measurement contradicts this prediction, especially because we see a minor decrease in the ratio in tantalum. This problem could be solved within the model if the electron capture decay rate has somehow been strongly reduced in the Ta sample. This case can be excluded using the following arguments.

By measuring the intensity ratio of the two arsenic peaks, we get the quantity

$$\frac{a_{\beta^+} \lambda_{\beta^+} + a_\varepsilon \lambda_\varepsilon}{a_{\beta^-} \lambda_{\beta^-}} = \text{const.}, \quad (3.24)$$

where a_i denotes the probability of the emission of the measured γ rays after the isotope undergoes an i type decay. This value has been found to be constant within at most 4 %. According to Ref. [84]

$$a_{\beta^-} \approx 0.45, \quad a_{\beta^+} \approx 0.9, \quad a_\varepsilon \approx 0.9 \quad (3.25)$$

thus, because $a_{\beta^+} = a_\varepsilon$, eq. (3.24) can be written as

$$\frac{\lambda_{\beta^+} + \lambda_\varepsilon}{\lambda_{\beta^-}} = \text{const.} \quad (3.26)$$

The decay rate of ^{74}As can be written as the sum of its partial decay rates

$$\lambda = \lambda_{\beta^-} + \lambda_{\beta^+} + \lambda_\varepsilon = \text{const.} \quad (3.27)$$

We have found this value to be constant within 2 % in our half-life measurement. Eq. (3.24) and eq. (3.27) can only be simultaneously satisfied within the given uncertainties if λ_{β^-} is constant within about 3 % (here we have propagated the mentioned 4 % and 2 % uncertainties). This value is less than half the value of the underestimated prediction of the intensity ratio change of $\approx 7.6\%$ in Ta [112], and much less than the $\approx 18.7\%$ prediction given in Table 3.3. The above considerations would still allow an equal and opposite change in the β^+ and ε decay rates, but this possibility is unlikely if we accept that β^- and β^+ decays are affected by their environment similarly, as has been suggested in [83]. On these grounds we conclude that our measurement supports that the three decay rates of ^{74}As are unaffected by the metallic environment within 3 % precision.

Participation of the author. I participated in the preparation of the targets, in setting up the equipment both at the beamline and at the counting room, the calibration of the detector, the installation and testing of the acquisition system, the irradiation process and the recording of the spectra.

Publication.

Scientific paper

Gy. Gyürky, **J. Farkas**, C. Yalçın, G. G. Kiss, Z. Elekes, Zs. Fülöp and E. Somorjai, *Investigation of ^{74}As decay branching ratio dependence on the host material*, *Europhys. Lett.* **83**, 42001 (2008)

Chapter 4

The lifetime of embedded ^{74}As at low temperatures

While our measurement of the ^{74}As intensity ratio was performed and analysed, further publications appeared dealing with the Debye-model predicted temperature dependence of half-lives. To reinforce the results of our work described in the previous chapter we decided to carry out an experiment under conditions where the temperature of the sample can be varied by orders of magnitude. This chapter contains the details and the outcome of our efforts.

I begin this chapter with the revision of the temperature dependence of the Debye–Hückel model. In Section 4.2 I review the low temperature half-life measurements published before our work. The next two sections contain the description of the instrumentation and the details of the experiment. The results can be found in Section 4.4. In the last section I summarize our room temperature and low temperature results and compare them with the recent literature.

4.1 The predicted temperature dependence

We have given the details of the Debye–Hückel plasma model in Section 3.3 and the predictions to half-lives derived from it in Section 3.5. Though it was in the equations, the temperature dependence was not particularly mentioned. The key concept of the Debye–Hückel model is the Debye-

length λ_D (eq. (3.17)), which is by definition

$$\lambda_D := \sqrt{\frac{\varepsilon_0 k_B T_e}{n_0 e^2 \left(1 + Z \frac{T_e}{T_i}\right)}}. \quad (4.1)$$

It has a $T^{1/2}$ temperature dependence, which migrates to the equation of the screening energy U_e (eq. (3.21)) resulting in

$$U_e = 2.09 \cdot 10^{-11} Z \sqrt{\frac{n_{ce} \rho_a}{T}} \sim T^{-1/2}. \quad (4.2)$$

If we apply this model without reservations (as it was used in some of the recent papers), by decreasing the temperature by a few orders of magnitude, the screening energy is greatly increased, which shall have a great impact on the enhancement factor f (eq. (3.22)).

Table 4.1 shows the predictions of the model to the changes of the intensity ratio of the two strongest peaks of ^{74}As at low temperatures.

Table 4.1: Predicted screening effect on the 596 keV / 635 keV γ intensity ratios at liquid nitrogen ($T = 77\text{ K}$), liquid helium ($T = 4.2\text{ K}$) and $T = 0.3\text{ K}$ temperatures. I_{norm} is the intensity ratio without decay rate change.

Material	$\frac{I_{\text{enh},300\text{K}}}{I_{\text{norm}}} / \%$	$\frac{I_{\text{enh},77\text{K}}}{I_{\text{norm}}} / \%$	$\frac{I_{\text{enh},4.2\text{K}}}{I_{\text{norm}}} / \%$	$\frac{I_{\text{enh},0.3\text{K}}}{I_{\text{norm}}} / \%$
Al	114.8	131.8	360.0	$1.9 \cdot 10^5$
Ta	118.7	141.0	510.0	$9.1 \cdot 10^7$
Ge	114.7	131.4	354.0	$1.6 \cdot 10^5$

4.2 Experimental results in the literature

In this section I give a brief review of the experimental literature dealing with the temperature dependence of the half-lives of radioisotopes embedded into different host materials. A summary of the measurements preceding our experiment can be seen in Table 4.2. This table along with Table 3.1 gives an overview of the literature of the Debye-model related experiments.

As it can be seen from the table, the results in the literature is quite ambiguous. Though many low temperature measurements have been performed (even one at 50 mK), their results were obtained by following the decay, which may (as described in the previous chapter) include unknown

Table 4.2: Recent experimental results dealing with the possible temperature dependence of the lifetimes of radionuclides embedded into metals. For notations see Table 3.1.

Date	Ref.	Source	Environment	T/K	$t_{1/2}$
2006	[48]	$^{22}\text{Na} \beta^+$	met(Pd)	12	$T_{\text{low}} < T_{\text{room}}$
2006	[103]	$^{22}\text{Na} \beta^+$	met(Al)	90	0
2006	[104]	$^7\text{Be} \varepsilon$	met(Pd,In) ins(Li_2O)	12 12	$T_{\text{low}} > T_{\text{room}}$ 0
2007	[80]	$^{198}\text{Au} \beta^-$	met(Au)	12	$T_{\text{low}} > T_{\text{room}}$
2007	[105]	$^{210}\text{Po} \alpha$	met(Cu)	12	$T_{\text{low}} < T_{\text{room}}$
2007	[106]	$^7\text{Be} \varepsilon$	C_{60}^{en}	5	$T_{\text{low}} < T_{\text{room}}$
2007	[107]	$^{253}\text{Es} \alpha$	met(Fe)	4, 0.05	0
2007	[108]	$^{198}\text{Au} \beta^-$	met(Au)	19	0
2008	[109]	$^{22}\text{Na} \beta^+$	met(Pd)	15	$T_{\text{low}} < T_{\text{room}}$
2008	[110]	$^{22}\text{Na} \beta^+$	met(Al)	10	0

systematic errors. This is especially true for low temperature measurements as thermal expansion may add to the geometric source of errors. Thus, a branching ratio measurement with low systematic errors would be advantageous to clarify the usability of the model at low temperatures.

We note that in the lowest temperature measurement at 50 mK, Severijns *et al* [107] utilized a dilution refrigerator similar to ours, described in the next section.

4.3 The outlines and instrumentation of the experiment

The aim of our experiment is to measure the intensity ratio of the 596 keV and 635 keV peaks of ^{74}As embedded into different kind of materials and to observe if the ratio changes as a function of sample temperature. The technique of an intensity ratio measurement as well as the needed instrumentation is described in Chapter 3. The experiment considered here is similar, but the need for the cooling of the samples implies several changes as well. I summarize these differences in this section.

4.3.1 Cooling system

The sample temperature was monitored and controlled in a $^3\text{He}/^4\text{He}$ dilution refrigerator which was constructed by Oxford Instruments for nuclear spectroscopy measurements. It was operated by Uppsala University at the OSIRIS isotope separator on-line at Studsvik, Sweden for several years. It was re-commissioned in the Cryophysics Laboratory of Atomki in 2006. The photo of the cooling system installed at Atomki can be seen in Fig. 4.1.

The sample was attached to the cold finger of the mixing chamber of the refrigerator. The construction makes it possible to directly ‘see’ the source from outside the cryostat through a special window system with negligible attenuation of the γ rays to be observed in our experiment. The sample temperature was measured by a calibrated carbon glass resistor thermometer. Room temperature, 77 K, 4.2 K, about 1 K and about 250 mK temperatures are readily attainable with the system. Between these temperatures, one has to deal with increased temperature uncertainty. 77 K was produced by filling the cryostat of the refrigerator with liquid nitrogen and keeping 1 mbar pressure of He gas in the vacuum space (Inner Vacuum Chamber, IVC) separating the main helium bath and the dilution unit. 4.2 K was kept by filling the main helium vessel of the cryostat with liquid helium boiling at atmospheric pressure. In order to achieve a temperature around 1 K, the IVC was pumped to the pressure below 10^{-6} mbar and the pot of the refrigerator was pumped to reach a pressure of about 1 mbar, without any temperature control. The lowest temperature was produced by circulating the $^3\text{He}/^4\text{He}$ mixture in the system with the proper adjustment of the heating powers of the still and mixing chamber. A schematic view of the cooling system can be seen in Fig. 4.2.

4.3.2 Target preparation and irradiation

After the irradiation the targets are to be glued to the sample holder of the refrigerator with vacuum grease having good heat conductivity. As mylar can be damaged in low temperatures we refrained from using it in this experiment. We used Ta as metallic host and we also measured the ^{74}As peaks in the Ge target. The expected low temperature effects for these materials can be seen in Table 4.1. The same target preparation, irradiation procedure and equipment were used as in the room temperature measurements,



Figure 4.1: (left) The dilution refrigerator at the Atomki Cryophysics Laboratory. (right) The γ detector watching the cooled sample through the thin exit windows (see also Fig. 4.2).

thus the samples were similar, too. This time the sample holder was placed at a (6.5 – 7.5) cm distance from the tantalum boat into which (38 – 61) mg 99.9999 % purified germanium nuggets were placed. For backing we used 50 μm thick high purity aluminum foils. Both the germanium and Al backings were manufactured by Advent Research Materials. Four targets were prepared altogether.

Three of the produced targets were activated, one in each measurement runs. For the activation the chamber described in Section 5.3 was utilized. This time the protons provided by the cyclotron had an energy of $E_{\text{p}} = 10.4 \text{ MeV}$. The intensity of the beam was (2.4 – 5) μA . The irradiations took (6.5 – 23) h. A summary of the irradiation runs can be seen in Table 4.3.

4.3.3 γ detection

The γ measurement was performed in the Cryophysics Lab while the sample was decaying inside the refrigerator. The applicable measuring geometry was constrained by the cooling system. The γ rays created by the de-excitation of the daughter nuclei of ^{74}As could escape the chamber of the sample holder through three thin aluminum windows. The 40 % relative efficiency HPGe detector described in Section 3.6 was used to detect the γ activity of the samples. The γ detector was placed directly in front of the outmost window, the diameter of which was approximately the same as the diameter of the detector (7.9 cm). The distance between the source and the

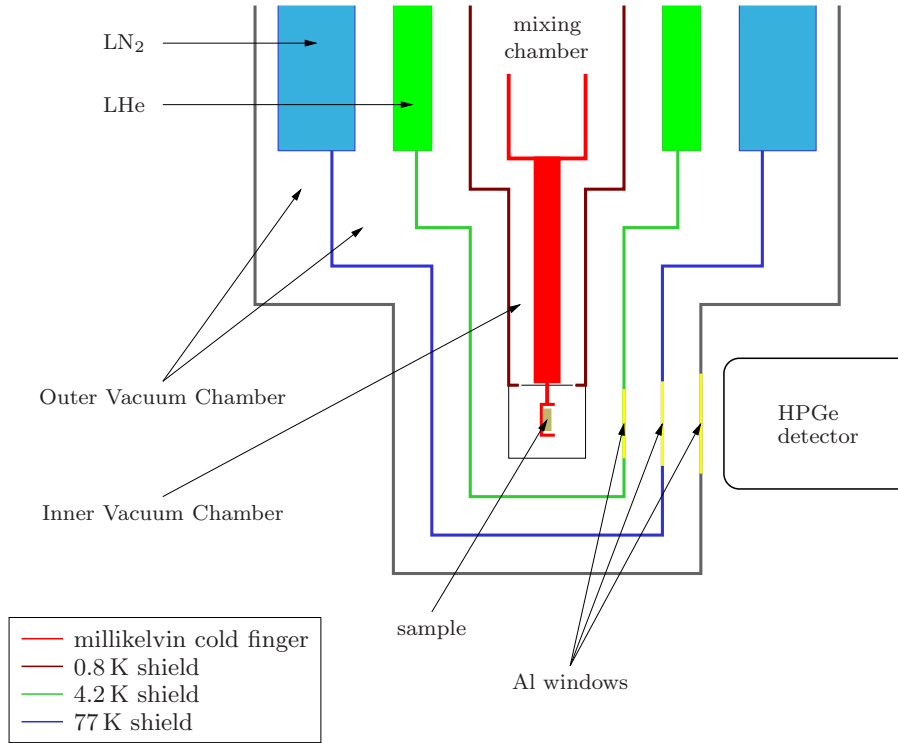


Figure 4.2: Schematic layout of the cooling system.

sensitive volume of the detector was 8.8 cm^3 . Figure 4.1 shows the detector positioned in front of the exit windows of the cooling system.

In the applied experimental arrangement it would have been impossible to build up the lead shielding around the detector as we did in the room temperature measurement. Thus, we decided to leave the detector unshielded but compensate for this disadvantage by using more active samples to get a better peak to background ratio. The initial activity of the tantalum [germanium] sample was 0.8 MBq [2.4 MBq]. The most intensive ($I_\gamma = 80\%$), 834 keV line of ^{72}As ($t_{1/2} = 26.0\text{ h}$) was detected in the germanium sample. This isotope was created from the $^{72}\text{Ge(p,n)}^{72}\text{As}$ reaction. As this isotope has a peak at 629.95 keV ($I_\gamma = 7.92\%$) which may interfere with the 635 keV peak of ^{74}As , several days were left for the decay of ^{72}As before the activity measurements com-

menced. We observed no other disturbing γ activity in the Ge sample, while we detected high energy X-rays coming from ^{181}W in the Ta samples, which was the result of the $^{181}\text{Ta}(\text{p},\text{n})^{181}\text{W}$ reaction. To decrease the summing effects and the dead time of our counting system we got rid of these X-rays by attaching a 2 mm thick lead sheet to the detector tube. This way a relatively low dead time ($\approx 1.2\%$ to 2.5% for Ge and $\approx 0.1\%$ to 0.2% for Ta) of the data acquisition system could be achieved.

Because of the geometry of the cold finger of the refrigerator only vertical source position shift is expected due to thermal expansion, with a maximum of approximately 4 mm perpendicular to the source-detector axis. To investigate the effect of such a displacement, GEANT4 [87] simulations were carried out for the 596 keV to 635 keV efficiency ratio and it was found to be constant within the statistical uncertainty of 0.05 %.

A long-term background spectrum was taken before the measurement. This, along with a typical spectrum can be seen in Fig. 4.3. A Palmtop MCA ADC and the associated software for the spectrum acquisition were used throughout the experiment, both of which were developed by Atomki.

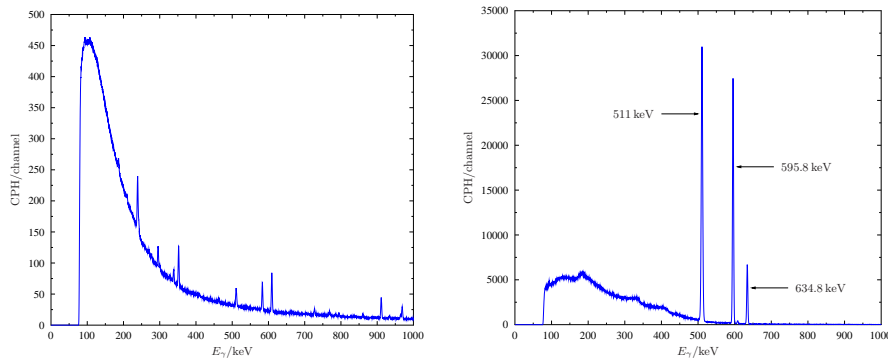


Figure 4.3: (left) Normalized (CPH) background spectrum of the Atomki Cryophysics Laboratory. The spectrum was recorded for 3.2 d. The peaks are coming from ^{212}Pb , ^{214}Pb , ^{228}Ac , ^{208}Tl , ^{212}Bi and ^{214}Bi . (right) Normalized spectrum of ^{74}As in Ge at 1350 mK 15 days after the irradiation. The spectrum was recorded for 1.7 h.

4.4 The course of the measurement and its results

4.4.1 Measurement runs

The data of the measurement runs can be seen in Table 4.3. Different targets were used for each irradiation run. The aim of the first run was to observe the intensity ratios in the highly active Ge target. The Ta host was also measured but only with higher uncertainties because of its lower activity. In the second run a high activity Ta host was measured. The third run was a check run at 77K.

Table 4.3: Data on the measurement runs. I_t shows the target current. t_{irrad} and t_{meas} denote the irradiation and measurement times, respectively. T_{lowest} is the lowest temperature at which the sample activity was measured.

Run no.	Host	$I_t/\mu\text{A}$	$t_{\text{irrad}}/\text{h}$	t_{meas}/h	$T_{\text{lowest}}/\text{K}$
1	Ge	≈ 2.4	6.5	156.4	0.316
	Ta			140.9	0.25
2	Ta	≈ 4	23	107.6	0.265
3	Ta	≈ 5	16.26	91.4	77

4.4.2 Data analysis

After the spectra were recorded they were loaded into an open source, scriptable peak fitting software, fityk [88]. Following the linear background subtraction the peaks were fitted by Gaussians. The intensity ratios were calculated from the peak areas for each spectra, and the intensity ratio I for each physical condition (i.e. host material and temperature) was taken as the error weighted mean of the intensity ratios per spectrum, with appropriate error propagation. To make the results easier to interpret we used again the normalized intensity ratio I_n . I_n is I normalized to the error weighted mean of the I of each temperature level.

In this experiment we also tried to fit the annihilation peak to separate the β^+ from ε decay, since ε decay contributes only to the 596 keV peak, while β^+ decay contributes both to the 511 keV and the 596 keV peaks. Unfortunately, there seemed to be many disturbing activities with contribution to the annihilation peak. This could be seen on the intensity ratios of the 511 keV and the ^{74}As peaks as they did not remain the same even if the

physical conditions did not vary. Thus we were unable to separate the two decay modes from each other.

4.4.3 Results

The values of I_n as a function of the temperature are summarized in Table 4.4 for ^{74}As in Ta and in Table 4.5 for ^{74}As in Ge. The results are shown in Fig. 4.4. The temperatures indicated are the mean of the temperatures of each run performed at the given temperature level. The slow drift of the cold finger temperature increases the relative error of the temperature at 1.2 K (Ta) and 1.4 K (Ge).

Table 4.4: The measured normalized intensity ratios of ^{74}As in Ta.

$\langle T \rangle / \text{K}$	$I_n / \%$
300 ± 1	99.856 ± 0.089
77.0 ± 0.5	99.82 ± 0.12
4.1 ± 0.1	100.07 ± 0.11
1.2 ± 0.2	99.95 ± 0.20
0.26 ± 0.01	100.30 ± 0.19

Table 4.5: The measured normalized intensity ratios of ^{74}As in Ge.

$\langle T \rangle / \text{K}$	$I_n / \%$
300 ± 1	100.04 ± 0.16
76.8 ± 0.5	100.098 ± 0.093
5.3 ± 0.1	99.956 ± 0.087
1.4 ± 0.2	99.98 ± 0.30
0.31 ± 0.02	99.98 ± 0.13

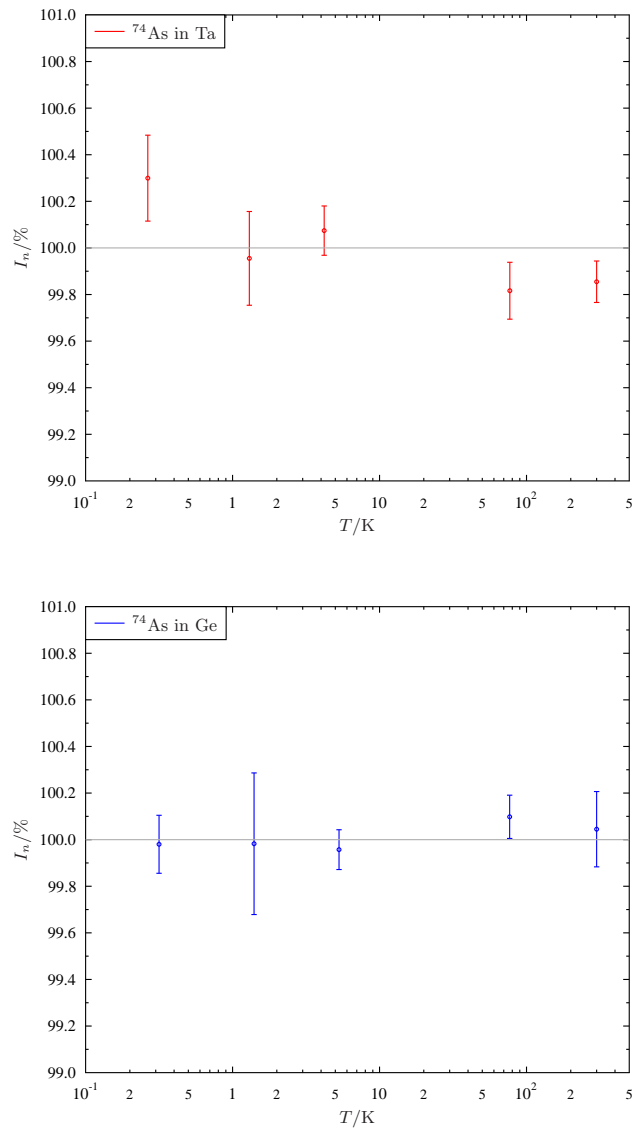


Figure 4.4: The measured normalized intensity ratio of ^{74}As in Ta (upper) and ^{74}As in Ge (lower) as a function of temperature.

4.5 Conclusions

From Tables 4.4, 4.5 and Fig. 4.4 it is very clear that our results do not support the supposed effect of the host material surrounding the decaying nuclei. This is true for temperatures ranging from room temperature down to about 0.3 K. The measured relative intensity ratios confirm this well within 2σ uncertainty, with $\sigma < 0.2\%$ in the case of Ta and $\sigma < 0.3\%$ in the case of Ge host.

Even if there was a change smaller than our precision in the intensity ratios, it is clear that the Debye-model is unable to describe the variation. In Fig. 4.5 the prediction of the Debye–Hückel model based calculations to the normalized peak intensity ratios as a function of temperature can be compared with the intensity ratios obtained from our measurement. Even our previous experiment (described in Chapter 3) showed that the possible effect has to be less than half the predicted one at room temperature. With the increased precision of the new experiment the applicability of the model can clearly be excluded. The deviation of the predicted and measured ratios becomes even larger when moving to lower temperatures, and they are off by orders of magnitude reaching the sub-kelvin regime. On these grounds, we take the applicability of the Debye-model to the prediction of screening effects on radioactive half-lives at and below room temperature rejected.

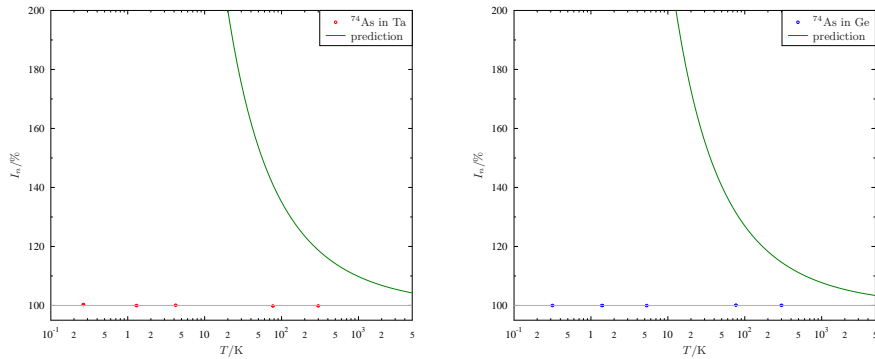


Figure 4.5: The measured normalized intensity ratio of As in Ta (left) and As in Ge (right) as a function of temperature ($0.1\text{ K} < T < 5000\text{ K}$). The green curve indicates the predicted effect. The error bars of the measured points are tiny beyond visibility.

Participation of the author. I played a key role in the experiment. I participated in the target preparation, in setting up the instruments, the irradiation and the recording of the spectra. I performed the complete analysis of the data from the peak fitting to preparing the final results. I wrote a paper, a proceedings and a popular article about our measurement and gave a talk at an international conference.

Comparison of our work to the literature. Let us place our room temperature and low temperature experiments among the recently published measurements. Table 4.6 summarizes the papers published after the publications of Table 3.1 and Table 4.2.

Table 4.6: Most recent literature dealing with the effect of electron screening on radioactive half-lives. Our publications are set in bold. For notations see Table 3.1. 300 K stands for uncontrolled room temperature.

Date	Ref.	Source	Environment	T/K	$t_{1/2}$
2008	[111]	$^{7}\text{Be} \varepsilon, ^{198}\text{Au} \beta^-$	met(Cu,Al-Au)	0.35–293	0
2008	[112]	$^{74}\text{As} \beta^\pm \varepsilon$	met(Ta,Al)	300	0
			sem(Ge), ins	300	0
2008	[113]	$^{64}\text{Cu} \beta^\pm \varepsilon$	met(Cu)	12	0
2009	[114]	$^{198}\text{Au} \beta^-$	met(Au)	12	$T_{\text{low}} > T_{\text{high}}$
2009	[115]	$^{109}\text{In} \varepsilon, ^{110}\text{Sn} \varepsilon$	met(Pb,Au)	300	Au > Pb
2009	[116]	$^{74}\text{As} \beta^\pm \varepsilon$	met(Ta)	0.26–300	0
			sem(Ge)	0.26–300	0
2009	[117]	$^{97}\text{Ru} \varepsilon$	met(Ru)	19	0
		$^{103}\text{Ru} \beta^-$	met(Ru)	19	0
		$^{105}\text{Rh} \beta^-$	met(Ru)	19	0
2010	[118]	$^{7}\text{Be} \varepsilon$	met(Pt,Al)	300	Al < Pt
2010	[119]	$^{210}\text{Po} \alpha$	met(Ag)	4	0

Ref. [111] were published while our room temperature paper was under review and our low temperature experiment was in progress. This experiment was very similar to ours, the main difference being is that Kumar *et al* measured the relative intensity ratio of the 412 keV γ peak of ^{198}Au and the 478 keV peak of ^7Be . They came to the same conclusion as we did. In this sense our experiment confirms the results of Ref. [111], but we performed the measurement on a single isotope (which is better for reducing the systematic uncertainties) and we also used a semiconductor as host

material.

Parallel to the experiments checking the validity of the Debye-model other screening theories were born. These are based on the Thomas–Fermi screening model (e.g. [103]), Hartree’s method (e.g. [63]) or TB-LMTO (Tight Binding Linear Muffin-tin Orbital method, e.g. [63]) calculations. These models predict minor screening effects and minor or no temperature dependence. We do not go into the details of these competing theories because the effect predicted by them are so small that their unambiguous verification is beyond the possibilities of current measuring techniques and instrumentation.

Publications.

Scientific paper

J. Farkas, Gy. Gyürky, C. Yalçın, Z. Elekes, G. G. Kiss, Zs. Fülöp, E. Somorjai, K. Vad, J. Hakl and S. Mészáros, *Measurement of embedded ^{74}As decay branching ratio at low temperatures*, J. Phys. G **36**, 105101 (2009)

Conference proceedings

J. Farkas, Gy. Gyürky, C. Yalçın, G. G. Kiss, Z. Elekes, Zs. Fülöp, E. Somorjai, K. Vad, J. Hakl and S. Mészáros, *Study of ^{74}As decay in different host materials and at different temperatures*, PoS NIC X (2009)

Conference talk

J. Farkas, Gy. Gyürky, C. Yalçın, Z. Elekes, G. G. Kiss, Zs. Fülöp, E. Somorjai, K. Vad, J. Hakl and S. Mészáros, *Temperature dependence of β^- and β^+/ε decay branching ratio of embedded ^{74}As* . European Nuclear Physics Conference, EuNPC. Bochum, Germany, 16 – 20 March, 2009

Conference poster

Gy. Gyürky, **J. Farkas**, C. Yalçın, G. G. Kiss, Z. Elekes, Zs. Fülöp, E. Somorjai, K. Vad, J. Hakl and S. Mészáros, *Study of ^{74}As decay in different host materials and at different temperatures*. 10th International Symposium on Nuclei in the Cosmos, NIC X. Mackinac Island, Michigan, USA, 27 July – 1 August, 2008

Popular article

J. Farkas, *Változik-e a radioaktív atommagok felezési ideje?* (Do the half-lives of radioactive nuclei change?) [in Hungarian], Természet Világa **142**(3) 135 (2011)

Chapter 5

High precision lifetime determination of ^{133m}Ce and ^{154m}Tb with γ spectrometry

In this chapter I describe the methods and the results of the half-life measurement of the lowest energy metastable states of ^{133}Ce and ^{154}Tb . In the first two sections I give our motivations by describing the astrophysical γ -process and the experimental cross section determination by target activation. In Section 5.3 I go into the details of the half-life measurement of ^{133m}Ce , while the ^{154m}Tb lifetime measurement is reviewed in Section 5.4. The chapter ends with the summary of the results and the drawing of the conclusions.

5.1 The astrophysical γ -process

As I mentioned in the introductory chapter, heavy elements are synthesized by various processes of presupernovae or supernova explosions. These processes include the s-process (slow neutron capture), the r-process (rapid neutron capture), the rp-process (rapid proton capture), the γ -process (photodisintegration) and ν -process (neutrino-induced reactions). It is thought that the combined effect of these processes should be responsible for the heavy element abundances observed in the Universe [8].

Neutron capture processes produce isotopes on the neutron-rich side of the valley of stability. Such unstable isotopes decay back to stable elements

through decay chains consisting mostly of β^- decays. There are some stable isotopes on the proton-rich side of the stability valley which cannot be reached from the neutron-rich side by successive β^- decays, since they are ‘shielded’ by the valley of stability. There are 35 such proton-rich stable isotopes, called p-isotopes or p-nuclei, ranging from ^{74}Se (see Fig. 5.1) to ^{196}Hg [8]. The abundance of these isotopes are about a hundred times less than the abundance of their neighboring stable isotopes produced by the s- and/or r-process, indicating a different mechanism for their creation [8]. The astrophysical process synthesizing p-isotopes are historically called the p-process [92].

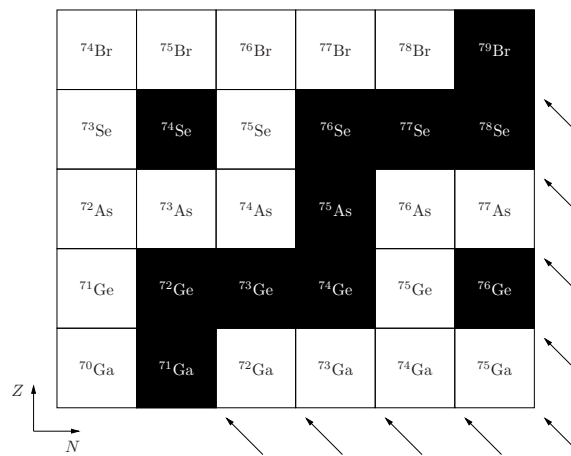


Figure 5.1: The location of ^{74}Se , the lightest p-isotope on the chart of the nuclides. Black boxes show the stable isotopes, the valley of stability being in the middle. The arrows show the direction of the β^- decay.

Nuclei produced by neutron capture processes can serve as seed nuclei for p-isotope production, which proceeds through photon induced, proton capture and neutrino induced reactions. It has been shown though that proton capture reactions (the rp-process) need special astrophysical environments (such as type I X-ray bursts) [8, 93, 94] which makes it very unlikely for large amounts of the produced nuclei to escape to interstellar space. Thus photodisintegration should be responsible for most of the observed p-isotope abundances (that is why the p-process is also called the γ -process). Solar System abundances of the p-isotopes could not have been

reproduced well in the Mo–Ru region and in the $A \in \{150, \dots, 167\}$ mass region [95] yet. The solution of this problem (i.e. examining the possible effect of the νp -process, changing the nuclear physics parameters or looking for other astrophysical scenarios as candidates for possible sources of p-isotope production) is still under debate [102]. The dominant reaction of the γ -process is the (γ, n) reaction, though as the reaction products move towards the proton drip line, (γ, p) and (γ, α) reactions become more probable, introducing branching points into the γ induced reaction paths [8].

The exact course of the changing of stellar composition can be investigated by means of computer simulation. The simulations monitor both the changes of the astrophysical environment (such as stellar temperature, pressure, density and opacity) and the element abundances. For the latter, the codes need nuclear physics input in the form of nuclear reaction rates and decay data. The simulational results also depend on the initial conditions, like the seed nucleus distribution. In the case of p-process simulations, where the astrophysical conditions (i.e. stellar explosions) assume an extended past of the system, these initial conditions can be taken from other simulations (like s-process codes). p-process simulations need vast reaction networks including heavy element reaction data, which mean tens of thousands of reactions on elements from hydrogen to bismuth [95, 96]. Obviously, these reactions have only been partially investigated experimentally, the majority of the reaction rates data come from model calculations. For example, the Hauser–Feshbach statistical model can be used to get heavy element reaction rates [97, 98]. The lack of experimental data makes nuclear reaction measurements in the astrophysically relevant energy range invaluable. The experimental results can directly be used as simulation input, while they also help to constrain and improve theoretical predictions [99].

5.2 Cross section measurements for the γ process

The most direct method to measure the $Y(\gamma, A)X$ reaction cross section is to bombard Y with intense γ radiation. This is usually hard to carry out, because of multiple reasons:

- Due to the high penetrability of γ rays the target needs to be thick,

making it hard to obtain enough enriched material.

- The production of γ beams needs special equipment. For this purpose, usually synchrotron as bremsstrahlung source is used.
- The distribution of the energy of the incident γ rays are usually wide, even after energy filtering. This makes the cross sections hard to calculate.
- The intensity of the γ beams are usually relatively low.
- Thermal excitations of the target in the stellar plasma lead to a strong modification of the laboratory cross section which has to be estimated from theory [100].

If one has to measure the most common (γ,n) , (γ,p) or (γ,α) reactions, it is usually possible to carry out a more feasible experiment, i.e. to bombard X by neutrons, protons or α particles and measure the cross section of this inverse reaction. The cross sections of the $\text{Y} + \gamma$ reactions can then be calculated by using the reciprocity theorem [8].

5.2.1 The activation method

Activation is a standard method to measure the cross section of nuclear reactions. To perform an activation measurement, one has to prepare the target from material X then irradiate it with the help of an accelerator. Let's say we are curious about the $\text{Y}(\gamma,p)\text{X}$ reaction cross section. Then we irradiate X with protons, and some of the protons will be captured in the $\text{X}(p,\gamma)\text{Y}$ reaction. If one knows the intensity of the incident beam (i.e. the flux of the incoming particles as a function of time), the decay rate of the created Y nuclei and the time elapsed since the end of the irradiation, then the cross section can be calculated from the measured activity of the reaction product.

Of course, this method can only be used if X is stable and a target can be made out of it, and if the reaction leads to a radioactive isotope with a reasonable half-life. The attempt to analyse the spectra can fail if there are parasitic reactions occurring on the target isotopes or on the contaminants, especially if the cross sections of such reactions are much higher than the reaction to be examined. If for some reason (like because of the reaction

daughter is stable) the cross section cannot be measured with activation, another experimental method, e.g. an on-line or an AMS measurement has to be utilized, if possible.

Let $N(t)$ denote the number of the Y nuclei at time t . During the irradiation the reaction product is continuously created in a rate given by the number of seed nuclei X in the target, the flux of the incoming particles and the cross section. Concurrently they decay with a rate characterized by the decay constant λ . $N(t)$ goes to saturation after irradiating the target for a few half-lives [9].

When the irradiation stops at time $t = 0$, the $N_0 := N(0)$ number of nuclei decreases according to the decay law eq. (2.2)

$$N(t) = N_0 e^{-\lambda t}.$$

We record the γ spectrum of the source in the time interval $[t_0, t_1]$, $\Delta t = t_1 - t_0$. By measuring the counts in one or more characteristic γ lines of the decay, the number of the decayed nuclei D can be given if the relative intensity of the given γ line is known and the absolute efficiency of the detector has previously been determined.

$$D = -\Delta N = N(t_0) - N(t_1) = N_0(e^{-\lambda t_0} - e^{-\lambda t_1}) = N_0 e^{-\lambda t_0}(1 - e^{-\lambda \Delta t}) \quad (5.1)$$

From this, the created number of nuclei N_0 can be obtained, and the cross section calculated.

5.2.2 When the half-life is incorrect

In a precise measurement many spectra are taken in the time intervals $[t_0, t_1]$, $[t_2, t_3]$, $[t_4, t_5]$, etc... If the decay constant λ is well known, then the calculated initial number of the created nuclei $N_0^{[t_{2i}, t_{2i+1}]}$ fluctuate around N_0 . However, if the applied decay constant is not precise compared to the precision of the measurement, then the $N_0^{[t_{2i}, t_{2i+1}]}$ values have a tendency to decrease/increase with time, depending on the difference of the real and the known decay constant values (see Fig. 5.2).

Moreover, eq. (5.1) also shows that the uncertainty of λ propagates into the calculated value of N_0 . Thus it is also desirable to use a precise value of the decay constant to reduce the final uncertainty of the obtained cross section value.

In order to augment our knowledge of the astrophysical γ -process and the theoretical reaction cross section models, our group planned to measure the cross sections of the $^{130}\text{Ba} + \alpha$ and $^{151}\text{Eu} + \alpha$ reactions by target activation. An accurate estimation of the created reaction products necessitates the precise knowledge of the reaction product half-lives. The literature half-lives of ^{133m}Ce (from the $^{130}\text{Ba}(\alpha, n)^{133m}\text{Ce}$ reaction) and ^{154m}Tb (from the $^{151}\text{Eu}(\alpha, n)^{154m}\text{Tb}$ reaction) were not appropriate for our purposes. Thus we had to measure these half-lives before we could proceed with the evaluation of the cross section experiments.

The following sections contain the details of these half-life measurements. As the technique and instrumentation used in these experiments were similar, I only go into the details of the cerium measurement, while the terbium experiment will only be briefly summarized.

5.3 The determination of the half-life of ^{133m}Ce

5.3.1 Motivation

To measure the cross section of the $^{130}\text{Ba}(\alpha, n)^{133m}\text{Ce}$ reaction by activation, one needs the lifetime of the ^{133m}Ce isomer. The literature value of the half-life is $t_{1/2}^{\text{lit}} = (4.9 \pm 0.4)$ h. This value is based on a single measurement from 1967 [120]¹. On the one hand, this half-life value has a rather high relative uncertainty (more than 8 %). On the other hand, our preliminary measurements clearly showed an upgoing tendency in the calculated number of the created reaction products, indicating that the literature half-life is underestimated (see Fig. 5.2). In order to supply our cross section measurement with a suitable half-life value, we measured the half-life of ^{133m}Ce .

5.3.2 Target preparation

Four barium targets were prepared for activation using the evaporator shown in Fig. 3.3. Barium carbonate (BaCO_3) enriched in ^{130}Ba ($(11.8 \pm 0.2)\%$, which is about 100 times the natural abundance, see Table 5.1) was evaporated onto thin aluminum foils. The thickness of the evaporated layer was

¹According to Ref. [121], the new literature value is $t_{1/2}^{\text{lit}} = (5.1 \pm 0.3)$ h. The new evaluation came out just before we published our results.

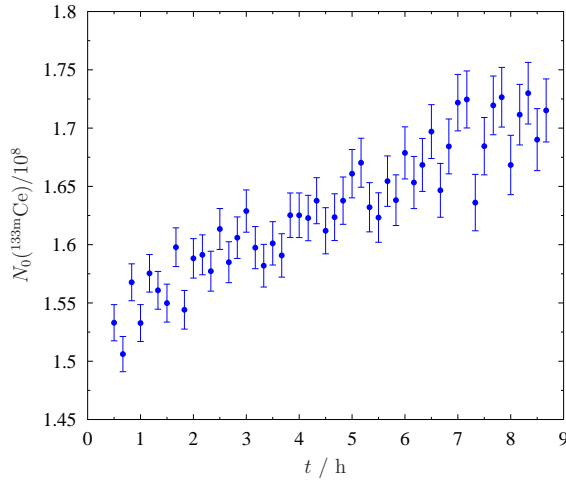


Figure 5.2: The effect of using an underestimated half-life value in the calculation of the number of reaction products. t shows the time elapsed from the end of the irradiation to the center of the spectrum recording time interval $[t_{2i}, t_{2i+1}]$. This plot served as motivation for the precise half-life measurement of ^{133m}Ce (literature $t_{1/2} = 4.9 \text{ h} \pm 0.4 \text{ h}$).

measured by weighing, and was found to vary from about $200 \mu\text{g}/\text{cm}^2$ to $400 \mu\text{g}/\text{cm}^2$.

5.3.3 The activation chamber

The targets were placed into an activation chamber, the schematics of which can be seen in Fig. 5.3. The same chamber was used in our ^{74}As γ intensity ratio measurements (see Chapter 3 and Chapter 4). This chamber was designed to be suitable not only for isotope production but also to measure reaction cross sections with the activation method.

Our chamber can be separated from the rest of the accelerator vacuum space with a built-in gate valve. The chamber can be exhausted to pre-vacuum with its own pump. This combination makes it possible to change the targets without venting a larger portion of the beamline. A vacuum in the order of 10^{-6} mbar was maintained in the chamber.

The incoming beam goes through a tantalum collimator ring before colliding into the target. The current on both the collimator and the target can be measured in order to help adjusting the beam and to measure the

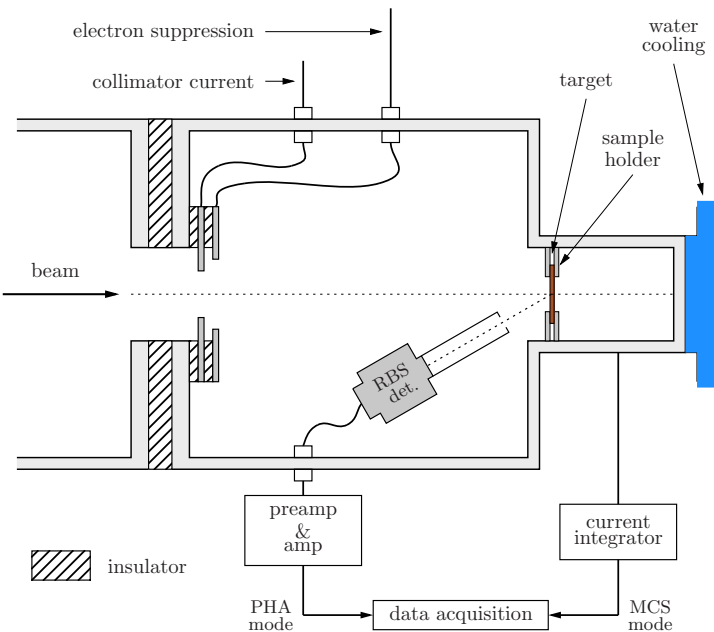


Figure 5.3: Schematics of the activation chamber. PHA: Pulse Height Analysis, MCS: Multichannel Scaling, RBS: Rutherford BackScattering.

number of particles arrived at the target. To make the current measurement reliable, one has to take care of the secondary electrons ejected due to beam impact. In our case this is done by applying -300 V electron suppression voltage on a ring placed behind the collimator.

In some experiments the target shall be cooled. There are various end caps applicable to our chamber, and the cooling possibilities depend on the cap attached. When air cooling is used, a blower is fixed on the chamber end. A more efficient option is water cooling; some caps can be connected to the water cooling system of the accelerator.

To monitor target stability, the RBS (Rutherford backscattering) spectrum of the target was followed on-line by using the chamber's built-in surface barrier silicon detector. This detector is fixed at 150° angle from the beam direction and it is equipped with its own collimator.

After the precise half-life of ^{133m}Ce was determined, the same chamber was used for the activation cross section measurement of the $^{130}\text{Ba} + \alpha$ reactions [122].

5.3.4 Irradiation

The targets were irradiated with α particles at the cyclotron of Atomki. 14 MeV, 14.5 MeV, 15 MeV and 15.5 MeV α beams with $2\mu\text{A}$ current were applied. The irradiation times can be seen in Table 5.2. The transmutation tree of α induced reactions on ^{130}Ba can be seen in Fig. 5.4.

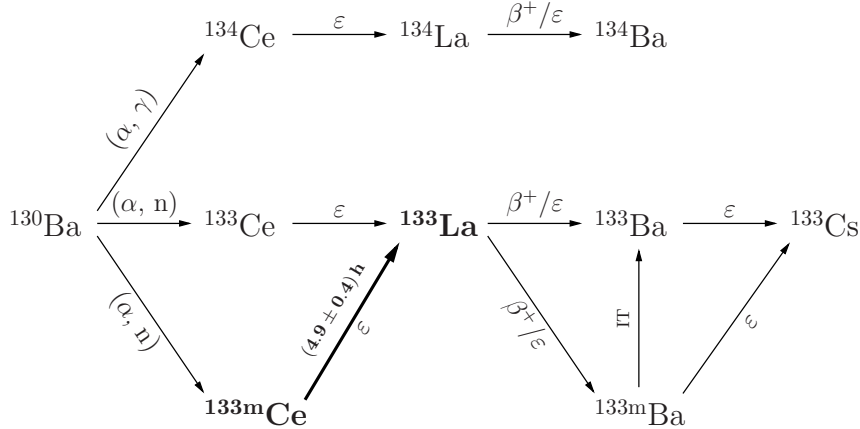


Figure 5.4: The isotopes created by the $^{130}\text{Ba} + \alpha$ reactions. The (α, p) reaction has been omitted as it plays no role in our measurement. $t_{1/2}(^{134}\text{Ce}) = 3.16\text{ d}$, $t_{1/2}(^{134}\text{La}) = 6.45\text{ m}$, $t_{1/2}(^{133}\text{Ce}) = 97\text{ m}$, $t_{1/2}(^{133}\text{La}) = 3.91\text{ h}$, $t_{1/2}(^{133}\text{Ba}) = 10.51\text{ y}$, $t_{1/2}(^{133m}\text{Ba}) = 38.9\text{ h}$.

Besides the isotopes indicated in Fig. 5.4, many other radioactive elements were created from the contaminants of the target (see Table 5.1). The detected γ rays emitted by the isotopes (including the disturbing contaminants) are detailed in the analysis subsection.

5.3.5 γ detection

After the irradiation the sources were transported to the γ counting room, where they were placed in front of a 100 % relative efficiency Canberra HPGe detector (model GR10024). The energy resolution of the detector was around 2.3 keV FWHM at 1332 keV. The sources were placed 10 cm away from the sensitive surface of the detector so as to reduce the coincidence summing effect. The high activities caused a relatively high initial dead-time (3 %–19 %), which decreased to negligible amounts till the end of the measurement runs. The dead-time was taken from the counting system,

Table 5.1: Composition of the target. Only the components having radioactive products with high γ intensity are shown (the 133m Ce peaks have been omitted). The disturbing γ lines are results of the (α, n) and (α, γ) reactions on the given isotopes (except the gammas of 24 Na, which come from 23 Na + n). The abundances are provided by the manufacturer (Isoflex USA).

Isotope/Element	Content	(α, n)	$t_{1/2}$	E_γ/keV
^{130}Ba	11.8 %	^{133}Ce	97 m	557.7, ...
^{132}Ba	0.7 %	^{135}Ce	17.7 h	265.6, 783.6, ...
^{134}Ba	4.0 %	^{137}Ce	9.0 h	447.2, 254.3, ...
^{136}Ba	8.3 %	^{139}Ce	137.6 d	165.9
^{138}Ba	56.6 %	^{141}Ce	32.5 d	145.4
^{92}Mo	unknown	^{95}Ru	1.64 h	336.4, 1096.8, ...
^{23}Na	unknown	^{24}Na	14.96 h	1368.6, 2754.0
Cu	175 ppm	^{66}Ga	9.49 h	1039.2, 2751.9, ...
Fe	270 ppm	^{57}Ni	35.6 h	1377.6, 1919.5, ...

which had previously been tested for precision with the help of a pulser (see Section 5.4).

The detector and the sample was surrounded with a 4π Low Background (LB) multilayered shielding (Tema Sinergie Mod GDS 2) to minimize background. At the relevant energy ranges the background of the empty lead chamber was typically less than 10 % of the background with the source present, at any time of the measurement. We used Ortec electronics with Ortec MAESTRO data acquisition software. The photo of the sample placed in front of the detector is shown in Fig. 5.5. A background spectrum can be seen in Fig. 5.6.

After the irradiation, a few minutes were spent with transporting the newly activated sources to the detector. The γ detection was performed in three steps. 50 spectra with 10 minutes real time were recorded to follow the decay-out of the short-lived isotopes, most importantly the ground state ^{133}Ce . Then several 1 h spectra (13 – 54, see Table 5.2) were saved before a new sample was inserted into the sample holder. Finally, a few 1 d spectra were taken to identify the isotopes with longer lifetimes, and to help subtract

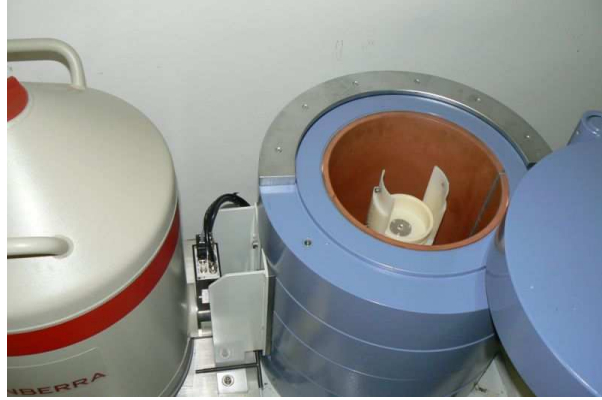


Figure 5.5: The sample in front of the detector.

their contribution from the earlier spectra, if necessary. This was needed in case of one of the peaks, as we will see. A typical spectrum is shown in Fig. 5.6.

Table 5.2: Data of the measurement runs: E_α is the bombarding α energy, I_t is the target current, t_{irrad} is the irradiation time and t_{meas} is the time of the spectrum recording, where the short (10 m and 1 h) runs and the long follow-up measurements are written separately.

E_α/MeV	$I_t/\mu\text{A}$	$t_{\text{irrad}}/\text{h}$	t_{meas}
14.0	2	20.73	62.35 h
14.5	2	9.95	21.34 h
15.0	3	21	43 h + 17 d
15.5	2	7.17	22.34 h + 4 d

5.3.6 Data analysis

The most easily identifiable γ peaks of ^{133m}Ce can be seen in Table 5.3 and Fig. 5.7. Some of these peaks could not have been taken into account in the final analysis because of various reasons. We found that a significant amount of ^{135}Ce was produced in the $^{132}\text{Ba}(\alpha, n)^{135}\text{Ce}$ reaction. This isotope decays by emitting 783.6 keV γ rays, contributing heavily to the 784.6 keV ^{133m}Ce peak. This effect could not be corrected for due to the poor count rate in the peak. The 1494.9 keV and the 1500.4 keV peaks were also rejected. These two peaks overlapped in a small region and could only be fitted as double

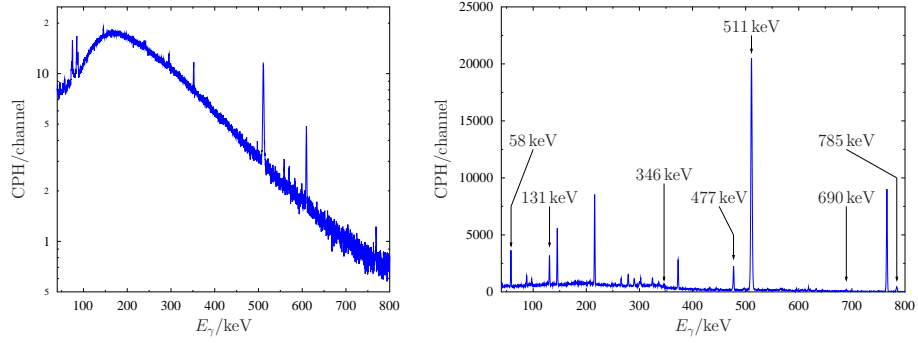


Figure 5.6: (left) Normalized (1 h) low energy background spectrum of the detector with closed shielding. (right) A typical 1 h spectrum ($E_\alpha = 14.5 \text{ MeV}$, $t/h \in [11.34, 12.34]$) showing the annihilation and the relevant ^{133m}Ce peaks.

peaks. Such a fitting has a much greater error than a single fit, making the uncertainties too high for our purposes. There was a similar problem in the case of the 477.2 keV peak, which contains a sub-peak of ^{133m}Ce at 475.5 keV. This problem was overcome by acquiring the summed area of the two peaks by integrating the counts instead of fitting. The success of using this procedure lies in the high intensity of the 477.2 keV peak, which made the relative error of the area much lower than in the case of the twin peaks at around 1500 keV. The low energy region of a typical spectrum is shown in Fig. 5.8. As it can be seen, the spectra contain many peaks since both the ^{130}Ba and the target contaminants were activated.

Due to the response function of the detector the peaks showed moderate tailing [3]. In order to have accurate results we fitted our peaks with exponentially modified Gaussian (EMG) functions (see Fig. 5.9). EMG described our peaks with much better χ^2 values than Gaussians and they have only one more parameter than normal distribution. The automated fitting of the more than 200 spectra was performed by fityk [88], using the Levenberg–Marquardt fitting method. After the fitting of the peaks, the poor quality fits (if either the background or the peak fit having $\chi^2_{\text{red}} > 2.5$, which is about 14 % of the fits) were rejected. The threshold of the rejection was determined empirically by analysing several spectra. The decay curve fits were performed on a minimum of 9, maximum of 17 one hour spectra.

The determination of the half-life was made by fit a linear curve on the semi-logarithmic plot of the intensities of the γ peaks as a function

Table 5.3: The most visible peaks of ^{133m}Ce that have been considered in the determination of the half-life [131]. See the text for more details on their contribution to the final result. I_γ denotes the relative intensity.

Transition						
E_γ/keV	I_γ	$E_{\text{level}}/\text{keV}$	$J\pi$	\rightarrow	$E_{\text{level}}/\text{keV}$	$J\pi$
58.4	19.2 %	535.604	11/2-	\rightarrow	477.224	9/2+
130.8	17.9 %	130.803	7/2+	\rightarrow	0.	5/2+
346.4	4.16 %	477.224	9/2+	\rightarrow	130.803	7/2+
475.5	3.18 %	563.35	9/2+	\rightarrow	87.939	5/2+
477.2	39 %	477.224	9/2+	\rightarrow	0.	5/2+
689.5	4.12 %	1735.46	11/2-	\rightarrow	1045.945	9/2-
784.6	9.64 %	784.552	7/2-	\rightarrow	0.	5/2+
1494.9	3.21 %	2036.04	7/2-	\rightarrow	541.2	7/2+
			9/2-			
1500.4	4.74 %	2036.04	7/2-	\rightarrow	535.604	11/2-
			9/2-			

of time. The result of such a fitting can be seen in Fig. 5.10. In most cases either short or long living (or both) contaminants were observed in the decay curves. The effect of the contaminants was also observable in the background areas under the peaks (see Fig. 5.10). The spectra taken in the contaminant-affected time intervals were left out from the fit. The examination of the 1 d spectra taken a few days after the irradiation revealed three small peaks with energies around 57.5 keV. These were identified as X-ray peaks, the source of which was tantalum excited by the radiation of the created unstable isotopes (the origin of the tantalum is uncertain). This peak increased the count rate of the 58.4 keV peak. The 1 d spectra made the correction for this available: the contribution of these peaks were subtracted, with taking into account an overestimated uncertainty (30 % – 50 % of the peak area). The 346.4 keV and the 689.5 keV peaks were also evaluated, but were omitted from the final results due to their high relative errors caused by low intensity. Finally, we checked the selected time intervals by fitting a decay curve to their first and second halves. The obtained half-life values agreed within their uncertainties.

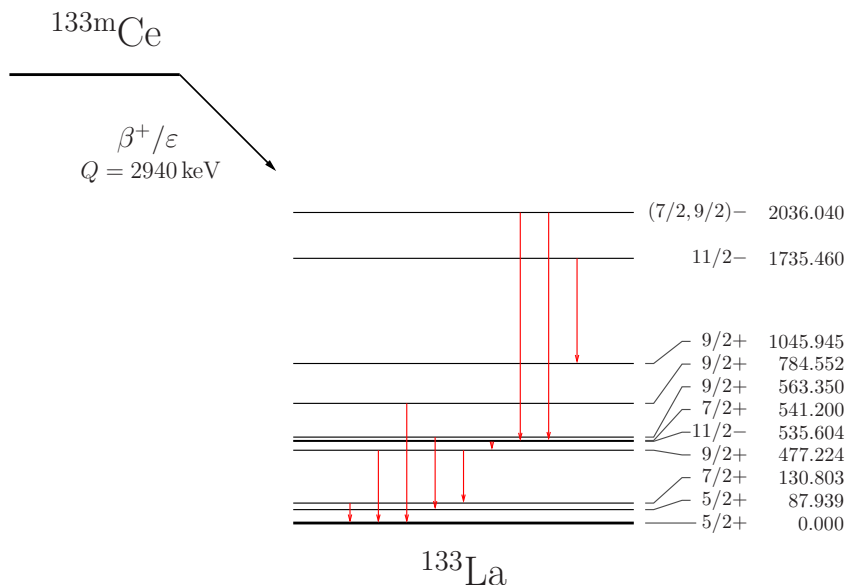


Figure 5.7: The most visible γ rays coming from the de-excitation of ^{133}La , which is the decay product of ^{133m}Ce .

5.3.7 Results

The half-lives obtained from the analysis of the 58.4 keV, 130.8 keV and 477.2 keV peaks of the four sources can be seen in Table 5.4 (the 58.4 keV peak of the 15.0 MeV target was not measured due to technical problems). The χ^2_{red} column shows the reduced χ^2 values of the fits of the decay curve. Particular care was taken to avoid any systematics in the deviance from the fitted decay curve (see for example Fig. 5.10) which would suggest the presence of contaminants in the peak. From the high χ^2_{red} values one can infer that the peak area errors are underestimated. The main reason for this is that the parameters of the fitted curves are not scaled by $\sqrt{\chi^2_{\text{red}}}$. It is also clear that the peak area error of the 477 keV peaks is underestimated, since the area of these peaks was determined by summing instead of fitting. From the physical side, it is most likely that the source of uncertainty lies in the congestion of the spectra – there are so many peaks, that one can only use a few channels for background fitting, making the background fits less reliable. These problems are treated as sources of systematic error, the measure of which is approximated by the χ^2 values themselves. To take this

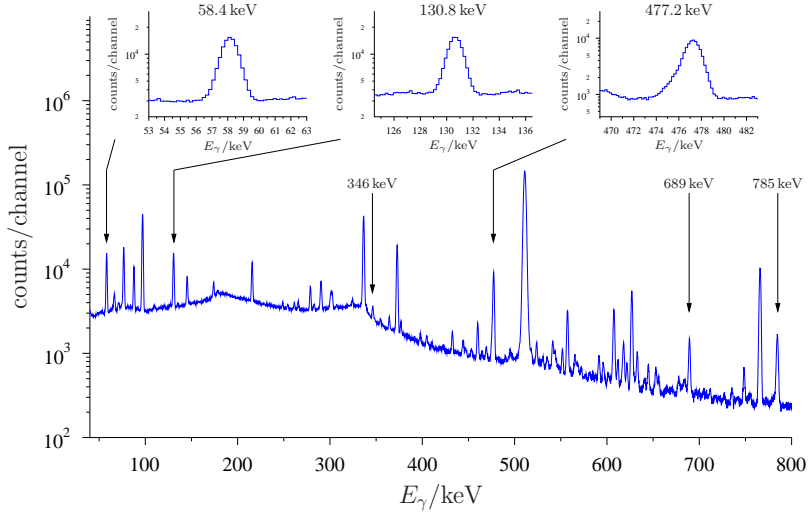


Figure 5.8: A one hour γ spectrum measured soon after the end of a 10 h irradiation by a 14.5 MeV α beam. Only the relevant energy region is shown, with the most important peaks of ^{133m}Ce in the insets. The 477.2 keV peak is asymmetric due to the presence of a sub-peak at 475.5 keV (see the text and Table 5.3 for details).

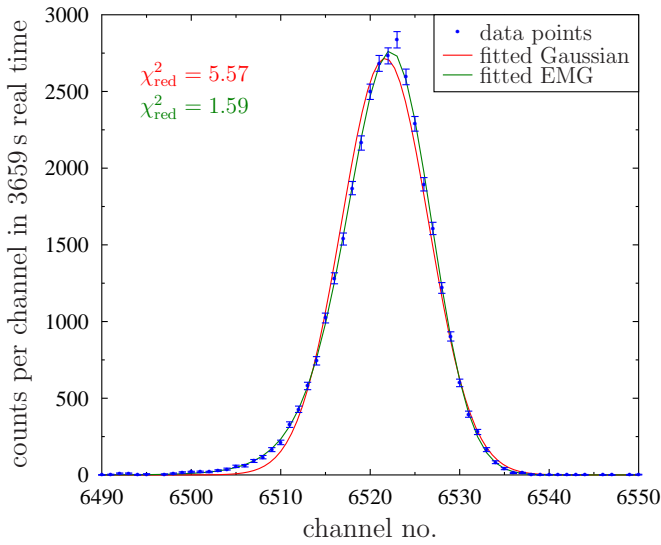


Figure 5.9: Peak asymmetry test on the 1332 keV γ peak of ^{60}Co [3]. The tailing is well approximated by EMG.

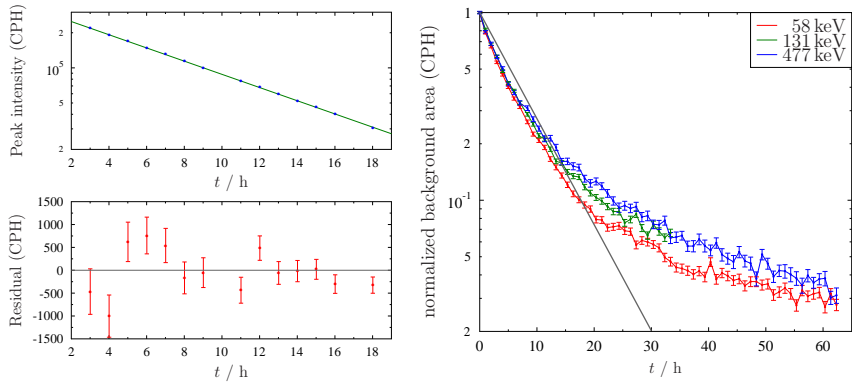


Figure 5.10: (left) The result of an exponential decay curve fit of 14 one hour spectra ($E_\alpha = 15 \text{ MeV}$, 477.2 keV peak). The activity is given in counts per hour (CPH). The shown fit has the highest χ^2 value among the results ($\chi^2_{\text{red}} = 1.96$). (right) The variation of the background in the region of the peaks with time. For comparison an exponential decay curve with the recommended half-life of ^{133m}Ce is shown (gray line). $E_\alpha = 14 \text{ MeV}$.

effect into account, all the error in Table 5.4 have been scaled up by a factor of $\sqrt{\chi^2_{\text{red}}}$.

The results can be compared in Fig. 5.11. The error weighted mean of the evaluated half-lives is $t_{1/2} = (5.3261 \pm 0.0052) \text{ h}$ with $\chi^2_{\text{red}} = 1.56$. The evaluation was repeated on a subset of the data with using Gaussian fits instead of EMG. A maximum of 0.009 h difference was found in the half-lives obtained from the different fits, which is treated as systematic uncertainty and is added quadratically to the $\sqrt{\chi^2_{\text{red}}}$ increased uncertainty of the error weighted mean. The width and the position of the fitting window can also introduce uncertainties to the final result. Unfortunately, we did not have much freedom on how we set our background model or where we fix our fitting window. As our spectra was crowded with peaks we could only use a few channels on each side of a peak to fit the background. As I mentioned earlier, we payed attention to the quality of the background fits (i.e. to fits where the points of the background window ‘climbed up’ a neighboring peak) by omitting suspicious peaks having high background χ^2_{red} from the half-life fit. Let us note in general, that the high number of γ lines coming from the products of the $^{130}\text{Ba} + \alpha$ reaction prohibits us to vary the background parameters and the use of an additional high intensity calibration source

Table 5.4: The half-life values extracted from the γ peaks of the four sources. The errors are already multiplied by $\sqrt{\chi^2_{\text{red}}}$, given that $\chi^2_{\text{red}} > 1$.

$E_{\text{beam}}/\text{MeV}$	E_{γ}/keV	χ^2_{red}	$t_{1/2}/\text{h}$
14.0	58.4	1.46	5.332 ± 0.048
	130.8	1.40	5.29 ± 0.11
	477.2	1.76	5.278 ± 0.022
14.5	58.4	0.96	5.339 ± 0.014
	130.8	1.48	5.254 ± 0.047
	477.2	1.76	5.314 ± 0.020
15.0	130.8	1.41	5.301 ± 0.017
	477.2	1.96	5.320 ± 0.014
15.5	58.4	1.31	5.344 ± 0.012
	130.8	1.56	5.362 ± 0.029
	477.2	0.97	5.331 ± 0.012

would increase the background, which we wanted to avoid. The robustness of our final result is mainly based on the fact that we acquired it by analysing three peaks with completely different backgrounds. As it can be seen in Fig. 5.11, the obtained half-lives agree within 2σ uncertainty.

Therefore, it is recommended to use the $(5.326 \pm 0.011)\text{ h}$ value as the half-life of ^{133m}Ce . This value is in agreement with the old literature value of $(4.9 \pm 0.4)\text{ h}$ but it has much less uncertainty. It also solves the cross-section measurement problem shown in Fig. 5.2.

5.4 The determination of the half-life of ^{154m}Tb

Motivation. We planned to measure the reaction cross sections of the reactions $^{151}\text{Eu}(\alpha,\gamma)^{155}\text{Tb}$ and $^{151}\text{Eu}(\alpha,n)^{154}\text{Tb}$ by activation, in order to provide data for γ -process and statistical model calculations [102]. As it turned out the half-life of one reaction product, the first isomeric state of ^{154}Tb was only known with high uncertainties ($t_{1/2} = 9.4\text{ h} \pm 0.4\text{ h}$). This was due to the ambiguous values in the literature (see Table 5.5). To decrease the uncertainty of the cross section experiment we decided to carry out our own measurement on the half-life of ^{154m}Tb .

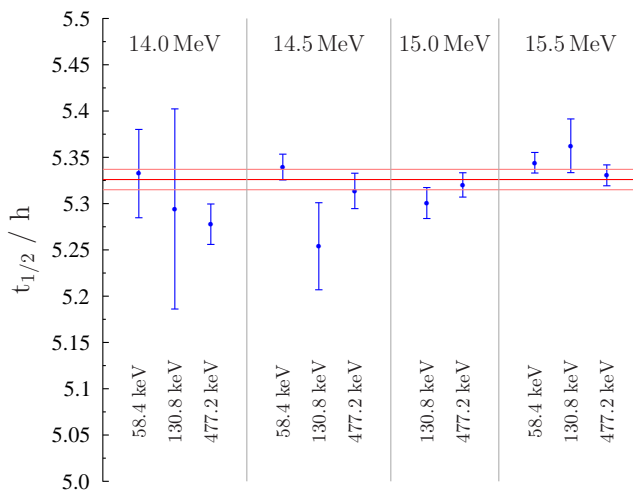


Figure 5.11: The results of the ^{133m}Ce measurement. The recommended value and its error are shown as horizontal lines. All the error bars contain the factor $\sqrt{\chi^2_{\text{red}}}$.

Target preparation. ^{154m}Tb was made by the $^{151}\text{Eu}(\alpha, n)^{154}\text{Tb}$ reaction. Europium oxide (Eu_2O_3) enriched to $99.2\% \pm 0.1\%$ in ^{151}Eu (its natural abundance is 47.8%) was evaporated onto Al foils. The use of enriched ^{151}Eu target was necessary to decrease the intensity of the strong γ radiation of ^{156}Tb , coming from the $^{153}\text{Eu}(\alpha, n)^{156}\text{Tb}$ reaction. A thin ($\approx 10\mu\text{g}/\text{cm}^2$) Al protective layer was evaporated onto each target to prevent the produced ^{154}Tb nuclei to diffuse out from the source during the half-life measurement.

Irradiation. The targets were irradiated at the cyclotron laboratory of Atomki. Five targets were irradiated by 13.5 MeV, 14.5 MeV, 15 MeV, 15.5 MeV and 17 MeV energy α beams with a typical beam intensity of $2\mu\text{A}$. The irradiation times varied between 5 h and 12 h. The products of the $^{151}\text{Eu}(\alpha, n)$ reactions and their decay modes can be seen in Fig. 5.12.

Detection. The γ rays were detected with the same 40 % relative efficiency HPGe detector that we used for the room temperature ^{74}As intensity ratio measurements, and the applied shielding was also the same (see Section 3.6). We used Ortec electronics and Ortec MAESTRO spectroscopic

Table 5.5: The results of the measurements of the half-life of ^{154m}Tb in the literature.

Year	Ref.	$t_{1/2}/\text{h}$
1972	[123]	9.9 ± 0.1
1973	[124]	9.0 ± 0.5
1975	[125]	9.0 ± 1.0
1976	[126]	9.9 ± 0.4
1983	[127]	9.8 ± 0.3
1998	compilation [128]	9.4 ± 0.4

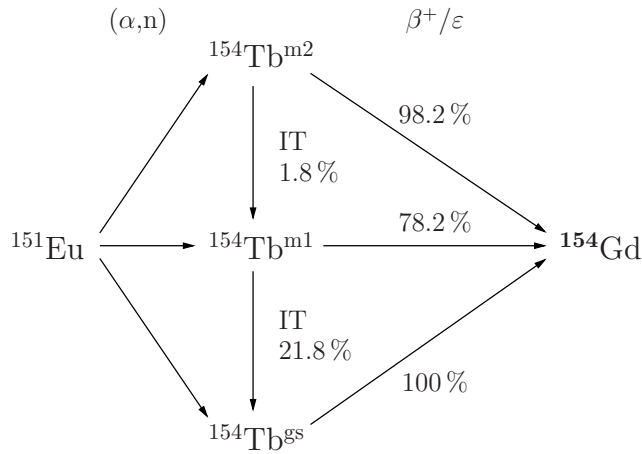


Figure 5.12: The isotopes created by the $^{151}\text{Eu} + \alpha$ reactions. $t_{1/2}(^{154\text{gs}}\text{Tb}) = 21.5 \text{ h}$, $t_{1/2}(^{154\text{m1}}\text{Tb}) = 9.4 \text{ h}$, $t_{1/2}(^{154\text{m2}}\text{Tb}) = 22.7 \text{ h}$.

software, just as in the case of the ^{133m}Ce experiment. The built-in dead time correction of the data acquisition system was checked with a pulse generator. The spectrum acquisition time varied between 21 h and 62 h. Unlike the ^{133m}Ce , for the analysis only one γ line ($E_\gamma = 540.2 \text{ keV}$) was used, as the other lines were so weak that they could not improve the precision of the measurement.

The half-life was determined by fitting an exponential decay curve on the points of the dead-time corrected 540 keV peak area versus time. In the case of the ^{133m}Ce measurement we could analyse three peaks with different background conditions, which made our results robust. In this experiment we only had one peak, which necessitated the use of a more sophisticated

uncertainty analysis. In the following I describe the steps of the uncertainty calculation in details.

Systematic uncertainties. First of all, the possible shifts in the detection efficiency had to be taken into account. This was done by comparing the results of the measurements on the five samples and taking the difference of the highest and lowest obtained half-life. This conservative estimation gave 0.24 % systematic uncertainty.

Dead-time determination uncertainties can also add to the systematic error. For this, the dead-time determined automatically by the Ortec electronics was compared to the dead-time value manually obtained by introducing a periodic signal pulser to the acquisition system. The pulser signals were counted both on a counter directly connected to the pulser and in the spectrum as the pulser peak area. We found that the dead-time provided by the data acquisition system was precise within about 0.3 %, which translates into less than 0.1 % half-life uncertainty. This value was adopted for the systematic uncertainty due to dead-time determination.

$^{151}\text{Eu}(\alpha, n)$ produces ground state ^{154}Tb and two isomers, ^{154m}Tb and $^{154m^2}\text{Tb}$. The m2 isomer is known to decay by isomeric transition to the m1 state, continuously feeding it. However, the branching ratio of this transition is only $(1.8 \pm 0.6) \%$ [124]. Furthermore, the m2 isomer is only very weakly populated by the $^{151}\text{Eu} + \alpha$ reaction. At $E_\alpha = 15.6 \text{ MeV}$ the cross section ratio of the reactions leading to the m2 and m1 states is $\sigma_{\text{m2}}/\sigma_{\text{m1}} = 0.019 \pm 0.003$ [129]. In our experiment this ratio was found to be in the interval $(0.012, 0.027)$, calculated from the strength of the characteristic γ rays of the two isomers. The combination of the low cross section ratio and the low isomeric transition ratio results in a maximum of 0.08 % feeding of the m1 state by the m2 state (if one takes a conservative upper limit of 2σ deviation from the isomeric transition literature value). This feeding influences the determined m1 half-life by at most 0.1 %. This value was taken as the systematic uncertainty coming from the m2 feeding.

Based on Ref. [125], it was assumed that the 540 keV line comes only from the m1 decay. Since the analysis of our data shows that the ground state population of the $^{151}\text{Eu} + \alpha$ reaction is not negligible (it is typically $\sigma_{\text{g.s.}}/\sigma_{\text{m1}} \approx 0.3$), our assumption should be confirmed. This was done by χ^2 analysis. A hypothetical ground state decay was assumed and the goodness-

of-fit was checked by the χ^2_{red} reduced chi-square value as a function of the ground state decay contribution to the peak. The test confirmed our assumption as the minimum χ^2_{red} was obtained at zero ground state contribution. The value where the χ^2_{red} increases by one was taken as the uncertainty of our assumption, which causes a 0.27 % half-life uncertainty. Thus, a 0.4 % final systematic half-life uncertainty was given as the quadratic sum of the four components of the systematic uncertainties.

As a check, the half-life of ^{66}Ga was also obtained ($t_{1/2} = 9.49 \text{ h} \pm 0.03 \text{ h}$ [130]). This isotope came from the copper impurity of the backing, through the $^{63}\text{Cu}(\alpha, n)^{66}\text{Ga}$ reaction, and its 1039 keV γ peak was observable in four of the samples. The obtained half-life value ($t_{1/2} = 9.414 \text{ h} \pm 0.071 \text{ h}$) was in agreement with the literature value.

Results. The results of our measurement can be seen in Table 5.6 and Fig. 5.13. Where the χ^2_{red} value of the decay curve fitting has been greater than 1, the uncertainty was multiplied by $\sqrt{\chi^2_{\text{red}}}$.

Table 5.6: The results of the ^{154m}Tb half-life measurement. The literature half-life value is $t_{1/2} = 9.4 \text{ h} \pm 0.4 \text{ h}$. The given uncertainties are statistical only.

Source no.	$t_{1/2}/\text{h}$	χ^2_{red}
1	9.993 ± 0.106	0.88
2	10.008 ± 0.033	0.85
3	9.984 ± 0.019	0.98
4	10.008 ± 0.029	0.90
5	9.994 ± 0.006	1.31
weighted mean	9.994 ± 0.006	

The suggested half-life value is $t_{1/2} = (9.994 \pm 0.039) \text{ h}$, which comes as the weighted mean of the half-lives measured with the different sources. This value already contains the systematic uncertainty added quadratically to the statistical one.

5.5 Conclusions

^{133m}Ce . We measured the half-life of ^{133m}Ce with γ spectrometry and found it to be $t_{1/2} = (5.326 \pm 0.011) \text{ h}$. This value is consistent with the literature value of $t_{1/2} = (4.9 \pm 0.4) \text{ h}$, while its uncertainty is lower by more than

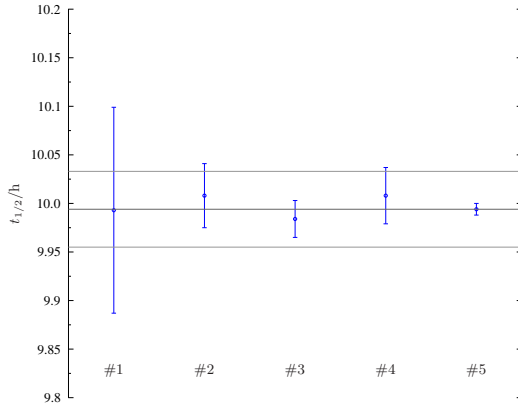


Figure 5.13: Results of the ^{154m}Tb half-life measurement. The horizontal lines indicate the suggested value of $t_{1/2} = (9.994 \pm 0.039)\text{ h}$. The literature value is much lower, $t_{1/2} = (9.4 \pm 0.4)\text{ h}$.

a factor of 30. With this new half-life value we were able to reach our goal to measure the cross section of the $^{130}\text{Ba}(\alpha, n)^{133m}\text{Ce}$ reaction with the activation technique.

^{154m}Tb . The half-life of ^{154m}Tb was found to be $t_{1/2} = 9.994\text{ h} \pm 0.039\text{ h}$. This value is one order of magnitude more precise than the literature value, but it is also much larger than that ($t_{1/2}^{\text{lit}} = 9.4\text{ h} \pm 0.4\text{ h}$). We suggest the use of our value in the future since it is in agreement with the most precise measurements so far [123, 126, 127], compatible with Ref. [125] and in disagreement with Ref. [124]. On these grounds, the quandary of the compilation can be solved by rejecting the results of the two latter papers. With the newly obtained value we could successfully reduce the uncertainty of the reaction cross section measurement of the $^{151}\text{Eu}(\alpha, n)^{154}\text{Tb}$ reaction [99, 102].

Participation of the author. I took significant part in the measurement of the half-life of ^{133m}Ce . I participated in the assembly of both the beamline and the detection setup and also in the irradiation and the detection processes. I arranged the automatic data analysis most importantly by writing the fityk scripts and fityk script writer programs. I was responsible for the complete evaluation process and the publication of the results.

I had a minor role in the ^{154m}Tb half-life experiment. I took part in the irradiation procedure and in the analysis of the data. Some of my programs were used for the data analysis.

Publications.

Scientific papers

Gy. Gyürky, G. Rastrepina, Z. Elekes, **J. Farkas**, Zs. Fülöp, G. G. Kiss, E. Somorjai, T. Szűcs, *Precise half-life measurement of the 10 h isomer in ^{154}Tb* , Nucl. Phys. A **828**, 1 (2009)

J. Farkas, Gy. Gyürky, Z. Halász, T. Szűcs, Zs. Fülöp, E. Somorjai, *Half-life measurement of ^{133m}Ce with γ spectrometry*, Eur. Phys. J. A **47**, 7 (2011)

Conference poster

J. Farkas, Gy. Gyürky, Z. Halász, T. Szűcs, Zs. Fülöp, E. Somorjai, *Half-life determination of ^{133m}Ce for activation cross section measurements*. 11th International Symposium on Nuclei in the Cosmos, NIC XI. Heidelberg, Germany, 19–23 July, 2010

Chapter 6

The Newcomb – Benford law as a test of decay models

In this chapter I discuss the relation between the Newcomb – Benford law and nuclear decay models. I begin with a brief historical overview of the law in Section 6.1. Then in Section 6.2 I review the literature relating the law to nuclear decay lifetimes. Section 6.3 recalls a recently published mathematical explanation of the law, which is based on Fourier analysis. In Section 6.4 I answer the question ‘Is the law applicable to test nuclear decay models?’

6.1 A historical review of the Newcomb – Benford law

The history of the Newcomb – Benford law (NBL) goes back to the nineteenth century, when the Canadian-American mathematician and astronomer Simon Newcomb noticed a rather strange phenomenon: the earlier pages of the logarithmic tables are much more used than the last pages [132]. Inspired by this rather peculiar observation he examined the histogram of the first significant digits of some data sequences. In most cases he found the same strange pattern: the probability P_d of a number having d as its first significant digit is (note that $\sum P_d = 1$):

$$P_d = \lg(1 + 1/d) \quad (d = 1, 2, \dots, 9). \quad (6.1)$$

This was reinvented later by a physicist of General Electric, Frank Benford, who investigated an enormous quantity of data from various sources [133]. Today the law is mostly known as Benford’s first digit law.

Let us note that the NBL is more general and covers the other digits, too [132]. In spite of this, only the first digit law can be investigated when analysing nuclear decay half-lives. The main reason for this is that in many cases the second digits are uncertain due to low experimental precision. Furthermore, the chart of half-lives contains only a few thousand values, which is insufficient to provide reliable statistics on the distribution of other digits.

The NBL is base invariant, which means that if the numbers in the original sequence obeying the law are transformed to a logarithmic base of k , and the first significant digits are extracted in this new base, then the law still holds (obviously k cannot be arbitrarily large):

$$P_d = \log_k(1 + 1/d) \quad (d = 1, \dots, k - 1). \quad (6.2)$$

Additionally, if one multiplies the elements of a sequence obeying the NBL with a given constant, the new sequence will again follow the law. This means that the NBL is scale invariant.

Regardless of whether the primary data sequences come from wealth statistics, magazines, geographical data or physics books, there is a very good chance that they obey the law. The validity of the NBL for different kinds of number sequences is a long standing issue in mathematics and the natural sciences. In physics, there are several such sequences that fulfill the law quite well, like physical constants [134], seismic activity data [135] or the intensities of atomic spectral lines [136]. The half-lives of α radioactive nuclei were also examined [137], and most recently this investigation was extended to β decay and spontaneous fission, including both the ground and isomeric states [138, 139]. In the following we examine the recent statements and conclusions regarding the relation between the NBL and nuclear decay [137, 138, 139].

6.2 The Newcomb–Benford law and nuclear half-lives

6.2.1 The distribution of the first digits

The authors of Refs. [137, 138, 139] examined the relative occurrence of the first significant decimal digits of nuclear half-life values. The data were

Table 6.1: The occurrence of the first significant digit of half-lives is in good agreement with the Newcomb–Benford law.

Digit	Occurrence	Expected by the NBL
1	701	692 ± 22
2	405	405 ± 18
3	281	287 ± 16
4	210	223 ± 14
5	209	182 ± 13
6	149	154 ± 12
7	112	133 ± 11
8	119	118 ± 11
9	112	105 ± 10

found to satisfy the NBL. In [137], 477 α decaying nuclei were taken into account, while in [139], 2059 β decay half-lives were investigated. Ref. [138] examined up to 3553 half-lives of nuclei with various decay modes. According to this work, the situation does not change if one adds a few hundreds or a thousand of estimated half-life values to the number sequence [138, 139].

The result of our own analysis is shown in Table 6.1 and in Fig. 6.1. The input data sequence were taken from NUBASE2003 [140]. The nuclei for which we know only the upper or lower limit of their half-lives were rejected, which resulted in an input sequence of 2298 entries. The occurrence of the first digits followed the NBL well within two standard deviations.

The calculation of the uncertainty of the NBL is based on the binomial distribution [137]. Let N be the size of the data set (in our case $N = 2298$) and P_d the probability of a value having d as its first significant digit. One is expected to find $N_d = NP_d$ values having d as its first significant digit with an error of Δ_{N_d} , where

$$\Delta_{N_d} = \sqrt{NP_d(1 - P_d)} \quad (6.3)$$

according to the standard deviation of the binomial distribution.

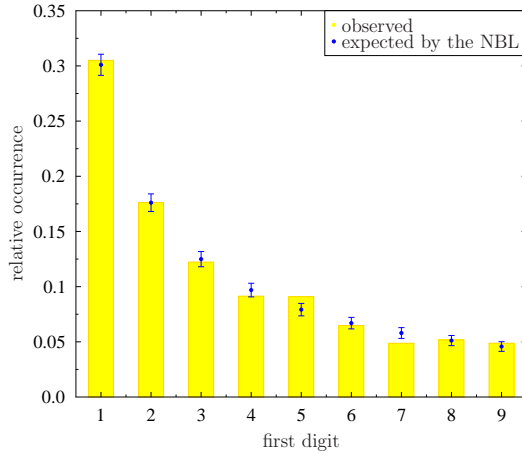


Figure 6.1: The distribution of the first significant digits of half-lives follows the Newcomb–Benford law. 2298 half-life values from NUBASE2003 [140] were evaluated.

6.2.2 Ones scaling test

The ‘ones scaling test’ (OST) is a simple method to test quantitatively whether a dataset satisfies the NBL [141]. The law holds only if the relative occurrence of the numbers beginning with the digit 1 is around $P_1 = 30.1\%$, even after an arbitrary number of multiplications by a given constant (due to scaling invariance). The constant is called the scaling constant, which we set to 1.01. Figure 6.2 shows the result of the OST for our dataset of 2298 half-lives. The NBL is clearly followed within the expected uncertainty.

6.3 Mathematical explanation

In this section we summarize the conditions for the NBL to hold, based on the work of Smith [141]. The following reasoning can be used whenever one knows the probability density function (p. d. f.) of the input set of numbers.

A dataset obeys the NBL if and only if the ones scaling test gives $\lg 2 \approx 0.301$ after any number of multiplications by the scaling constant. Let $f(x)$ denote the p. d. f. of the numbers. In logarithmic scale ($g(x) = \lg x$) the p. d. f. becomes $f(g)$. The condition that a number has 1 as its first significant digit can be expressed by the sampling function $s(g)$, which is a periodic

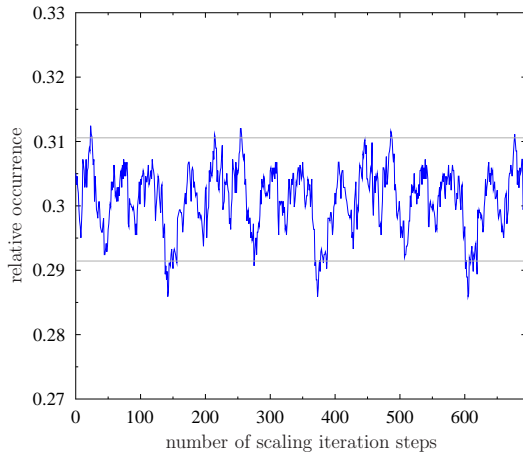


Figure 6.2: The result of the ones scaling test executed on our dataset. The relative number of ones as the first significant digit fluctuated around its expected value 0.301 within the uncertainty 0.0096. The scaling constant was 1.01. The error is given by Eq. 6.3, and is indicated by the horizontal lines. Note the periodicity coming from $1.01^{231} \approx 10$ (see text).

square function on the logarithmic scale (see the blue stripes in Fig. 6.3). The P_1 probability of having 1 as the first significant digit is

$$P_1 = \int_{-\infty}^{\infty} s(g)f(g)dg. \quad (6.4)$$

Multiplication by c^m (where $c > 1$ is the scaling constant) works as a shift by $\gamma = m \lg c$ on the logarithmic scale. The area denoted by P_1 in Eq. 6.4 remains unchanged if we gain and lose the same area when we perform the scaling (Fig. 6.3) [142]. Due to the shape of the sampling function, a scaling by 10^i ($i \in \mathbb{Z}$) results in the same P_1 , making the results of the OST necessarily periodic when $c \approx 1$ (as in Fig. 6.2). According to Newcomb [132],

$$\forall C \in \mathbb{R}, C > 0 : \exists i \in \mathbb{Z}, r \in [0, 1] : C = 10^{i+r}. \quad (6.5)$$

Only r plays a role in the value of the first significant digit, since i only represents the shifting of the decimal point. Newcomb stated that the NBL is naturally followed, because the distribution of r is uniform. Though the

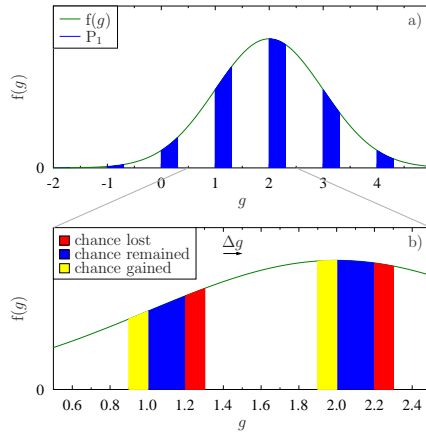


Figure 6.3: Illustration of the sampling of the ones scaling test: *a)* a sample distribution (log-normal with a mean of 2 and standard deviation 1 on the lg axis), *b)* the result of the multiplication of the number sequence by $10^{\Delta g}$.

uniformity of r is not at all trivial, by using the train of thought above we can see, that his statement can be written in a more precise form: the NBL is followed if the distribution of the numbers are log-uniform ranging between integer powers of 10.

To get all functions approximately obeying the law in a mathematically rigorous way, the result of the ones scaling test after m scaling iterations has to be expressed as a convolution

$$P_1(\gamma) = \int_{-\infty}^{\infty} s(g)f(g-\gamma)dg \Rightarrow P_1(g) = s(g) * f(-g). \quad (6.6)$$

The convolution transforms into a simple multiplication $F(f) \cdot S(f)$ in the frequency domain, where F and S are the Fourier transforms of f and s , respectively. Since the support of $S(f)$ is the nonnegative integer numbers, and the ones scaling test gives 0.301 only if the $F(f) \cdot S(f)$ product is 0.301 at $f = 0$ and vanishes everywhere else, the following theorem holds: A set of numbers with the probability distribution $f(g)$ obeys the NBL if and only if the Fourier transform $F(f)$ of the probability distribution function of the numbers vanishes at all nonzero integer frequencies (Benford's law compliance theorem, [141]). For an experimentally good satisfaction of the law, it is enough for the product to become small at integer frequencies. In natural

sciences this criterion is most likely to be fulfilled by such $f(g)$ distributions the $F(f)$ Fourier transform of which becomes very small ($F(f) \approx 0$) before $f = 1$, and remains close to zero thereafter.

6.4 Is the law applicable to test nuclear decay models?

The specific distribution of the first digits comes from the method one uses when decides whether a number has d as its first digit. This method is mathematically defined by the sampling function. It follows, that for any given distribution of numbers, the compliance of the NBL (within a given error) can be predicted, but not vice versa: from the compliance of the law the distribution cannot be constructed.

Consequently (and contrary to the findings of [138, 139]), the feeling that there is a natural phenomenon behind the NBL is illusoric. While scale invariant systems play an important role in today's research, in the case of the NBL the source of the scale invariance is the (logarithmic) periodicity of the sampling function (given the probability distribution fulfills the mentioned criterion).

If one knows the distribution of a number set, the NBL carries no additional information. Thus, it is only the distribution that should be explained or predicted by the theory of a given phenomenon obeying the law, and not the satisfaction of the law itself. Contrary to the suggestion of e.g. [136, 138, 139], knowing the p. d. f., the use of the NBL to test a number sequence derived from a theory modeling a phenomenon that obeys the law gives no additional information on the physics of the system (just as knowing the integral of a function on an interval does not help much in finding a function with a given shape).

In the case of nuclear decay, the distribution of the half-lives is known (see Fig. 6.4). The examined experimental values of the half-lives span 54 decimal orders of magnitude. It can be seen that this distribution is very close to a log-normal distribution. The parameters of the fitted normal distributions can be read in Table 6.2.

By looking at the distribution it is not surprising that half-lives follow the NBL. The Fourier transform of a Gaussian (see Fig. 6.5) with stan-

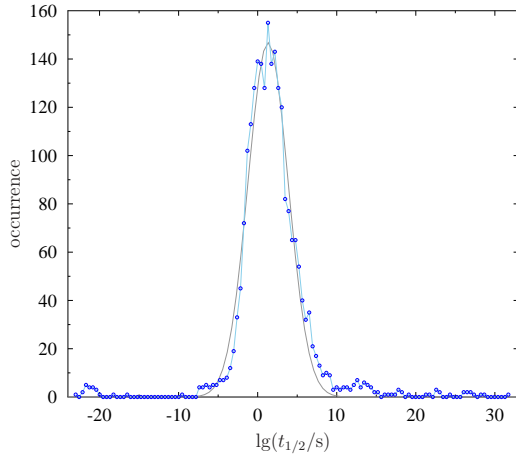


Figure 6.4: Distribution of the half-lives of the examined 2298 decays. The known half-life values cover about 54 orders of magnitude. The binning of the histogram is natural logarithm based.

dard deviation σ is yet another Gaussian with a mean of 0 and a standard deviation of $1/(2\pi\sigma)$. The standard deviation of the fitted Gaussian is $3.0139/\sqrt{2 \ln 2} \approx 2.56$ on the decimal logarithmic scale, making the standard deviation of its Fourier transform ≈ 0.062 . Thus, the transform becomes very small at all integer frequencies, resulting only minor fluctuations in the value of $P_1(\gamma)$.

If a theory of nuclear decay reproduces the half-life distribution well, it automatically satisfies the NBL. Thus, the physics is behind the form of the distribution, and the models have nothing to do with the NBL itself.

Participation of the author. I wrote programs to perform the NBL’s compliance to half-lives and ran them on a half-life database. I performed the Fourier transformation and drew consequences based on the literature of the NBL, the half-life probability distribution function and its Fourier transform. I was also responsible for the publication of the results.

Publication.

Scientific paper

J. Farkas, Gy. Gyürky, *The significance of using the Newcomb–Benford law as a test of nuclear half-life calculations*, Acta Phys. Pol. B **41**:6 (2010)

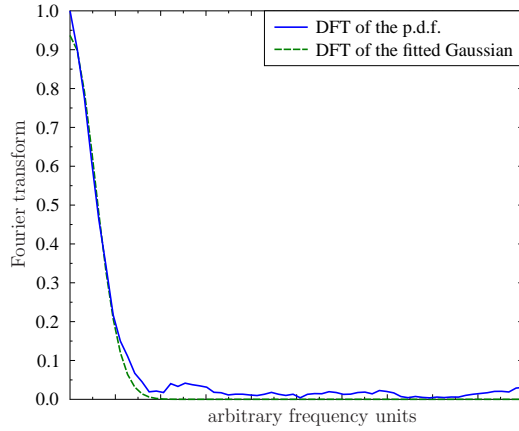


Figure 6.5: Fourier transform of the half-life distribution and the fitted log-normal function.

Table 6.2: The parameters of the Gaussians fitted to the logarithmic distribution of the half-lives of 2298 decays. The parameters differed slightly depending on the resolution of the binning. Decimal, natural and binary logarithm based binning were used. HWHM: Half Width at Half Maximum.

binning	mean	$\text{base}^{\text{mean}}$	HWHM	$\text{base}^{\text{HWHM}}$
lg	1.0503 ± 0.0051	11.23	3.0139 ± 0.0060	1032.52
ln	3.030 ± 0.018	20.70	6.889 ± 0.021	981.42
lb	4.609 ± 0.030	24.40	9.909 ± 0.036	961.40

Chapter 7

Summary

In this chapter I summarize the motivation and results of the research covered in my thesis. Section 7.1 is the summary in English, while Section 7.2 is the Hungarian one.

7.1 Summary

γ intensity ratio measurements of embedded ^{74}As

Nuclear astrophysics aims at explaining the synthesis of elements and energy generation of stars. As we cannot experiment with stars, observations are compared to the results of computer simulations. These simulations rely heavily on nuclear physics input. This input comes either directly from nuclear measurements or from theoretical calculations, where the theories are constrained by the results of nuclear experiments.

Low energy nuclear reaction cross section measurements showed that the electronic environment of the target isotope affects the measured cross sections below a center of mass energy of $\sim 10\text{ keV}$. The effect was pronounced when the targets were embedded into metals. The phenomenon has been attributed to the electromagnetic screening of metallic electrons, and it has been described by the classical Debye–Hückel plasma model. Later the model was extended to nuclear decay: it was suggested that α and β^+ decays are enhanced while β^- decay is suppressed when the radionuclides decay in a metallic environment (for electron capture decay no clear conclusion was drawn). If half-lives can really be modified by the electronic environment, this effect shall be taken into account in astrophysical

calculations. It could also be of use in nuclear technology either to hasten the decay of nuclear waste or to decrease its activity by slowing down its decay.

Several experiments were performed recently to verify the predictions of the Debye–Hückel model. The results of these measurements were contradictory: some could show evidence of altered half-lives, while others saw no signs of half-life modification. Our group set out to conduct two decisive high precision measurements to either confirm or disprove the applicability of the Debye–Hückel model to nuclear decay.

We used ^{74}As in our experiments as it undergoes both β^- and β^+/ε decays. By utilizing γ ray spectrometry we could differentiate between these decay modes, as the different types of decay were followed by the emission of γ rays with different characteristic energies. As the model predicts a change in the half-lives in opposite directions for these decay modes, high precision could be achieved by monitoring the β^+/ε activity ($E_\gamma = 596 \text{ keV}$) relative to the β^- activity ($E_\gamma = 635 \text{ keV}$).

In our first experiment we produced ^{74}As at the cyclotron of Atomki by the $^{74}\text{Ge}(\text{p},\text{n})^{74}\text{As}$ reaction and embedded it into metals (tantalum and aluminum), semiconductor (germanium) and insulator (mylar foil) host materials. We used a high purity germanium detector to follow the decay of the samples. The measured relative γ intensities were compatible with each other and with the literature value, no matter what the host of the arsenic was. Our measurement supports that the half-lives of the three decay modes of ^{74}As was unaffected by the electronic environment within 3 % precision. This measurement strengthened the view that the Debye–Hückel model is not adequate to describe enhanced nuclear decay of embedded radionuclides, as it predicted an at least 4 % enhancement for the β^+ decay and an at least 12 % suppression for the β^- decay.

γ intensity ratio of embedded ^{74}As at low temperatures

A key concept in the Debye–Hückel decay screening theory is the screening energy U_e . As $U_e \sim T^{-1/2}$, Debye screening predicts a spectacular enhancement of electron screening at very low temperatures. This was studied in many experiments, in which the samples consisting of radionuclides embedded in metals were cooled down to temperatures of usually 10 K – 20 K. In

an outstanding experiment researchers could investigate the decay of the α emitter ^{253}Es in iron at 50 mK temperature.

The outcome of the experiments of the literature was again ambiguous: some observed a change in the half-lives but some did not. Our group joined the debate by extending our relative intensity ratio measurement technique to low temperatures.

The production of the radioactive samples was similar to that described above. This time we used only tantalum and germanium as host materials, as mylar can be damaged at low temperatures. The samples were cooled at the Cryophysics Laboratory of Atomki with a $^3\text{He}/^4\text{He}$ dilution refrigerator. The activity of the samples was followed again by a HPGe γ detector, while the samples were cooled to 77 K, 4.2 K, \approx 1 K and \approx 250 mK.

Within our precision (which was similar to the precision of our room temperature measurement) we could not observe any change in the half-lives of ^{74}As at any temperature with any host material, though – according to the Debye–Hückel model – the half-lives should have changed by orders of magnitude at subkelvin temperatures. As the dependence of the screening on temperature is a crucial part of the Debye–Hückel model, based on our results we could clearly refute the claims that the Debye–Hückel model gives a suitable description of electron screening of nuclear decay.

High precision half-life measurements of ^{133m}Ce and ^{154m}Tb

In order to support the theoretical work on the astrophysical γ process, we measured the cross section of α induced reactions on ^{130}Ba , as experimental data on these reactions were absent in the literature. The (α, γ) reaction cross section can directly be used to enhance γ process models, while the (α, n) reaction is used to constrain the Hauser–Feshbach model calculations used in such models.

We used the activation technique in our measurement: we activated the ^{130}Ba target with an α beam and detected the γ photons emitted by the decaying reaction products. In order to perform the cross section measurement one needs the precise half-lives of the created nuclei. We realized that the half-life of one of the products of the $^{130}\text{Ba} + \alpha$ reaction, ^{133m}Ce is known with high uncertainty ($t_{1/2}^{\text{lit}} = 4.9 \text{ h} \pm 0.4 \text{ h}$). We also found evidence that this half-life value is underestimated. As the compilations were based

on a single measurement published back in 1967, we decided to perform a half-life measurement of ^{133m}Ce the precision of which is suitable for our needs.

The irradiations were performed at the cyclotron of Atomki and the decay of ^{133m}Ce was followed with a HPGe γ detector. By analysing the 58.4 keV, 130.8 keV and 477.2 keV peaks we found the half-life to be $t_{1/2} = 5.326 \text{ h} \pm 0.011 \text{ h}$. As this value is consistent with the literature value and its uncertainty is lower by almost a factor of 40, we suggested its use in the nuclear data compilations to-come. This new half-life value was successfully used in the cross section measurement of the $^{130}\text{Ba}(\alpha, n)^{133m}\text{Ce}$ reaction.

We also measured the half-life of ^{154m}Tb . In this case the motivation was to measure the cross section of the $^{151}\text{Eu}(\alpha, n)^{154m}\text{Tb}$ reaction. We used a similar technique as in the cerium measurement. The half-life was found to be $t_{1/2} = 9.994 \text{ h} \pm 0.039 \text{ h}$, which is an order of magnitude more precise than the literature value of $t_{1/2}^{\text{lit}} = 9.4 \text{ h} \pm 0.4 \text{ h}$.

The applicability of the Newcomb – Benford law in testing nuclear decay models

The Newcomb – Benford law (NBL) gives the distribution of the first significant digits of numbers coming from various data sources. It was found to describe well the distribution of the first significant digits of nuclear decay half-lives. Based on this and the scale invariant nature of the law it was recently suggested that the compliance of the law is an evidence of the self-organizing nature of the atomic nucleus. The law was also proposed as a tool to test nuclear decay models: if the first digits of calculated half-lives do not obey the NBL, then the given nuclear model cannot be complete.

Many mathematicians tried to solve the conundrum of the NBL for decades. Though only partial success has been achieved it became clear that the problem can be approached from a mathematical point of view and mystical explanations shall be rejected. A new, Fourier analysis based theorem was published in 2008. This gives the conditions when the NBL is satisfied for number sequences having a given probability density function.

In my work I have confirmed that the NBL can be applied for half-lives with two technique: direct check and the method called ‘ones scaling test’. Then I examined both the probability distribution function of the

half-lives and its Fourier transform. I found that the distribution function automatically satisfies the law. This means two things. On the one hand the idea that the NBL indicates self-organizing behavior can no longer be held. On the other hand if a nuclear decay model provides the same half-life distribution as nature, then it automatically satisfies the NBL, while the satisfaction of the NBL does not mean at all that the predicted half-life distribution is correct. This way the NBL cannot be used to test nuclear decay models.

7.2 Összefoglalás

Beágyazott ^{74}As γ intenzitásarányának mérése

A nukleáris asztrofizika célja, hogy megmagyarázza a kémiai elemek keletkezését és a csillagok energiatermelését. Mivel a csillagokkal nem tudunk kísérletezni, így a megfigyeléseinket számítógépes szimulációk eredményeivel hasonlítjuk össze. A szimulációk eredményei erősen függnek a magfizikai bemenő paramétereiktől, amelyek vagy közvetlenül magfizikai mérésekkel vagy kísérletileg ellenőrizhető elméleti számításokból származnak.

Alacsony energiás magreakció hatáskeresztmetszet-mérésekkel tudjuk, hogy a $\sim 10 \text{ keV}$ középponti energia tartományban a céltárgy atommagjai körül elhelyezkedő elektronok befolyásolják a hatáskeresztmetszetet. Ez a hatás fémbe helyezett céltárgyak esetén különösen meghatározó. A jelenséget a fémek delokalizált elektronainak elektrosztatikus árnyékolásával magyarázták és a klasszikus plazmafizika Debye–Hückel-féle modelljével írták le. Később a modellt kiterjesztették a radioaktív bomlásra is: felvették, hogy a fémekbe ágyazott α és β^+ bomló izotópok felezési ideje csökken, míg a β^- bomló magok felezési ideje nő (az elektronbefogásos bomlás élettartamának változására nem született egyértelmű jóslat). Ha a felezési időket valóban befolyásolják a bomló magok körüli elektronok, akkor ezt figyelembe kell venni az asztrofizikai számításoknál. Ráadásul a jelenség rendkívül hasznos volna a nukleáris ipar számára, például a nukleáris hulladékot fémbe ágyazva azok felezési ideje (és így a veszélyességük ideje) csökkenthető volna, vagy a felezési idejük növelésével csökkenthető volna az aktivitásuk.

A Debye–Hückel-modell ellenőrzésére számos kísérletet hajtottak végre

a közelmúltban. A kísérletek eredményei azonban ellentmondásosak voltak: néhány kísérletben képesek voltak kimutatni a felezési idők megváltozását, míg más kísérletekben ennek jelét sem látták. A kutatásokhoz a csoportunk is csatlakozott. Célunk az volt, hogy két nagypontosságú kísérletsorozatot végrehajtva egyértelműen megerősítsük vagy elvessük a Debye–Hückel-modell beágyazott bomlásra való alkalmazhatóságát.

Kísérleteinkhez a β^- és β^+/ε bomlásmódokkal is átalakuló ^{74}As izotópot használtuk. Mivel a különböző típusú bomlásokat különböző energiájú γ -sugárzás kibocsátása kíséri, ezért azok γ -spektrometriával elkövülnéhetők egymástól. Mivel a modell a két bomlásmódra eltérő irányú felezési idő változást jósol, így nagy pontosságot érhetünk el azzal, ha a β^+/ε bomlást követő $E_\gamma = 596 \text{ keV}$ energiájú γ -vonal és a β^- bomlást követő $E_\gamma = 635 \text{ keV}$ energiájú vonal erősségeinek arányát mérjük.

Az ^{74}As izotópot a $^{74}\text{Ge}(\text{p},\text{n})^{74}\text{As}$ reakció segítségével állítottuk elő az Atomki ciklotronjával. Első kísérletünkben az arzént fémekbe (tantál és alumínium), félvezetőbe (germánium) és szigetelőbe (milár fólia) ágyazva vizsgáltuk. A minták bomlását nagytisztaságú germánium (HPGe) detektorral figyeltük. A mért relatív γ -intenzitások egymással és az irodalmi értékkel is összhangban voltak, attól függetlenül, hogy az arzént milyen anyag vette körül. A Debye–Hückel-modell a β^+ felezési idő legalább 4%-os növekedését és a β^- felezési idő legalább 12%-os csökkenését jósolta, míg a mérés alapján a felezési idők legfeljebb 3%-kal változhattak meg. Eredményeink szerint tehát a Debye–Hückel-modell az irodalomban ismertetett módon nem alkalmazható beágyazott felezési idők változásának számítására.

Beágyazott ^{74}As γ intenzitásarányának mérése alacsony hőmérsékleteken

A Debye–Hückel-féle bomlásárnyékolási modell egyik kulcsfogalma az U_e árnyékolási energia. Mivel $U_e \sim T^{-1/2}$, ezért a modell a felezési idők látványos változását jósolja alacsony hőmérsékleten. Ezt a jelenséget több olyan kísérletben is vizsgálták, ahol a fémes környezetbe ágyazott radioaktív izotópokat alacsony, általában 10 K–20 K hőmérsékletre hűtötték. A legalacsonyabb hőmérsékletű kísérletben vasba ágyazott α -bomló ^{253}Es -ot hűtötték le 50 mK hőmérsékletre.

Akárcsak a szobahőmérsékletű mérések esetén, a kísérleti eredmények itt sem voltak egyértelműek: volt amikor sikerült kimutatni felezési idő változást, volt amikor nem. Csoportunk a fent ismertetett relatív kísérleti technika segítségével igyekezett eldönteni a kérdést.

A radioaktív mintákat az előzőekben leírtakhoz hasonlóan állítottuk elő, de a keletkezett arzént most csak tantál és germánium mintákba ágyaztuk be, mivel a milár alacsony hőmérsékleten könnyen sérül. A mintákat egy $^3\text{He}/^4\text{He}$ keverési hűtőgéppel hűtöttük le az Atomki Hidegfizikai Laboratóriumában. A minták bomlását ismét egy HPGe γ -detektorral követtük, miközben 77 K, 4.2 K, ≈ 1 K és ≈ 250 mK hőmérsékletre hűtöttük őket.

A Debye–Hückel-modell a felezési idők több nagyságrenddel való változását jósolja 1 K alatti hőmérsékleteken. Ennek ellenére a méréseink most sem mutattak ki változást a különböző bomlásmódokhoz tartozó γ -intenzitások arányában. Mivel a hőmérsékletfüggés a Debye–Hückel-modell szerves részét képezi, ezért a kísérletünkön egyértelműen arra lehet következtetni, hogy a modell alkalmatlan a beágyazott radioizotópok felezési idő (nem) változásának helyes kiszámítására.

A $^{133\text{m}}\text{Ce}$ és a $^{154\text{m}}\text{Tb}$ izotópok felezési idejének nagypontosságú mérése

Az asztronómiai γ -folyamat elméleti kutatásának előmozdításához szükséges a benne szereplő magreakciók kísérleti vizsgálata. Csoportunk a ^{130}Ba -on lezajló α -indukált reakciók hatáskeresztmetszetének meghatározását tűzte ki célul. Az (α, γ) reakció hatáskeresztmetszete közvetlenül paraméterezheti a γ -folyamatot szimuláló programokat, míg az (α, n) reakció hatáskeresztmetszetének ismerete segíthet a Hauser–Feshbach-modellel végzett számítások ellenőrzésében és fejlesztésében.

Méréseinkben az aktivációs technikát használtuk: a ^{130}Ba izotópot α -részecskékkel bombáztuk, majd a keletkezett reakciótermékek aktivitását γ -detektorral mértük. A hatáskeresztmetszet méréséhez tudnunk kell, hogy az aktiváció végén mennyi reakcióterméket sikerült előállítani. Ehhez a reakciótermékek felezési idejének pontos ismerete szükséges. A kísérlet kiértékelésekor észrevettük, hogy a $^{130}\text{Ba} + \alpha$ reakciók egyik végtermékének, a $^{133\text{m}}\text{Ce}$ -nak a felezési ideje nagy relatív hibával szerepel az irodalomban ($t_{1/2}^{\text{ir}} = 4.9 \text{ h} \pm 0.4 \text{ h}$). Ráadásul bizonyítékot találtunk arra, hogy az iro-

dalmi érték egyértelműen kisebb, mint a valós érték. Mivel az irodalmi érték egyetlen egy mérésen alapul, amit még 1967-ben végeztek el, úgy döntöttünk, hogy egy új mérés elvégzésével pontosítjuk a ^{133m}Ce felezési idejét.

A besugárzást az Atomki ciklotronjával végeztük, és a ^{133m}Ce bomlását HPGe γ -detektorral követtük. Az 58.4 keV, 130.8 keV és 477.2 keV energiájú csúcsok elemzésével azt találtuk, hogy az izotóp felezési ideje $t_{1/2} = 5.326 \text{ h} \pm 0.011 \text{ h}$. Mivel ez az érték összhangban van az irodalmi értékkel, de annál majdnem 40-szer pontosabb, ezért az új érték felvételét javasoltuk a magfizikai adatbázisokba. Az új érték használata a $^{130}\text{Ba}(\alpha, n)^{133m}\text{Ce}$ hatáskeresztmetszet-mérésénél felmerült problémáinkat is megoldotta.

A ^{154m}Tb felezési idejét is sikerült az irodalminál pontosabban meghatároznunk. Ebben az esetben az volt a célunk, hogy megfelelő felezési idő értéket tudunk használni a $^{151}\text{Eu}(\alpha, n)^{154m}\text{Tb}$ reakció hatáskeresztmetszetének aktivációs méréséhez. A felezési idő meghatározásához használt technika hasonló volt a cérium kísérletnél bemutatotttól. A felezési idő új értéke $t_{1/2} = 9.994 \text{ h} \pm 0.039 \text{ h}$ lett, ami egy nagyságrenddel pontosabb, mint az irodalmi érték ($t_{1/2}^{\text{ir}} = 9.4 \text{ h} \pm 0.4 \text{ h}$).

Használható-e a Newcomb – Benford-törvény radioaktív bomlásmodellek tesztelésére?

A Newcomb – Benford-törvény (NBT) a természetben előforduló számok első értékes jegyének eloszlását adja meg, függetlenül attól, hogy a számok természeti állandókból, napilapokból vagy adóbevallásokból származnak. A törvény a nukleáris felezési idők első értékes számjegyének eloszlására is érvényes. Figyelembe véve a törvény skálainvarianciáját, nemrég azt a következtetést vonták le, hogy a törvény teljesülése az atommagok önszerveződésére utal. Egyes szerzők szerint a törvény arra is alkalmas, hogy segítségével teszteljük a magfizikai bomlásmodelleket: ha egy modell alapján számított felezési idők első értékes számjegyeinek eloszlása nem követi a NBT-t, akkor a modell nem lehet teljes.

A NBT talányával az elmúlt évtizedekben sok matematikus foglalkozott. Bár a törvény magyarázatában csak részleges sikereket értek el, azt már ezek alapján is kijelenthetjük, hogy a törvény természetfeletti eredetével manipuláló magyarázatok elvethetők. 2008-ban Fourier-analízis segítségével

sikerült a törvény teljesülési feltételeit új formába önteni. Az új téTEL olyan esetben alkalmazható, mikor a vizsgált számok egy adott valószínűségi sűrűségfüggénnyel írhatók le.

Munkámban megerősítettem, hogy a felezési idők valóban leírhatók a NBT-el. Ehhez két technikát használtam: a közvetlen ellenőrzést és a „skálázott egyesek” próbát. Ezek után megvizsgáltam mind a felezési idők eloszlását, mind a sűrűségfüggvény Fourier-transzformáltját. Azt találtam, hogy a felezési idők eloszlása olyan, hogy az automatikusan teljesíti a NBT-t. Ez két dolgot jelent. Egyszerűen azt, hogy a NBT teljesülése nem utal önszerveződésre, másrészt azt, hogy a törvény nem használható bomlásmodellek tesztelésére. Ugyanis ha egy bomlásmóddell képes a felezési idők sűrűségfüggvényének helyes előállítására, akkor automatikusan megfelel a NBT-nek is, míg attól, hogy teljesíti a törvényt, még nem biztos, hogy megfelelő a vele számított felezési idők eloszlása.

Publications

Scientific papers related to the thesis

Gy. Gyürky, **J. Farkas**, C. Yalçın, G. G. Kiss, Z. Elekes, Zs. Fülöp and E. Somorjai, *Investigation of ^{74}As decay branching ratio dependence on the host material*, *Europhys. Lett.* **83**, 42001 (2008)

J. Farkas, Gy. Gyürky, C. Yalçın, Z. Elekes, G. G. Kiss, Zs. Fülöp, E. Somorjai, K. Vad, J. Hakl and S. Mészáros, *Measurement of embedded ^{74}As decay branching ratio at low temperatures*, *J. Phys. G* **36**, 105101 (2009)

Gy. Gyürky, G. Rastrepina, Z. Elekes, **J. Farkas**, Zs. Fülöp, G. G. Kiss, E. Somorjai, T. Szűcs, *Precise half-life measurement of the 10 h isomer in ^{154}Tb* , *Nucl. Phys. A* **828**, 1 (2009)

J. Farkas, Gy. Gyürky, *The significance of using the Newcomb – Benford law as a test of nuclear half-life calculations*, *Acta Phys. Pol. B* **41**:6 (2010)

J. Farkas, Gy. Gyürky, Z. Halász, T. Szűcs, Zs. Fülöp, E. Somorjai, *Half-life measurement of $^{133\text{m}}\text{Ce}$ with γ -spectrometry*, *Eur. Phys. J. A* **47**, 7 (2011)

Conference proceedings, talk and posters related to the thesis

Gy. Gyürky, **J. Farkas**, C. Yalçın, G. G. Kiss, Z. Elekes, Zs. Fülöp, E. Somorjai, K. Vad, J. Hakl and S. Mészáros, *Study of ^{74}As decay in different host materials and at different temperatures*. Poster. 10th International Symposium on Nuclei in the Cosmos, NIC X. Mackinac Island, Michigan, USA, 27 July – 1 August, 2008

J. Farkas, Gy. Gyürky, C. Yalçın, G. G. Kiss, Z. Elekes, Zs. Fülöp, E. Somorjai, K. Vad, J. Hakl and S. Mészáros, *Study of ^{74}As decay in different host materials and at different temperatures*. Proceedings. PoS NIC X (2009)

J. Farkas, Gy. Gyürky, C. Yalçın, Z. Elekes, G. G. Kiss, Zs. Fülöp, E. Somorjai, K. Vad, J. Hakl and S. Mészáros, *Temperature dependence of β^- and β^+/ε decay branching ratio of embedded ^{74}As* . Talk. European Nuclear Physics Conference, EuNPC. Bochum, Germany, 16–20 March, 2009

J. Farkas, Gy. Gyürky, Z. Halász, T. Szücs, Zs. Fülöp, E. Somorjai, *Half-life determination of ^{133m}Ce for activation cross section measurements*. Poster. 11th International Symposium on Nuclei in the Cosmos, NIC XI. Heidelberg, Germany, 19–23 July, 2010

Popular article related to the thesis

J. Farkas, *Változik-e a radioaktív atommagok felezési ideje?* (Do the half-lives of radioactive nuclei change?) [in Hungarian], Természet Világa **142**(3) 135 (2011)

Other scientific papers in nuclear astrophysics

C. Yalçın, R. T. Güray, N. Özkan, S. Kutlu, Gy. Gyürky, **J. Farkas**, G. Gy. Kiss, Zs. Fülöp, A. Simon, E. Somorjai, T. Rauscher, *Odd p isotope ^{113}In : Measurement of alpha-induced reactions*, Phys. Rev. C **79**, 065801 (2009)

Gy. Gyürky, Z. Elekes, **J. Farkas**, Zs. Fülöp, Z. Halász, G. Gy. Kiss, E. Somorjai, T. Szücs, R. T. Güray, N. Özkan, C. Yalçın, T. Rauscher, *Alpha-induced reaction cross section measurements on ^{151}Eu for the astrophysical gamma-process*, J. Phys. G **37**, 115201 (2010)

G. Gy. Kiss, T. Rauscher, T. Szücs, Zs. Kertész, Zs. Fülöp, Gy. Gyürky, C. Fröhlich, **J. Farkas**, Z. Elekes, E. Somorjai, *Determining reaction cross sections via characteristic X-ray detection: Alpha-induced reactions on ^{169}Tm for the astrophysical gamma-process*, Phys. Lett. B **695**, 5:419 (2011)

Acknowledgements

My thesis summarizes more than three years of my work in the field of nuclear astrophysics. Though the results discussed here fit well into the recent international literature of nuclear decay studies, they were achieved solely by using the research infrastructure of Atomki. For this I am grateful to the community of the Atomki employees, who helped me a lot along the way of my Ph.D. studies.

I am especially indebted to the members of the Nuclear Astrophysics Group. I am glad for the opportunity to be a member of the most cheerful group of Atomki – the group which would be completely different without its founder, Endre Somorjai. I am much obliged to my supervisor, Zsolt Fülöp for he could see the possibilities both in the half-life project and in me. Very special thanks goes to György Gyürky, without the help of whom I would have no chance to finish (or even start) my work. I thank for the tons of help I got from the other members of the group too, namely Zoltán Elekes, Gábor Kiss, Caner Yalçın, Tamás Szűcs and Zoltán Halász.

Some of our experiments could not have been performed without the help of Kálmán Vad, József Hakl and Sándor Mészáros, all members of the Cryophysics Lab of Atomki. I thank Zsolt Fülöp, György Gyürky and Peter Mohr for the thorough reading and correction of the thesis.

So long, and thanks for all the fish!

Bibliography

- [1] A. Vértes (ed.), *Szemelvények a nukleáris tudomány történetéből* [in Hungarian], Akadémiai Kiadó, Budapest, 2009
- [2] D. J. Griffiths, *Introduction to quantum mechanics*, Prentice Hall, Upper Saddle River, 1995
- [3] G. F. Knoll, *Radiation detection and measurement* (3rd ed.), John Wiley & Sons, New York, 2000
- [4] W. Greiner, J. A. Maruhn, *Nuclear models*, Springer-Verlag, Berlin, Heidelberg, 1996
- [5] K. Nagy, *Kvantummechanika* [in Hungarian], Nemzeti Tankönyvkiadó, Budapest, 1978, 2000
- [6] D. Prialnik, *An introduction to the theory of stellar structure and evolution* (2nd ed.), Cambridge University Press, Cambridge, 2010
- [7] C. E. Rolfs, W. S. Rodney, *Cauldrons in the Cosmos*, University of Chicago Press, Chicago, 1988
- [8] C. Iliadis, *Nuclear physics of stars*, Wiley-VCH Verlag GmbH & Co. KGaA, Weinheim, 2007
- [9] K. Heyde, *Basic ideas and concepts in nuclear physics. An introductory approach* (2nd ed.), IOP Publishing, London, 1999
- [10] H. Becquerel, multiple publications, Compt. Rend. **122 – 124**, (1896, 1897)
- [11] M. Skłodowska-Curie, *Rayons émis par le composés de l'uranium et du thorium*, Compt. Rend. **126**, 1101 (1898)
- [12] E. Rutherford, *Uranium radiation and the electrical conduction produced by it*, Phil. Mag. Series 5 **47**, 109 (1899)

- [13] E. Rutherford, T. Royds, *The Nature of the α Particle from Radioactive Substances*, Phil. Mag. **17**, 281 (1909)
- [14] H. Becquerel, *Déviation du Rayonnement du Radium dans un Champ Électrique*, Compt. Rend. **130**, 809 (1900)
- [15] H. Becquerel, *Sur la transparence de l'aluminium pour la rayonnement du radium*, Compt. Rend. **130**, 1154 (1900)
- [16] P. Villard, *Sur la Réflexion et la Réfraction des Rayons Cathodiques et des Rayons Déviabiles du Radium*, Compt. Rend. **130**, 1010 (1900)
- [17] H. Geiger, E. Marsden, *On a Diffuse Reflection of the α -Particles*, Proc. Royal Soc. Series A **82**, 495 (1909)
- [18] E. Rutherford, *The Scattering of α and β Particles by Matter and the Structure of the Atom*, Phil. Mag. Series 6 **21**, 669 (1911)
- [19] *The Lund/LBNL Nuclear Data Search*,
<http://nucleardata.nuclear.lu.se/nucleardata/toi/>
- [20] R. G. Lovas *et al*, *Microscopic theory of cluster radioactivity*, Phys. Rep. **294**, 265 (1998)
- [21] Gy. Csikai, *Photographic evidence for the existence of the neutrino*, Il Nuovo Cimento **5**, 1011 (1957)
- [22] P. T. Hosmer *et al*, *Half-life of the doubly magic r-process nucleus ^{78}Ni* , Phys. Rev. Lett. **94**, 112501 (2005)
- [23] Yu. A. Litvinov, F. Bosch, *Beta decay of highly charged ions*, Rep. Prog. Phys. **74**, 016301 (2011)
- [24] H. Budzikiewicz, R. D. Grigsby, *Mass spectrometry and isotopes: a century of research and discussion*, Mass. Spectrom. Rev. **25**(1), 146 (2006)
- [25] A. N. Petridis *et al*, *Exact analytical and numerical solutions to the time-dependent Schrödinger equation for a one-dimensional potential exhibiting non-exponential decay at all times*, J. Mod. Phys. **1**, 128 (2010)
- [26] S. R. Wilkinson *et al*, *Experimental evidence for non-exponential decay in quantum tunnelling*, Nature **387**, 575 (1997)
- [27] C. Rothe, S. I. Hintschich, A. P. Monkman, *Violation of the exponential-decay law at long times*, Phys. Rev. Lett. **96**, 163601 (2006)

- [28] N. G. Kelkar, M. Nowakowski, K. P. Khemchandani, *Hidden evidence of nonexponential nuclear decay*, Phys. Rev. C **70**, 24601 (2004)
- [29] Yu. A. Litvinov *et al*, *Observation of non-exponential orbital electron capture decays of hydrogen-like ^{140}Pr and ^{142}Pm ions*, Phys. Lett. B **664(3)**, 162 (2008)
- [30] P. M. Walker, *A neutrino's wobble?*, Nature **453**, 864 (2008)
- [31] A. G. Cohen, S. L. Glashow, Z. Ligeti, *Disentangling neutrino oscillations*, Phys. Lett. B **678(2)**, 191 (2009)
- [32] T. Faestermann *et al*, *Could the GSI decay rate oscillations be observed in a standard electron capture decay experiment?*, Phys. Lett. B **672(3)**, 227 (2009)
- [33] J. H. Jenkins *et al*, *Evidence of correlations between nuclear decay rates and Earth–Sun distance*, Astropart. Phys. **32**, 42 (2009)
- [34] J. H. Jenkins, E. Fischbach, *Perturbation of nuclear decay rates during the solar flare of 2006 December 13*, Astropart. Phys. **31**, 407 (2009)
- [35] D. Javorsek II *et al*, *Power spectrum analyses of nuclear decay rates*, Astropart. Phys. **34**, 173 (2010)
- [36] P. A. Sturrock *et al*, *Power spectrum analyses of BNL decay rate data*, Astropart. Phys. **34**, 121 (2010)
- [37] P. S. Cooper, *Searching for modifications to the exponential radioactive decay law with the Cassini spacecraft*, Astropart. Phys. **31**, 267 (2009)
- [38] E. B. Norman *et al*, *Evidence against correlations between nuclear decay rates and Earth–Sun distance*, Astropart. Phys. **31**, 135 (2009)
- [39] T. M. Semkow *et al*, *Oscillations in radioactive exponential decay*, Phys. Lett. B **675**, 415 (2009)
- [40] F. Cardone, R. Mignani, A. Petrucci, *Piezounuclear decay of thorium*, Phys. Lett. A **373**, 1956 (2009)
- [41] F. Cardone *et al*, *Piezounuclear reactions*, arXiv:1009.4127v1 [physics.gen-ph]
- [42] G. Ericsson *et al*, *Comment on ‘Piezonuclear decay of thorium’*, Phys. Lett. A **373**, 3795 (2009)
- [43] F. Cardone, R. Mignani, A. Petrucci, *Reply to ‘Comment on ‘Piezonuclear decay of thorium’’*, Phys. Lett. A **373**, 3797 (2009)

- [44] L. Kowalski, *Comment on ‘Piezonuclear decay of thorium’*, Phys. Lett. A **374**, 696 (2010)
- [45] F. Cardone, R. Mignani, A. Petrucci, *Reply to ‘Comment on ‘Piezonuclear decay of thorium’’*, Phys. Lett. A **374**, 698 (2010)
- [46] G. Ericsson *et al*, *Piezonnuclear reactions – do they really exist?*, Phys. Lett. A **374**, 750 (2010)
- [47] R. Ford, M. Gerbier-Violleau, E. Vázquez-Jáuregui, *Measurement of the thorium-228 activity in solutions cavitated by ultrasonic sound*, Phys. Lett. A **374**, 701 (2010)
- [48] B. Limata *et al*, *First hints on a change of the ^{22}Na β^+ -decay half-life in the metal Pd*, Eur. Phys. J. A **28**, 251 (2006)
- [49] C. Rolfs, *Nuclear reactions in stars far below the Coulomb barrier*, Prog. Part. Nucl. Phys. **59**, 43 (2007)
- [50] E. Somorjai, *Mérések a mag-asztrofizika területén: elektronárnyékolás és p-folyamat* [in Hungarian], Doctoral thesis for the Hungarian Academy of Sciences, Debrecen, 2000
- [51] G. Wallerstein *et al*, *Synthesis of the elements in stars: forty years of progress*, Rev. Mod. Phys. **69(4)**, 995 (1997)
- [52] H. J. Assenbaum, K. Langanke, C. E. Rolfs, *Effects of electron screening on low-energy fusion cross sections*, Z. Phys. A **327**, 461 (1987)
- [53] L. Bracci *et al*, *Atomic effects in the determination of nuclear cross sections of astrophysical interest*, Nucl. Phys. A **513**, 316 (1990)
- [54] G. Fiorentini, R. W. Kavanagh, C. E. Rolfs, *Prospects for underground accelerator research*, Z. Phys. A **350**, 289 (1995)
- [55] U. Greife *et al*, *Oppenheimer–Phillips effect and electron screening in d+d fusion reactions*, Z. Phys. A **351**, 107 (1995)
- [56] T. D. Shoppa *et al*, *One- and two-electron atomic screening in fusion reactions*, Phys. Rev. C **48**, 837 (1993)
- [57] C. E. Rolfs, E. Somorjai, *Status report on electron screening*, Nucl. Instrum. Meth. B **99**, 297 (1995)
- [58] K. Czerski *et al*, *Enhancement of the electron screening effect for d+d fusion reactions in metallic environments*, Europhys. Lett. **54**, 449 (2001)

- [59] F. Raiola *et al*, *Enhanced electron screening in d(d,p)t for deuterated metals*, Eur. Phys. J. A **19**, 283 (2004)
- [60] A. Ray *et al*, *Observation of large change of ^7Be decay rate in Au and Al_2O_3 and its implications*, Phys. Lett. B **455**, 69 (1999)
- [61] T. Ohtsuki *et al*, *Enhanced electron-capture decay rate of ^7Be encapsulated in C_{60} cages*, Phys. Rev. Lett. **93**, 112501 (2004)
- [62] Zhou Shu-Hua *et al*, *Large decay rate variation of ^7Be in Pd and Au*, Chin. Phys. Lett. **22**, 565 (2005)
- [63] P. Das, A. Ray, *Terrestrial ^7Be decay rate and ^8B solar neutrino flux*, Phys. Rev. C **71**, 025801 (2005)
- [64] F. Raiola *et al*, *Electron screening in d(d,p)t for deuterated metals: temperature effects*, J. Phys. G **31**, 1141 (2005)
- [65] M. Asplund, *The shining make-up of our star*, Science **322**, 51 (2008)
- [66] N. T. Zinner, *Alpha decay rate enhancement in metals: an unlikely scenario*, Nucl. Phys. A **781**, 81 (2007)
- [67] P. W. Debye, E. Hückel, Phys. Z. **24**, 185 (1923)
- [68] R. J. Goldston, P. H. Rutherford, *Introduction to plasma physics*, Institute of Physics Publishing, Bristol and Philadelphia, 1995
- [69] P. M. Bellan, *Fundamentals of plasma physics*, Cambridge University Press, 2006
- [70] R. Fitzpatrick, *Introduction to plasma physics: A graduate level course*, lecture notes, University of Texas at Austin, 2008
- [71] B. W. Sargent, *Energy distribution curves of the disintegration electrons*, Proc. Camb. Phil. Soc. **28**, 538 (1932)
- [72] K. Sailer, *Statisztikus fizika és termodinamika* [in Hungarian], lecture notes, University of Debrecen, Hungary, 1998
- [73] F. Bloch, J. D. Walecka, *Fundamentals of statistical mechanics: Manuscript and notes of Felix Bloch*, Imperial College Press and World Scientific Publishing, Stanford, 1989, 2000
- [74] D. Souza *et al*, Bull. Am. Phys. Soc. **42**, 1679 (1997)
- [75] E. B. Norman *et al*, *Influence of physical and chemical environments on the decay rates of ^7Be and ^{40}K* , Phys. Lett. B **519**, 15 (2001)

- [76] Z-Y. Liu *et al*, *Measurement of change of ${}^7\text{Be}$ decay rate in Be and Au*, Chin. Phys. Lett. **20**, 829 (2003)
- [77] S-H. Zhou *et al*, *Large decay rate variation of ${}^7\text{Be}$ in Pd and Au*, Chin. Phys. Lett. **22**, 565 (2004)
- [78] A. Ray *et al*, *Change of ${}^7\text{Be}$ decay rate in exohedral and endohedral C_{60} fullerene compounds and its implications*, Phys. Rev. C **73**, 034323 (2006)
- [79] Y. Nir-El *et al*, *Precision measurement of the decay rate of ${}^7\text{Be}$ in host materials*, Phys. Rev. C **75**, 012801(R) (2007)
- [80] T. Spillane *et al*, *The ${}^{198}\text{Au}$ β^- -half-life in the metal Au*, Eur. Phys. J. A **31**, 203 (2007)
- [81] Brookhaven National Laboratory, *National Nuclear Data Center (NNDC)*, <http://www.nndc.bnl.gov/>
- [82] H. B. Jeppesen *et al*, *Alpha-decay half-life of ${}^{221}\text{Fr}$ in different environments*, Eur. Phys. J. A **32**, 31 (2007)
- [83] K. U. Kettner *et al*, *High-Z electron screening: the cases ${}^{50}\text{V}(\text{p},\text{n}){}^{50}\text{Cr}$ and ${}^{176}\text{Lu}(\text{p},\text{n}){}^{176}\text{Hf}$* , J. Phys. G **32**, 489 (2006)
- [84] B. Singh and A. R. Farhan, *Nucl. Data Sheets* **107** (2006)
- [85] <http://periodictable.com>
- [86] J. Ziegler *et al*, *SRIM-2006.02*, <http://www.srim.org>
- [87] S. Agostinelli *et al*, *Nucl. Instr. Meth. A* **506**, 250 (2003)
- [88] M. Wojdyr, *fityk*, <http://www.unipress.waw.pl/fityk/>
- [89] G. Székely, *FGM – A flexible gamma-spectrum analysis program for a small computer*, Comp. Phys. Comm. **34**, 313 (1985)
- [90] Gy. Gyürky *et al*, *Precise half-life measurement of ${}^{110}\text{Sn}$ and ${}^{109}\text{In}$ isotopes*, Phys. Rev. C **71**, 5:7302(3) (2005)
- [91] H. C. Casey Jr. and G. L. Pearson, *Diffusion in Semiconductors*, Vol. 2, p. 163, edited by J. H. Crawford and L. M. Slifkin, Plenum Press, New York, 1975
- [92] E. M. Burbidge, G. R. Burbidge, W. A. Fowler, F. Hoyle, *Synthesis of the elements in stars*, Rev. Mod. Phys. **29(4)**, 547 (1957)
- [93] S. E. Woosley, W. M. Howard, *The p-process in supernovae*, Astrophys. J. Suppl. S. **26**, 285 (1978)

- [94] H. Schatz *et al*, *rp-process nucleosynthesis at extreme temperature and density conditions*, Phys. Rep. **294**, 167 (1998)
- [95] W. Rapp *et al*, *Sensitivity of p-process nucleosynthesis to nuclear reaction rates in a $25 M_{\odot}$ supernova model*, Astrophys. J. **653**, 474 (2006)
- [96] M. Rayet *et al*, *The p-process in Type II supernovae*, Astron. Astrophys. **298**, 517 (1995)
- [97] T. Rauscher, F-K. Thielemann, K-L. Kratz, *Nuclear level density and the determination of thermonuclear rates for astrophysics*, Phys. Rev. C **56**(3), 1613 (1997)
- [98] T. Rauscher, F-K. Thielemann, *Astrophysical reaction rates from statistical model calculations*, Atom. Data Nucl. Data **75**, 1 (2000)
- [99] Gy. Gyürky *et al*, *α -induced reactions for the astrophysical p-process: the case of ^{151}Eu* , J. Phys.: Conf. Ser. **202**, 012004 (2010)
- [100] P. Mohr, Zs. Fülöp, H. Utsunomiya, *Photo-induced nucleosynthesis: Current problems and experimental approaches*, Eur. Phys. J. A **32**, 357 (2007)
- [101] C. Fröhlich *et al*, *Neutrino-induced nucleosynthesis of $A > 64$ nuclei: the νp process*, Phys. Rev. Lett. **96**, 142502 (2006)
- [102] Gy. Gyürky *et al*, *Alpha-induced reaction cross section measurements on ^{151}Eu for the astrophysical γ -process*, J. Phys. G **37**, 115201 (2010)
- [103] G. Ruprecht *et al*, *The influence of electron screening on half-lives*, Proceedings of Science PoS(NIC-IX) 171 (2006)
- [104] B. Wang *et al*, *Change of the ^7Be electron capture half-life in metallic environments*, Eur. Phys. J. A **28**, 375 (2006)
- [105] F. Raiola *et al*, *First hint on a change of the ^{210}Po alpha-decay half-life in the metal Cu*, Eur. Phys. J. A **32**, 51 (2007)
- [106] T. Ohtsuki *et al*, *Radioactive decay speedup at $T = 5\text{K}$: Electron-capture decay rate of ^7Be encapsulated in C_{60}* , Phys. Rev. Lett. **98**, 252501 (2007)
- [107] N. Severijns *et al*, *α -decay half-life of ^{253}Es in metallic Fe at temperatures between 4 K and 50 mK*, Phys. Rev. C **76**, 024304 (2007)
- [108] J. R. Goodwin *et al*, *The half-life of ^{198}Au : High-precision measurement shows no temperature dependence*, Eur. Phys. J. A **34**, 271 (2007)

- [109] G. Lian *et al*, *Enhancement of beta⁺-decay rate of ²²Na in metal Pd at low temperature*, Chin. Phys. Lett. **25**, 70 (2008)
- [110] G. Ruprecht *et al*, *On the possible influence of electron screening on the lifetime of radioactive nuclei*, J. Phys. G **35**, 014017 (2008)
- [111] V. Kumar *et al*, *Absence of low-temperature dependence of the decay of ⁷Be and ¹⁹⁸Au in metallic hosts*, Phys. Rev. C **77**, 051304(R) (2008)
- [112] Gy. Gyürky *et al*, *Investigation of ⁷⁴As decay branching ratio dependence on the host material*, Europhys. Lett. **83**, 42001 (2008)
- [113] B. A. Fallin, B. P. Grabow and W. Tornow, *Attempt to manipulate the decay rate of ⁶⁴Cu*, Phys. Rev. C **78**, 057301 (2008)
- [114] S. Zeng *et al*, *Measurement of ¹⁹⁸Au β⁻-decay half-life in metal Au at low temperature*, Atom. En. Sci. Tech. **43** (2009)
- [115] A. Ray *et al*, *Observation of enhanced orbital electron-capture nuclear decay rate in a compact medium*, Phys. Lett. B **679**, 106 (2009)
- [116] J. Farkas *et al*, *Measurement of embedded ⁷⁴As decay branching ratio at low temperatures*, J. Phys. G **36**, 105101 (2009)
- [117] J. R. Goodwin *et al*, *Half-life of the electron capture decay of ⁹⁷Ru: Precision measurement shows no temperature dependence*, Phys. Rev. C **80**, 045501 (2009)
- [118] C-B. Li *et al*, *Search for decay rate variation of ⁷Be in Pt and Al*, Chin. Phys. Lett. **27**, 012301 (2010)
- [119] S. Pierre *et al*, *On the variation of the ²¹⁰Po half-life at low temperature*, Appl. Radiat. Isotopes **68**, 1467 (2010)
- [120] C. Gerschel, G. Albouy, C. R. Acad. Sci. (Paris) **264B**, 183 (1967)
- [121] Yu. Khazov, A. Rodionov, F. G. Kondev, Nucl. Data Sheets **112** (2011)
- [122] Gy. Gyürky *et al*, *Target characterization for the ¹³⁰Ba(α,γ)¹³⁴Ce γ-process experiment*, Proceedings of Science PoS(NIC-XI) 238(5) (2011)
- [123] T. Vylov *et al*, Izv. Akad. Nauk. SSSR, Ser. Fiz. **36**, 718 (1972)
- [124] J. C. F. Lau and J. J. Hogan, *Investigation of branching ratios between isomeric states of ¹⁵⁴Tb*, Phys. Rev. C **8**, 715 (1973)
- [125] D. C. Sousa *et al*, *Decay of the three isomers of ¹⁵⁴Tb*, Nucl. Phys. A **238**, 365 (1975)

- [126] V. G. Nedovesov, Y. V. Kholnov, G. E. Shukin, Proc. 26th Annu. Conf. Nucl. Spectrosc. Struct. At. Nuclei, Baku, p. 109 (1976)
- [127] I. Berkes, R. Brenier, G. Marest, J. Phys. G **9**, 213 (1983)
- [128] C. W. Reich, R. G. Helmer, Nucl. Data Sheets **85**, 171 (1998)
- [129] V. I. Gavriljuk, V. A. Zheltonozhskij, V. B. Kharlanov, 40th Conf. Nucl. Spectroscopy Nucl. Struct., Leningrad, p. 347 (1990)
- [130] E. Browne and J. K. Tuli, *Nucl. Data Sheets* **111**, 1093 (2010)
- [131] S. Rab, Nucl. Data Sheets **75**, 491 (1995)
- [132] S. Newcomb, *Note on the frequency of the use of digits in natural numbers*, Am. J. Math. **4**, 39 (1881)
- [133] F. Benford, *The law of anomalous numbers*, Proc. Am. Philos. Soc. **78**, 551 (1938)
- [134] J. Burke, E. Kincanon, *Benford law and physical constants – The distribution of initial digits*, Am. J. Phys. **59**, 952 (1991)
- [135] L. Pietronero *et al.*, *Explaining the uneven distribution of numbers in nature: the laws of Benford and Zipf*, Physica A **293**, 297 (2001)
- [136] J-C. Pain, *Benford's law and complex atomic spectra*, Phys. Rev. E **77**, 012102 (2008)
- [137] B. Buck, A. C. Merchant, S. M. Perez, *An illustration of Benford's first digit law using alpha decay half-lives*, Eur. J. Phys. **14**, 59 (1993)
- [138] D. Ni and Z. Ren, *Benford's law and half-lives of unstable nuclei*, Eur. Phys. J. A **38**, 251 (2008)
- [139] D. Ni, L. Wei and Z. Ren, *Benford's law and β -decay half-lives*, Commun. Theor. Phys. **51**, 713 (2009)
- [140] G. Audi *et al.*, *The NUBASE evaluation of nuclear and decay properties*, Nucl. Phys. A **729**, 3 (2003)
- [141] S. W. Smith, *The Scientist and Engineer's Guide to Digital Signal Processing* (California Technical Publishing, 1997, 2008), ch. 34, 701–722
- [142] R. M. Fewster, *A simple explanation of Benford's law*, Am. Stat. **63**(1), 26 (2009)